BEILSTEIN JOURNAL OF ORGANIC CHEMISTRY

Organic porous materials

Edited by Stefan Bräse

Imprint

Beilstein Journal of Organic Chemistry
www.bjoc.org
ISSN 1860-5397
Email: journals-support@beilstein-institut.de

The *Beilstein Journal of Organic Chemistry* is published by the Beilstein-Institut zur Förderung der Chemischen Wissenschaften.

Beilstein-Institut zur Förderung der Chemischen Wissenschaften
Trakehner Straße 7–9
60487 Frankfurt am Main
Germany
www.beilstein-institut.de

BEILSTEIN JOURNAL OF ORGANIC CHEMISTRY

Hydroxy-functionalized hyper-cross-linked ultra-microporous organic polymers for selective CO_2 capture at room temperature

Partha Samanta[1], Priyanshu Chandra[1] and Sujit K. Ghosh[*1,2]

Letter

Open Access

Address:
[1]Indian Institute of Science Education and Research (IISER), Pune. Dr. Homi Bhabha Road, Pashan, Pune-411008, India. Fax: +91 20 2589 8022; Tel: +91 20 2590 8076 and [2]Centre for Research in Energy & Sustainable Materials, IISER Pune, Pashan, Pune, India

Email:
Sujit K. Ghosh[*] - sghosh@iiserpune.ac.in

* Corresponding author

Keywords:
carbon dioxide capture; hyper-cross-linked polymer; metal-organic framework; microporous organic polymer

Beilstein J. Org. Chem. **2016,** *12,* 1981–1986.
doi:10.3762/bjoc.12.185

Received: 09 July 2016
Accepted: 19 August 2016
Published: 02 September 2016

This article is part of the Thematic Series "Organic porous materials".

Guest Editor: S. Bräse

Abstract

Two hydroxy-functionalized hyper-cross-linked ultra-microporous compounds have been synthesized by Friedel–Crafts alkylation reaction and characterised with different spectroscopic techniques. Both compounds exhibit an efficient carbon dioxide uptake over other gases like N_2, H_2 and O_2 at room temperature. A high isosteric heat of adsorption (Q_{st}) has been obtained for both materials because of strong interactions between polar –OH groups and CO_2 molecules.

Introduction

The increase in the earth's average temperature, also termed as global warming, is mainly due to the effects of greenhouse gases. The impacts of global warming includes rising sea level, more likelihood of extreme events (like floods, hurricanes etc.), widespread vanishing of animal population, loss of plankton due to warming seas. There are many heat-trapping greenhouse gases present in the atmosphere (from methane to water vapour), but CO_2 puts us at the greatest risk if it continues to accumulate in the atmosphere. This is due to the fact that CO_2 remains in the atmosphere in a time scale of hundred years in contrast to other greenhouse gases which leave the atmosphere with relatively smaller time scale [1]. The CO_2 long life in the atmosphere provides the clearest possible rationale for carbon dioxide capture and storage. Previously, different types of amine solvents were employed to study the CO_2 capture, but the need of high energy to regenerate the amine solutions after CO_2 capture, hinders their applications further [2]. In the domain of porous materials, zeolites, metal-organic frameworks (MOFs), cage molecules, etc. have been introduced for selective uptake of CO_2 [3-5]. In terms of surface area, tuneable porosity and feasible host–guest interaction, MOFs have scored over other above mentioned porous materials [6]. But the less hydrolytic stability of metal-organic frameworks limits their real time application [7,8]. So the search for new materials having high sur-

face area and feasible interaction with carbon dioxide like MOFs and with high chemical stability have become one of top priority for researchers.

Microporous organic polymers (MOP) are a relatively new class of porous materials, constructed from light elements like H, C, B, N, O etc. having a large surface area, small pore size and low skeletal density [9-12]. This type of materials has already been used for various purposes of applications such as gas storage, gas separation, catalysis, sensing, clean energy, etc. [13-18]. Relatively weaker coordination bonds in MOFs have been replaced with stronger covalent bonds in this type of porous compounds. This results in a high chemical stability of the microporous organic polymers, which is an essential condition for the real-time application of any compound. The last decade has witnessed advancements in synthesizing various types of microporous organic materials including covalent organic frameworks (COFs), conjugate microporous polymers (CMPs), porous polymeric networks (PPNs), porous aromatic frameworks (PAFs), covalent triazine framework (CTFs), etc. [19-24]. Hyper-cross-linked microporous organic polymers (HCPs) are a subclass of this type of porous materials. Recently, hyper-cross-linked MOPs are emerged as a new subclass, synthesized by hyper-cross linking of basic small organic building blocks by Friedel–Crafts reaction in the presence of the Lewis acid $FeCl_3$ (as catalyst) and formaldehyde dimethyl acetal (FDA) as the cross linker [25-27]. Here, aromatic small organic compounds are used to polymerise via C–C cross coupling to produce the targeted porous and physicochemical stable organic hyper-cross-linked polymeric materials. One huge advantage of this material is the low-cost synthesis, the cost-effective formaldehyde dimethyl acetal (FDA), $FeCl_3$ and that organic small molecules can produce very low cost materials with high yield [28]. Hyper-cross-linking prevents the close packing of polymeric chains in this type of material to impart the intrinsic porosity. Hyper-cross-linked polymers have been applied in the field of gas storage, catalysis, separation and recently also in CO_2 capture [29-32]. The increasing environmental pollution due to carbon dioxide, urges us to develop new materials with high stability, which are cost-effective and demonstrate a high efficiency in CO_2 capture. Based on the interaction of Lewis basic sites with carbon dioxide it has been observed that porous materials functionalised with $–NH_2$ groups or –OH groups exhibit a selective uptake of CO_2 in contrast to other gases [33,34] (Scheme 1). Inspired by this we have designed and synthesized two hydroxy-functionalised hyper-cross-linked microporous organic polymers for selective CO_2 capture at room temperature. Both compounds (HCP-91 and HCP-94) were synthesized via hyper-cross-linked C–C coupling of hydroxyl-functionalised aromatic rings by using a Friedel–Craftys reaction. At different temperatures (273 K and 298 K) gas (CO_2, N_2, H_2 and O_2) adsorption experiments were carried out for both compounds. HCP-91 and HCP-94 showed selective CO_2 capture at both temperatures over other flue gases.

Results and Discussion

For the synthesis of HCP-91 and HCP-94, we used 4-phenylphenol and 9-(hydroxymethyl)anthracene, respectively

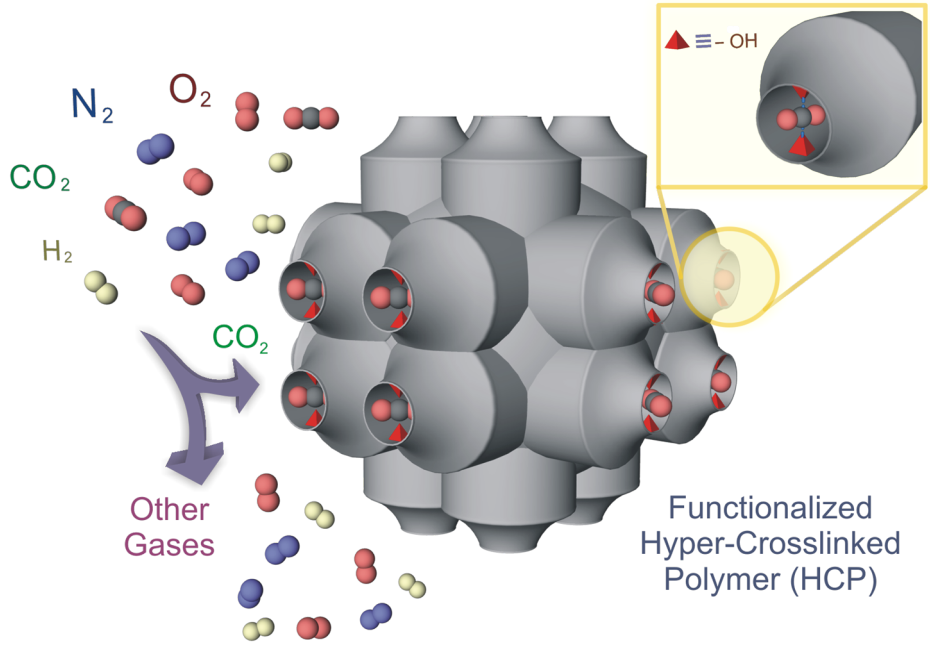

Scheme 1: Schematic representation of selective CO_2 capture in a porous material.

(Figure 1). HCP-91 and HCP-94 have been synthesized by using a Friedel–Crafts alkylation reaction. The thus obtained as-synthesized compounds were washed repeatedly with dimethylformamide (DMF), methanol, water, chloroform, dichloromethane and tetrahydrofuran (THF) to obtain phase-pure hyper-cross-linked polymers. Both compounds were immersed in a $CHCl_3$–THF (1:1) mixture and kept for 4–5 days to exchange the high boiling solvents occluded inside the framework with low boiling $CHCl_3$ and THF. The solvent-exchanged phases of HCP-91 and HCP-94 were then heated at ≈100 °C under vacuum to get the guest-free desolvated phases of the respective compounds. Infrared (IR) spectroscopy was done first to characterize the constituents of both compounds. A broad peak at ≈3000–3500 cm^{-1} and two sharp peaks at ≈1465 and ≈1527 cm^{-1} can be observed in HCP-91 corresponding to the stretching frequencies of –OH groups and aromatic C=C double bonds, respectively (Figure 2a). Similar to the HCP-91, peaks corresponding to –OH groups and aromatic C=C double bonds were found at ≈3300–3500 cm^{-1} and ≈1643 and 1500 cm^{-1}, respectively (Figure 2a). Meanwhile a thermo-

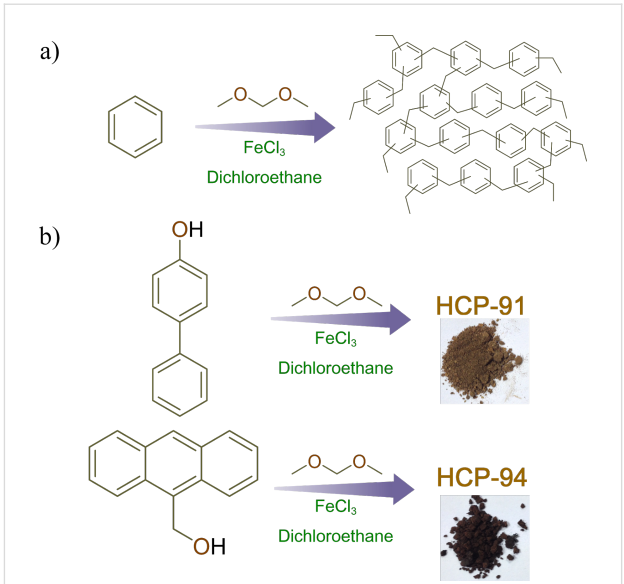

Figure 1: a) General synthesis scheme for hyper-cross-linked polymers (HCPs) and b) synthesis schemes for HCP-91 and HCP-94.

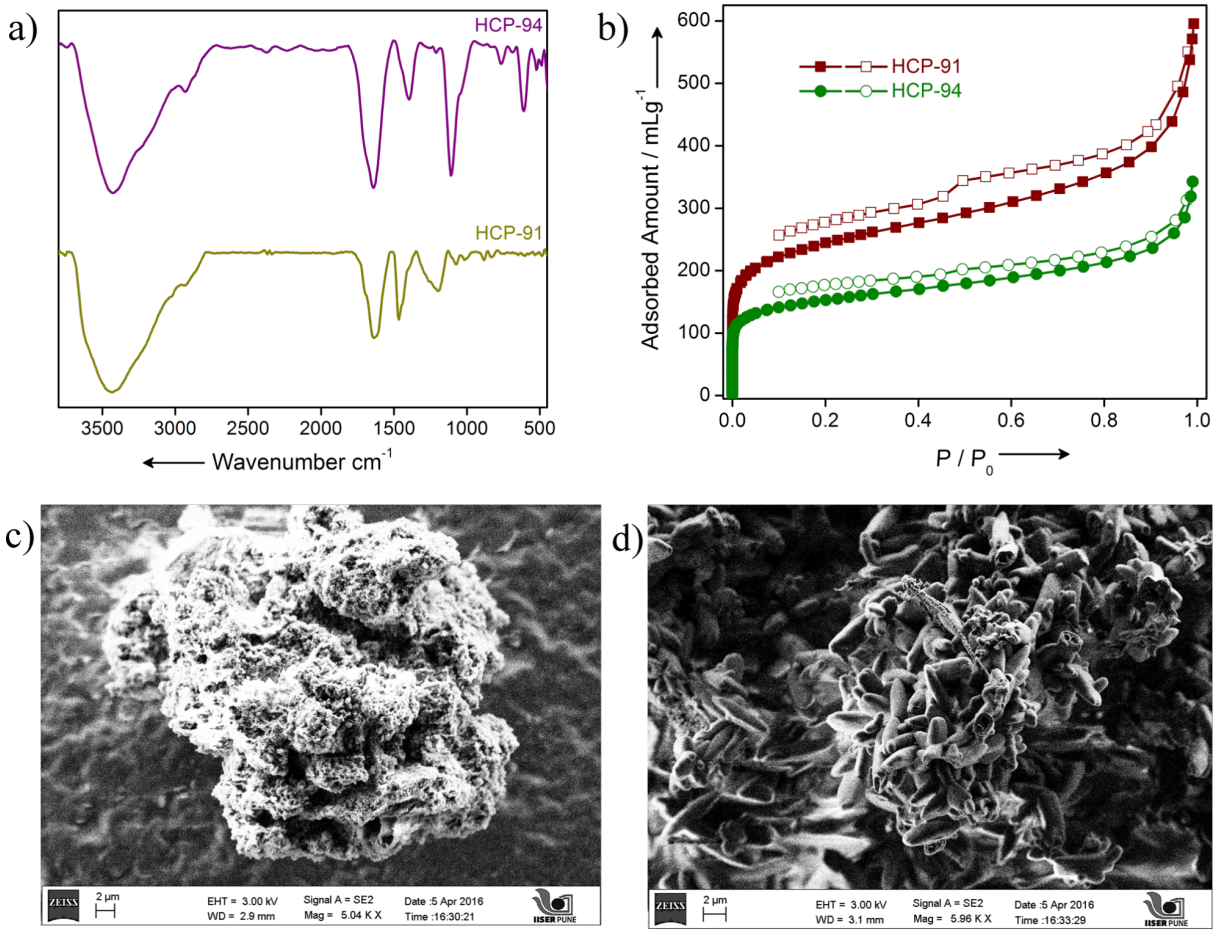

Figure 2: a) Infra-red spectra of HCP-91 (dark yellow) and HCP-94 (purple); b) N_2 adsorption isotherms for HCP-91 (wine red) and HCP-94 (green) at 77 K; c) SEM image of HCP-91 and d) SEM image of HCP-94.

gravimetric analysis (TGA) was performed with both as-synthesized and desolvated phases for HCP-91 and HCP-94. Because of the occluded solvents in the as-synthesized phases of HCP-91 and HCP-94, an initial weight loss of ≈8% and ≈10% was observed in the TGA, respectively (Figures S1 and S2 in Supporting Information File 1). Upon desolvation guest-free phases were obtained and in the TG curve a negligible loss was obtained up to ≈350 °C and ≈250 °C for HCP-91 and HCP-94, respectively (Figures S1 and S2). As confirmation of the local structures of the compounds, we performed solid state ^{13}C NMR measurements (Figures S3 and S4). To investigate the morphology of both compounds we performed a field emission scanning electron microscope (FESEM) study. The morphology of HCP-91 can be described as agglomerated particles consisting of small particles without any distinct shape (Figure 2c and Figure S5). But in case of HCP-94, a clear capsule-type of morphology was found in the FESEM (Figure 2d and Figure S6).

After all characterizations and proper desolvation of both compounds, we investigated their porosity. First, we measured the N_2 adsorption at 77 K. The N_2 uptake for HCP-91 was found to be 595 mL/g, whereas that for HCP-94 was 342 mL/g (Figure 2b). Both low temperature N_2 adsorption isotherms were of type-I category and a hysteresis was observed in desorption profiles. The hysteresis in the desorption curves can be explained in terms of a network swelling in the presence of condensed nitrogen [34]. The Howarth–Kawazoe pore-size distributions were calculated from low-temperature N_2 adsorption data. HCP-91 and HCP-94 exhibit pore sizes of 0.59 and 0.46 nm, respectively (Supporting Information File 1, Figures S7 and S8). According to recent literature, both compounds belong to the ultra-microporous material domain as pore sizes for the above mentioned compounds are lesser than 0.7 nm [35]. Carbon dioxide uptakes of 365 mL/g and 224 mL/g for HCP-91 and HCP-94, respectively, were observed when the CO_2 adsorption was carried out at 195 K (Figure 3a). The hysteresis in the CO_2 desorption profile in case of both compounds accounts for the interaction between hydroxy groups and CO_2 molecules [33,34]. Since both compounds are ultra-microporous in nature, BET (Brunauer–Emmett–Teller) surface areas were calculated from the CO_2 adsorption profile at 195 K (Supporting Information File 1, Table S1).

The effective CO_2 uptake at 195 K encouraged us to perform a CO_2 adsorption study at room temperature. HCP-91 and HCP-94 both exhibit an adequate amount of carbon dioxide uptake at 273 K and 298 K (Figures S9 and S10, Supporting Information File 1). At 273 K the CO_2 uptake was 74 mL/g for HCP-91 and 65 mL/g for HCP-94 at 1 bar (Figure 3b,d). In the case of CO_2 adsorption at 298 K a similar uptake has been observed for both compounds: 43 mL/g (HCP-91) and 45 mL/g (HCP-94) at 1 bar (Figure 3c,e). The uptake amounts of CO_2 at room temperature and 1 bar are comparable with other well performing microp-

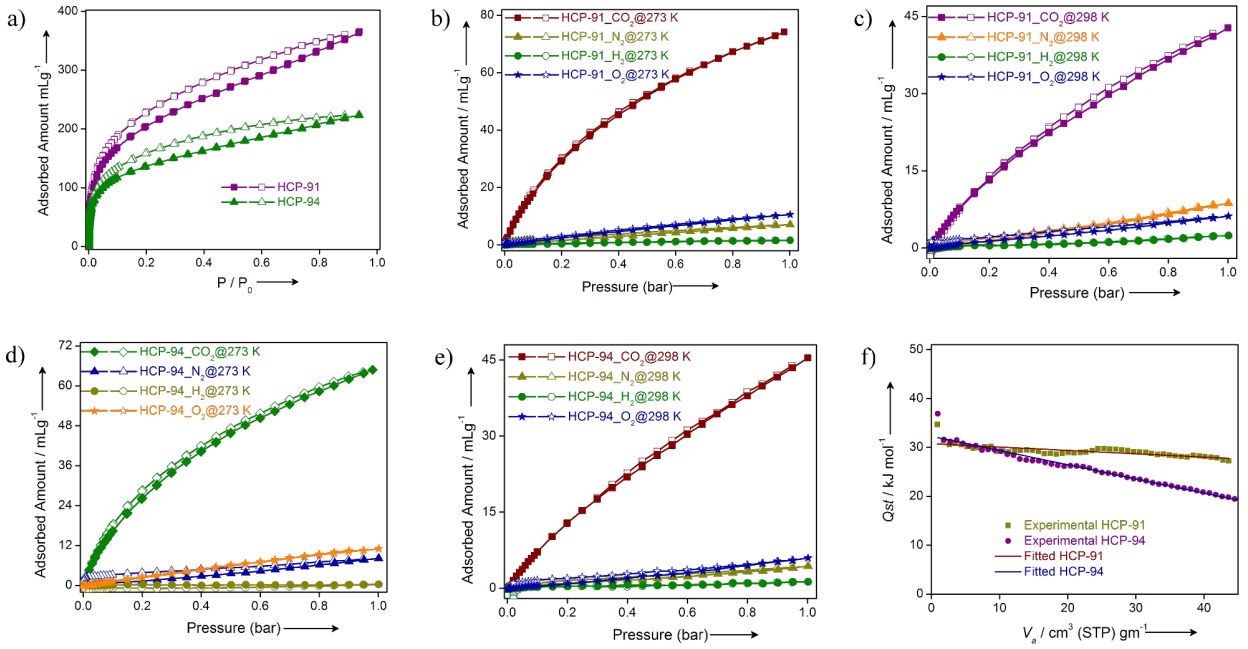

Figure 3: a) CO_2 adsorption isotherms for HCP-91 (purple) and HCP-94 (green) at 195 K; b) adsorption isotherms of CO_2 (wine red), N_2 (dark yellow), H_2 (green) and O_2 (blue) for HCP-91 at 273 K; c) adsorption isotherms of CO_2 (purple), N_2 (orange), H_2 (green) and O_2 (blue) for HCP-91 at 298 K; d) adsorption isotherms of CO_2 (green), N_2 (blue), H_2 (dark yellow) and O_2 (orange) for HCP-94 at 273 K; e) adsorption isotherms of CO_2 (wine red), N_2 (dark yellow), H_2 (green) and O_2 (blue) for HCP-94 at 298 K and f) Q_{st} plots for HCP-91 (dark yellow) and HCP-94 (purple).

orous polymer compounds. Meanwhile adsorption of other gases like nitrogen, hydrogen and oxygen (constituents of air) were performed at 273 K and 298 K and 1 bar. Interestingly very negligible amounts of uptake were obtained for each of them (Figure 3b–e). This type of CO_2 separation over other flue gases at room temperature can be attributed to the high interaction of carbon dioxide with the framework. Both hyper-cross-linked polymers have hydroxy groups which are polar in nature. On the other hand CO_2 molecules have a quadrupole moment, which renders a positive charge density over the carbon atom. So the polar hydroxy groups can offer a strong dipole-quadrupole moment interaction with carbon dioxide molecules. For a better understanding of the interaction between CO_2 and our HCPs materials, we calculated the isosteric heat of adsorption (Q_{st}) for CO_2. Heat of adsorptions for both compounds has been calculated from CO_2 adsorption data at 273 K and 298 K by using the Clausius–Clapeyron equation (Figure 3f) [33]. The Q_{st} values for HCP-91 and HCP-94 were found to be 30.7 kJ mol^{-1} and 32 kJ mol^{-1}, respectively. According to the previous reports, this high isosteric heat of adsorption values for both the materials indicates the strong interaction of it with CO_2 molecules.

Conclusion

In this report, we have synthesized two hyper-cross-linked ultra-microporous organic polymers (HCP-91 and HCP-94) by following a cost-effective and easy synthesis route. One step Friedel–Crafts syntheses were carried out by using hydroxy-functionalized organic building blocks. Both compounds were characterised thoroughly by IR spectroscopy, TG analysis, solid state ^{13}C NMR technique, FESEM and adsorption measurements. An efficient selective carbon dioxide capture was obtained for both compounds over other flue gases. High Q_{st} values for both compounds ascribed the strong dipole–quadrupole interaction between polar –OH groups and CO_2 molecules. We believe that this result will stimulate further design and fabrication of such low cost materials to be used as carbon dioxide capture materials.

Supporting Information

The Supporting Information contains the experimental section, thermo-gravimetric analysis curves, solid state ^{13}C NMR, FESEM images, pore size distribution plots and room temperature CO_2 adsorption plots.

Supporting Information File 1

Experimental and analytical data.
[http://www.beilstein-journals.org/bjoc/content/supplementary/1860-5397-12-185-S1.pdf]

Acknowledgements

P.S. and P.C. are thankful to UGC and INSPIRE, respectively, for fellowships. We acknowledge IISER Pune and MHRD FAST for financial support. We also acknowledge Mr. Aamod V. Desai, Mr. Soumya Mukherjee and Mr. Avishek Karmakar for their valuable suggestions.

References

1. Forster, P.; Ramaswamy, V.; Artaxo, P.; Berntsen, T.; Betts, R.; Fahey, D. W.; Haywood, J.; Lean, J.; Lowe, D. C.; Myhre, G.; Nganga, J.; Prinn, R.; Raga, G.; Schulz, M.; Van Dorland, R. *Climate Change 2007: The Physical Science Basis. Contribution of Working Group I to the Fourth Assessment Report of the Intergovernmental Panel on Climate Change;* 2007.
2. Rochelle, G. T. *Science* **2009,** *325,* 1652–1654. doi:10.1126/science.1176731
3. Bae, Y.-S.; Snurr, R. Q. *Angew. Chem., Int. Ed.* **2011,** *50,* 11586–11596. doi:10.1002/anie.201101891
4. Slater, A. G.; Cooper, A. I. *Science* **2015,** 348. doi:10.1126/science.aaa8075
5. Li, J.-R.; Kuppler, R. J.; Zhou, H.-C. *Chem. Soc. Rev.* **2009,** *38,* 1477–1504. doi:10.1039/b802426j
6. Mason, J. A.; Sumida, K.; Herm, Z. R.; Krishna, R.; Long, J. R. *Energy Environ. Sci.* **2011,** *4,* 3030–3040. doi:10.1039/c1ee01720a
7. Lu, W.; Yuan, D.; Sculley, J.; Zhao, D.; Krishna, R.; Zhou, H.-C. *J. Am. Chem. Soc.* **2011,** *133,* 18126–18129. doi:10.1021/ja2087773
8. Keskin, S.; van Heest, T. M.; Sholl, D. S. *ChemSusChem* **2010,** *3,* 879–891. doi:10.1002/cssc.201000114
9. Jiang, J.; Zhao, Y.; Yaghi, O. M. *J. Am. Chem. Soc.* **2016,** *138,* 3255–3265. doi:10.1021/jacs.5b10666
10. Thomas, A. *Angew. Chem., Int. Ed.* **2010,** *49,* 8328–8344. doi:10.1002/anie.201000167
11. McKeown, N. B.; Budd, P. M. *Macromolecules* **2010,** *43,* 5163–5176. doi:10.1021/ma1006396
12. Dawson, R.; Stöckel, E.; Holst, J. R.; Adams, D. J.; Cooper, A. I. *Energy Environ. Sci.* **2011,** *4,* 4239–4245. doi:10.1039/c1ee01971f
13. Patel, H. A.; Je, S. H.; Park, J.; Chen, D. P.; Jung, Y.; Yavuz, C. T.; Coskun, A. *Nat. Commun.* **2013,** *4,* No. 1357. doi:10.1038/ncomms2359
14. DeBlase, C. R.; Silberstein, K. E.; Truong, T.-T.; Abruña, H. D.; Dichtel, W. R. *J. Am. Chem. Soc.* **2013,** *135,* 16821–16824. doi:10.1021/ja409421d
15. Stegbauer, L.; Schwinghammer, K.; Lotsch, B. V. *Chem. Sci.* **2014,** *5,* 2789–2793. doi:10.1039/C4SC00016A
16. Wang, J.; Sng, W.; Yi, G.; Zhang, Y. *Chem. Commun.* **2015,** *51,* 12076–12079. doi:10.1039/C5CC04702A
17. Gopalakrishnan, D.; Dichtel, W. R. *J. Am. Chem. Soc.* **2013,** *135,* 8357–8362. doi:10.1021/ja402668e
18. Karmakar, A.; Kumar, A.; Chaudhari, A. K.; Samanta, P.; Desai, A. V.; Krishna, R.; Ghosh, S. K. *Chem. – Eur. J.* **2016,** *22,* 4931–4937. doi:10.1002/chem.201600109
19. Waller, P. J.; Gándara, F.; Yaghi, O. M. *Acc. Chem. Res.* **2015,** *48,* 3053–3063. doi:10.1021/acs.accounts.5b00369
20. Xu, Y.; Jin, S.; Xu, H.; Nagai, A.; Jiang, D. *Chem. Soc. Rev.* **2013,** *42,* 8012–8031. doi:10.1039/c3cs60160a
21. Ben, T.; Pei, C.; Zhang, D.; Xu, J.; Deng, F.; Jing, X.; Qiu, S. *Energy Environ. Sci.* **2011,** *4,* 3991–3999. doi:10.1039/c1ee01222c

22. Bojdys, M. J.; Jeromenok, J.; Thomas, A.; Antonietti, M. *Adv. Mater.* **2010,** *22,* 2202–2205. doi:10.1002/adma.200903436
23. Ben, T.; Ren, H.; Ma, S.; Cao, D.; Lan, J.; Jing, X.; Wang, W.; Xu, J.; Deng, F.; Simmons, J. M.; Qiu, S.; Zhu, G. *Angew. Chem., Int. Ed.* **2009,** *48,* 9457–9460. doi:10.1002/anie.200904637
24. Lu, W.; Sculley, J. P.; Yuan, D.; Krishna, R.; Wei, Z.; Zhou, H.-C. *Angew. Chem., Int. Ed.* **2012,** *51,* 7480–7484. doi:10.1002/anie.201202176
25. Li, B.; Gong, R.; Wang, W.; Huang, X.; Zhang, W.; Li, H.; Hu, C.; Tan, B. *Macromolecules* **2011,** *44,* 2410–2414. doi:10.1021/ma200630s
26. Luo, Y.; Li, B.; Wang, W.; Wu, K.; Tan, B. *Adv. Mater.* **2012,** *24,* 5703–5707. doi:10.1002/adma.201202447
27. Dawson, R.; Ratvijitvech, T.; Corker, M.; Laybourn, A.; Khimyak, Y. Z.; Cooper, A. I.; Adams, D. J. *Polym. Chem.* **2012,** *3,* 2034–2038. doi:10.1039/c2py20136d
28. Msayib, K. J.; McKeown, N. B. *J. Mater. Chem. A* **2016,** *4,* 10110–10113. doi:10.1039/C6TA03257E
29. Woodward, R. T.; Stevens, L. A.; Dawson, R.; Vijayaraghavan, M.; Hasell, T.; Silverwood, I. P.; Ewing, A. V.; Ratvijitvech, T.; Exley, J. D.; Chong, S. Y.; Blanc, F.; Adams, D. J.; Kazarian, S. G.; Snape, C. E.; Drage, T. C.; Cooper, A. I. *J. Am. Chem. Soc.* **2014,** *136,* 9028–9035. doi:10.1021/ja5031968
30. Bhunia, S.; Banerjee, B.; Bhaumik, A. *Chem. Commun.* **2015,** *51,* 5020–5023. doi:10.1039/C4CC09872B
31. Mondal, J.; Kundu, S. K.; Ng, W. K. H.; Singuru, R.; Borah, P.; Hirao, H.; Zhao, Y.; Bhaumik, A. *Chem. – Eur. J.* **2015,** *21,* 19016–19027. doi:10.1002/chem.201504055
32. Li, H.; Meng, B.; Chai, S.-H.; Liu, H.; Dai, S. *Chem. Sci.* **2016,** *7,* 905–909. doi:10.1039/C5SC04034E
33. Jing, X.; Zou, D.; Cui, P.; Ren, H.; Zhu, G. *J. Mater. Chem. A* **2013,** *1,* 13926–13931. doi:10.1039/c3ta13115g
34. Dawson, R.; Stevens, L. A.; Drage, T. C.; Snape, C. E.; Smith, M. W.; Adams, D. J.; Cooper, A. I. *J. Am. Chem. Soc.* **2012,** *134,* 10741–10744. doi:10.1021/ja301926h
35. Kim, K. C.; Yoon, T.-U.; Bae, Y.-S. *Microporous Mesoporous Mater.* **2016,** *224,* 294–301. doi:10.1016/j.micromeso.2016.01.003

License and Terms

BEILSTEIN JOURNAL OF ORGANIC CHEMISTRY

Robust C–C bonded porous networks with chemically designed functionalities for improved CO_2 capture from flue gas

Damien Thirion[1], Joo S. Lee[1], Ercan Özdemir[1] and Cafer T. Yavuz[*1,2,§]

Letter

Open Access

Address:
[1]Graduate School of Energy, Environment, Water, Sustainability (EEWS), Korea Advanced Institute of Science and Technology (KAIST), Guseong Dong, Yuseong Gu, Daejeon 305–701, Korea and [2]Department of Chemistry, Korea Advanced Institute of Science and Technology (KAIST), Guseong Dong, Yuseong Gu, Daejeon 305–701, Korea

Email:
Cafer T. Yavuz[*] - yavuz@kaist.ac.kr

* Corresponding author
§ www.porouspolymers.com, Tel: +82-42-350-1718

Keywords:
C–C bond; CO_2 capture; microporous materials; porous polymers; postmodification

Beilstein J. Org. Chem. **2016,** *12,* 2274–2279.
doi:10.3762/bjoc.12.220

Received: 05 August 2016
Accepted: 14 October 2016
Published: 28 October 2016

This article is part of the Thematic Series "Organic porous materials".

Guest Editor: S. Bräse

Abstract

Effective carbon dioxide (CO_2) capture requires solid, porous sorbents with chemically and thermally stable frameworks. Herein, we report two new carbon–carbon bonded porous networks that were synthesized through metal-free Knoevenagel nitrile–aldol condensation, namely the covalent organic polymer, COP-156 and 157. COP-156, due to high specific surface area (650 m^2/g) and easily interchangeable nitrile groups, was modified post-synthetically into free amine- or amidoxime-containing networks. The modified COP-156-amine showed fast and increased CO_2 uptake under simulated moist flue gas conditions compared to the starting network and usual industrial CO_2 solvents, reaching up to 7.8 wt % uptake at 40 °C.

Findings

Porous polymers are network polymers that are made from multivalent monomers and form permanent pores through the net formation [1]. They differ slightly from cross-linked polymers with more certainty in the location of branching and the type and quantity of functionalities. Also, the rigidity of the monomers is essential since the porosity, a desired feature, is best achieved by structurally interlocked motifs. In industrial applications, porous polymers have to meet several important criteria like high porosity, chemical and thermal stability while also possessing application-specific functionalities [1,2]. Designing and synthesizing structures that respect all these criteria is a challenging task. Chemical and thermal stability can be achieved best by having robust C–C bonded architecture like in porous polymer networks (PPNs) [3], porous aromatic frameworks (PAFs) [4] or conjugated microporous polymers (CMPs) [5]. Most of these networks have the advantage of high

porosity, but they are all made through precious metal-catalyzed reactions, which elevates the synthesis cost and limits their mass production. Another type of C–C bonded porous networks are hypercrosslinked polymers (HCPs) [6]. HCPs are mainly synthesized through Friedel–Crafts alkylation using iron chloride and thus, are not relying on precious metals. Unfortunately, Friedel–Crafts reactions are not very tolerant to functional groups like nitriles or amines [7]. On the other hand, structures incorporating heteroatoms, such as nitrogen in imine, Tröger's base or azo linked networks [8-11], have led to materials with remarkable gas uptake properties. Compared to C–C bonded networks, C–O or C–N linked structures are less thermally stable or chemically resistant. Furthermore, the chemical reactions involved in the formation of these structures do not allow obtaining free nitrile or amine functionalities. The most used strategy to install available functional groups on porous materials is through post-modification, which often requires several steps and harsh conditions, and yields low porosity [12,13].

The Knoevenagel condensation of benzyl nitriles and aldehydes produces C–C bonded products with labile nitrile functionalities. In fact, nitrile groups have been shown in porous polymers (particularly in polymers of intrinsic microporosity (PIMs)) to be good precursors to several functionalities like carboxylic acids, tetrazoles, amines or amidoximes [14-17]. To the best of our knowledge the nitrile functionality has not been explored in other types of porous polymers, except our earlier work [18].

Herein we report the synthesis of two new cyanovinylene-bridged covalent organic polymers, indexed as COP-156 and COP-157, through Knoevenagel nitrile–aldol condensation. COP-156 showed a high surface area (650 m^2/g) with a hierarchical porosity, allowing synthetic post-modifications. The nitrile functional groups were first reduced to amine groups (COP-156-amine) and then through reaction with hydroxylamine converted into amidoxime groups (COP-156-amidoxime). The COP-156-amine proved increased affinity towards CO_2 with stronger binding energy, especially under moist conditions, reaching up to 7.8 wt % at 40 °C, a 2.1 wt % increase when compared to the original COP-156.

Despite the promise, cyanovinylene bridged porous networks are not studied extensively and our previously reported COP-100 structure [18] suffered from low porosity. In order to obtain a cyanovinylene-bridged porous network with tangible surface area, different core and linker combinations were tested leading to the synthesis of COP-156 and COP-157 (Scheme 1). Tetraphenylmethane cores are well-known tetrahedral building blocks that are commonly employed to form highly porous materials [4,19]. A trivalent 1,3,5-phenylenetriacetonitrile linker led to COP-156 whereas a divalent 1,4-phenylenediacetonitrile formed COP-157 (Scheme 1). Despite having the same tetra-

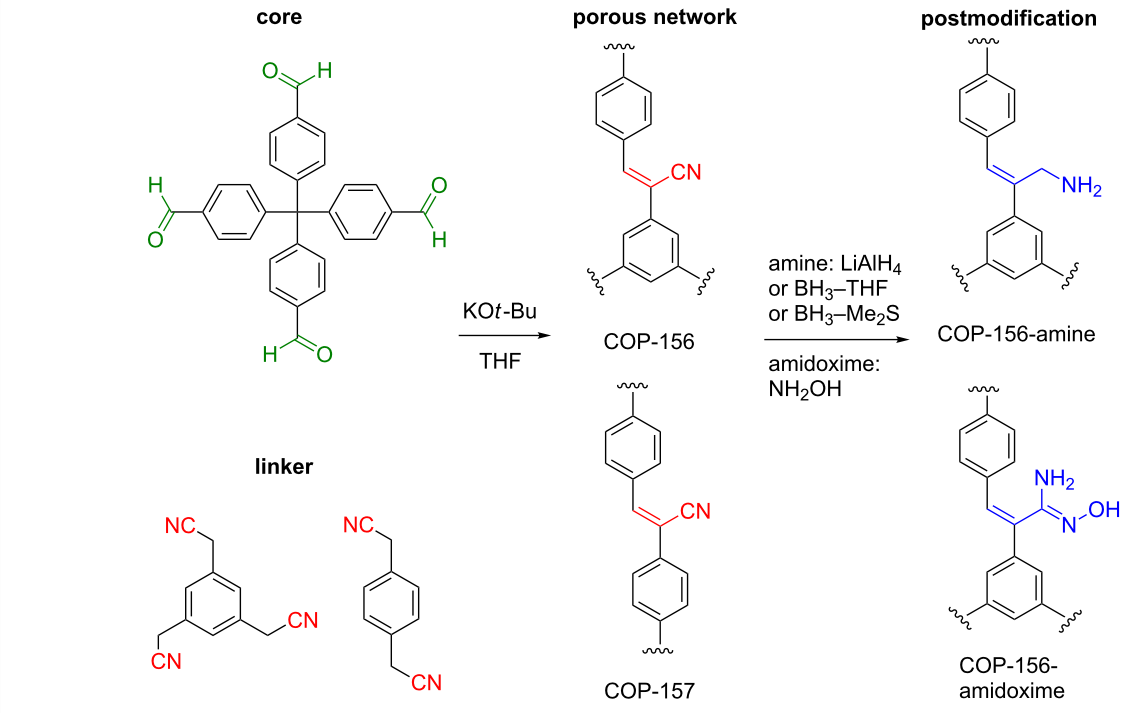

Scheme 1: Synthesis route for COP-156 and COP-157, and the post-modification of COP-156.

hedral core, COP-156 showed a much higher surface area (650 m^2/g) than COP-157 (146 m^2/g). One possible reason is the framework interpenetration, where neighboring branches of a network polymer intertwine through the adjacent open pore. For these reasons, we studied COP-156 for post-modification.

COP-156 possesses labile nitrile functionalities, which can easily be transformed into amines or amidoximes. Amines are especially attractive for gas uptake [20] and amidoximes are shown effective in uranium capture [21]. COP-156 has been post-modified through two different routes, either by reduction to the corresponding amine or reaction with hydroxylamine into an amidoxime. For the reduction, three reagents ($LiAlH_4$, BH_3–THF and BH_3–Me_2S) were screened. All reductions were chemically successful, but the textural properties of the modified networks were noticeably different. BH_3–Me_2S gave the highest surface area and therefore CO_2 uptake studies were based on this reduction method (see Supporting Information File 1, Table S1 for the properties of other obtained reduced networks). All networks were studied by FTIR, elemental analysis, TGA, and gas sorption experiments.

The FTIR spectra of COP-156 shows the characteristic nitrile stretch at 2215 cm^{-1} and several bands for the carbon–carbon double bonds (C=C) of both aromatic and alkene between 1600 and 1350 cm^{-1} (Figure 1). The presence of a peak at 1698 cm^{-1} can be attributed to carbonyl units from unreacted aldehydes. This is further confirmed in elemental analysis showing the presence of 4–5 % oxygen (Supporting Information File 1, Table S2). The condensation reaction is very fast and the formed network precipitates in a matter of minutes, leading to unreacted aldehyde edges on the surface of the grains, explaining the leftover carbonyl units. COP-157 shows similar results due to the chemical similarity of the structures and the reaction conditions (Supporting Information File 1, Figure S1 and Table S2).

After post-modification, the nitrile stretching becomes very weak in both COP-156-amine and COP-156-amidoxime, confirming the chemical modification of the nitrile units (Figure 1). A broad region around 3400 cm^{-1} can be attributed to the NH stretching of the formed amine groups and the two peaks at 2931 and 2866 cm^{-1} belong to sp^3 CH stretching of the formed methylene unit in COP-156-amine. For COP-156-amidoxime the 3400 cm^{-1} region is even broader, due to the combination of both NH and OH stretching. The strong peak at 1664 cm^{-1} can be attributed to the imine C=N bond of the amidoxime structure.

The textural properties were measured through nitrogen sorption isotherms at 77 K and calculated based on the

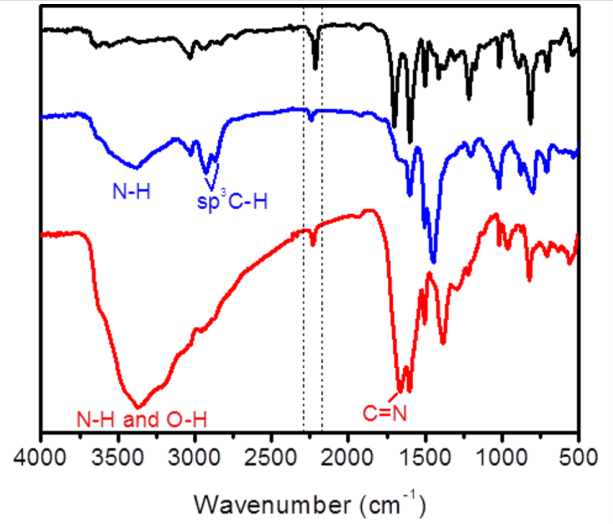

Figure 1: FTIR spectra of COP-156 (black), COP-156-amine (blue) and COP-156-amidoxime (red). The dotted lines highlight the characteristic stretching for the nitrile functionality (2215 cm^{-1}), which loses intensity by the post-modification reactions.

Brunauer–Emmett–Teller (BET) theory. COP-156 shows type II N_2 sorption isotherms and a slight hysteresis, owing to the existence of micro, meso and macropores, with a surface area of 650 m^2/g and a pore volume of 0.82 cm^3/g at P/P_0 = 0.99 (Figure 2). The pore size distribution is broad with several important pore sizes (2.2, 3.0, 5.0, 7.0 nm). Larger pores are required for post-modification, as the reagents may not be able to penetrate to the small micropores. CO_2 sorption isotherms reflect the physisorptive nature of COP-156 with almost no hysteresis and an isosteric heat of adsorption (Q_{st}) of 28.1 kJ mol^{-1} (Table 1, Figure 2 and Supporting Information File 1, Figure S3). COP-157 gave a similar isotherm but with lesser surface area (Supporting Information File 1, Figures S4 and S5). This could be explained by a higher interpenetration probability of the network structure than in COP-156, as the linker used for COP-157 is linear [22,23].

After post-modification, the surface area diminishes, which is a common observation [13,24]. Yet, the pore volume of COP-156-amine increases to 0.99 cm^3/g at P/P_0 = 0.99, due to newly created pores from the reduction reaction (Figure 2). COP-156-amidoxime has decreased both surface area (67 m^2/g) and pore volume (0.41 cm^3/g at P/P_0 = 0.99), as the functional group is larger than amine or nitrile. It should be noted that elemental analysis does not reach 100% with the measured elements (C, H, N, O), indicating the presence of trapped reagents in the pores. These could not be removed with extensive washing and therefore contribute to the porosity loss (Supporting Information File 1, Table S2). Nevertheless, CO_2 sorption isotherms of COP-156-amine show a slight hysteresis, indicating that the network is not purely physisorptive anymore. At 0.15 bar (the

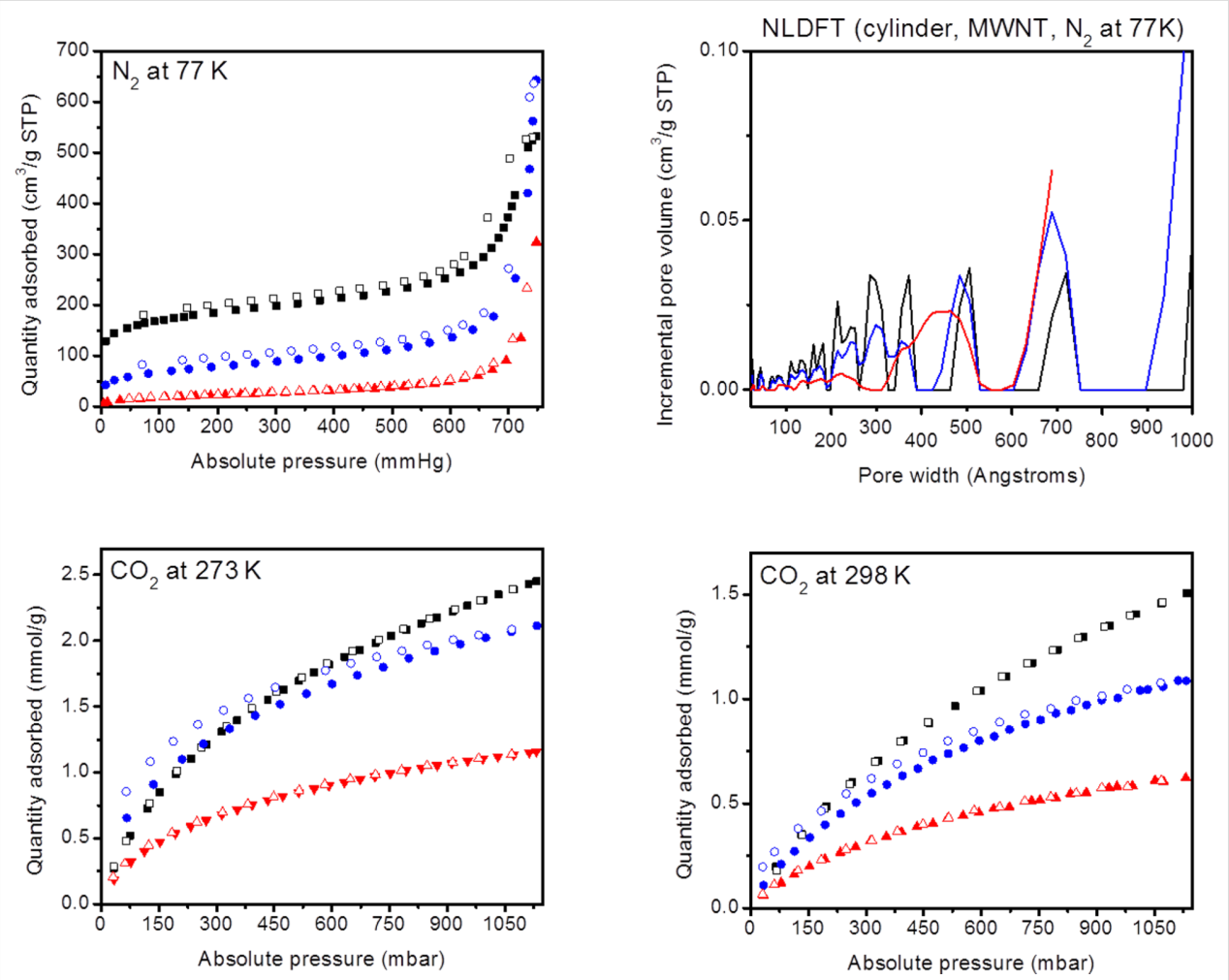

Figure 2: Gas adsorption (filled dots)-desorption (empty dots) isotherms and pore size distribution of COP-156 (black), COP-156-amine (blue) and COP-156-amidoxime (red).

Table 1: BET surface area, CO_2 sorption properties at 273 K, 298 K and heat of adsorption values of all networks.

Structure	BET surface area (m^2/g)	CO_2 at 273 K (mmol/g) 0.15/1 bar	CO_2 at 298 K (mmol/g) 0.15/1 bar	Q_{st} (kJ/mol)[a]
COP-156	650	0.84/2.31	0.38/1.40	28.1
COP-157	146	0.45/1.18	0.22/0.71	29.5
COP-156-amine	263	0.94/2.00	0.34/1.09	49.9
COP-156-amidoxime	67	0.47/1.10	0.20/0.58	38.6

[a]Zero point coverage Q_{st} calculated from 273 K and 298 K.

relevant pressure of CO_2 in flue gas emission) and 273 K, the uptake is slightly higher than the starting COP-156. The chemisorptive behavior and stronger binding affinity is reflected in the higher Q_{st} value of 49.9 kJ mol^{-1}. The moderate binding energy is optimal for CO_2 capture, as too strong binding requires high regeneration energy and raises the overall cost of the carbon capture operations [12,25].

Dry CO_2 uptake is not always meaningful, especially with amine functionalities, as flue gas from power plants contains moisture [26]. When binding to CO_2, amines go through either carbamate or carbamic acid formation. Carbamates form with the contribution of two amines and carbamic acid needs one amine and a water molecule. The presence of moisture, therefore, favors the formation of carbamic acids and leads to higher

uptake capacity per sorbent mass. We performed moist CO_2 uptake experiments in order to mimic an actual power plant flue gas on COP-156 and COP-156-amine (see Supporting Information File 1 for the experimental details).

As expected, COP-156-amine shows faster and higher uptake than COP-156 (Figure 3). For the COP-156-amine 80% of the total CO_2 uptake is reached in 21 minutes, while COP-156 requires around 30 minutes to reach the same percentage. COP-156-amine yields a total uptake of 7.8 wt %, which is 2.1 wt % more than COP-156. These CO_2 capacities are considerably higher than the industrial standard, monoethanolamine (MEA) (usually 2.1–5.5 wt %) [27,28].

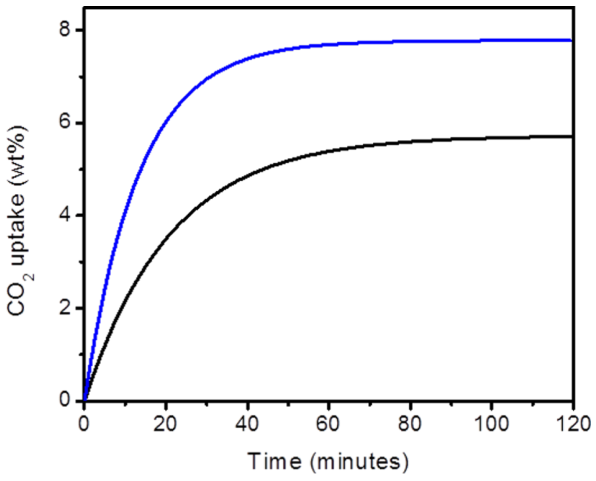

Figure 3: CO_2 uptake under moist conditions at 40 °C of COP-156 (black) and COP-156-amine (blue).

In summary, we have shown that highly porous cyanovinylene networks could be obtained through Knoevenagel condensation of benzylic nitriles and aldehydes by choosing appropriate building blocks. The resulting nitrile functionalities in COP-156 could be easily modified into free amine or amidoxime groups. The amine functionalities in COP-156-amine allowed for higher CO_2 binding strength and therefore led to fast and improved CO_2 uptake in moist conditions.

Supporting Information

Supporting Information File 1

Materials and methods, synthesis, FTIR spectra and gas sorption isotherms of COP-157, heat of adsorption graph, elemental analysis and TGA of all structures.
[http://www.beilstein-journals.org/bjoc/content/supplementary/1860-5397-12-220-S1.pdf]

Acknowledgements

This work was supported by the National Research Foundation of Korea (NRF) grant funded by the Korea government (MSIP) (No. NRF-2016R1A2B4011027).

References

1. Wu, D.; Xu, F.; Sun, B.; Fu, R.; He, H.; Matyjaszewski, K. *Chem. Rev.* **2012,** *112,* 3959. doi:10.1021/cr200440z
2. Slater, A. G.; Cooper, A. I. *Science* **2015,** *348,* 6238. doi:10.1126/science.aaa8075
3. Lu, W.; Yuan, D.; Zhao, D.; Schilling, C. I.; Plietzsch, O.; Muller, T.; Bräse, S.; Guenther, J.; Blümel, J.; Krishna, R.; Li, Z.; Zhou, H.-C. *Chem. Mater.* **2010,** *22,* 5964. doi:10.1021/cm1021068
4. Ben, T.; Ren, H.; Ma, S.; Cao, D.; Lan, J.; Jing, X.; Wang, W.; Xu, J.; Deng, F.; Simmons, J. M.; Qiu, S.; Zhu, G. *Angew. Chem., Int. Ed.* **2009,** *48,* 9457. doi:10.1002/anie.200904637
5. Cooper, A. I. *Adv. Mater.* **2009,** *21,* 1291. doi:10.1002/adma.200801971
6. Martin, C. F.; Stöckel, E.; Clowes, R.; Adams, D. J.; Cooper, A. I.; Pis, J. J.; Rubiera, F.; Pevida, C. *J. Mater. Chem.* **2011,** *21,* 5475. doi:10.1039/c0jm03534c
7. Dawson, R.; Ratvijitvech, T.; Corker, M.; Laybourn, A.; Khimyak, Y. Z.; Cooper, A. I.; Adams, D. J. *Polym. Chem.* **2012,** *3,* 2034. doi:10.1039/c2py20136d
8. Patel, H. A.; Je, S. H.; Park, J.; Chen, D. P.; Jung, Y.; Yavuz, C. T.; Coskun, A. *Nat. Commun.* **2013,** *4,* No. 1357. doi:10.1038/ncomms2359
9. Byun, J.; Je, S.-H.; Patel, H. A.; Coskun, A.; Yavuz, C. T. *J. Mater. Chem. A* **2014,** *2,* 12507. doi:10.1039/C4TA00698D
10. Côté, A. P.; Benin, A. I.; Ockwig, N. W.; O'Keeffe, M.; Matzger, A. J.; Yaghi, O. M. *Science* **2005,** *310,* 1166. doi:10.1126/science.1120411
11. Schwab, M. G.; Fassbender, B.; Spiess, H. W.; Thomas, A.; Feng, X.; Müllen, K. *J. Am. Chem. Soc.* **2009,** *131,* 7216. doi:10.1021/ja902116f
12. Islamoglu, T.; Kim, T.; Kahveci, Z.; El-Kadri, O. M.; El-Kaderi, H. M. *J. Phys. Chem. C* **2016,** *120,* 2592. doi:10.1021/acs.jpcc.5b12247
13. Lu, W.; Sculley, J. P.; Yuan, D.; Krishna, R.; Wei, Z.; Zhou, H.-C. *Angew. Chem., Int. Ed.* **2012,** *51,* 7480. doi:10.1002/anie.201202176
14. Patel, H. A.; Yavuz, C. T. *Chem. Commun.* **2012,** *48,* 9989. doi:10.1039/c2cc35392j
15. Mason, C. R.; Maynard-Atem, L.; Heard, K. W. J.; Satilmis, B.; Budd, P. M.; Friess, K.; Lanč, M.; Bernardo, P.; Clarizia, G.; Jansen, J. C. *Macromolecules* **2014,** *47,* 1021. doi:10.1021/ma401869p
16. Du, N.; Park, H. B.; Robertson, G. P.; Dal-Cin, M. M.; Visser, T.; Scoles, L.; Guiver, M. D. *Nat. Mater.* **2011,** *10,* 372. doi:10.1038/nmat2989
17. Weber, J.; Du, N.; Guiver, M. D. *Macromolecules* **2011,** *44,* 1763. doi:10.1021/ma101447h
18. Özdemir, E.; Thirion, D.; Yavuz, C. T. *RSC Adv.* **2015,** *5,* 69010. doi:10.1039/C5RA10697D
19. Yuan, D.; Lu, W.; Zhao, D.; Zhou, H.-C. *Adv. Mater.* **2011,** *23,* 3723. doi:10.1002/adma.201101759
20. Zulfiqar, S.; Karadas, F.; Park, J.; Deniz, E.; Stucky, G. D.; Jung, Y.; Atilhan, M.; Yavuz, C. T. *Energy Environ. Sci.* **2011,** *4,* 4528. doi:10.1039/c1ee02264d
21. Sihn, Y. H.; Byun, J.; Patel, H. A.; Lee, W.; Yavuz, C. T. *RSC Adv.* **2016,** *6,* 45968. doi:10.1039/C6RA06807C
22. Kitagawa, S.; Kitaura, R.; Noro, S.-i. *Angew. Chem., Int. Ed.* **2004,** *43,* 2334. doi:10.1002/anie.200300610

23. Batten, S. R.; Robson, R. *Angew. Chem., Int. Ed.* **1998,** *37,* 1460. doi:10.1002/(SICI)1521-3773(19980619)37:11<1460::AID-ANIE1460>3.0.CO;2-Z
Angew. Chem. **1998,** *110,* 1558. doi:10.1002/(SICI)1521-3757(19980605)110:11<1558::AID-ANGE1558>3.0.CO;2-7
24. Islamoğlu, T.; Rabbani, M. G.; El-Kaderi, H. M. *J. Mater. Chem. A* **2013,** *1,* 10259. doi:10.1039/c3ta12305g
25. Thirion, D.; Rozyyev, V.; Park, J.; Byun, J.; Jung, Y.; Atilhan, M.; Yavuz, C. T. *Phys. Chem. Chem. Phys.* **2016,** *18,* 14177. doi:10.1039/C6CP01382A
26. Fracaroli, A. M.; Furukawa, H.; Suzuki, M.; Dodd, M.; Okajima, S.; Gándara, F.; Reimer, J. A.; Yaghi, O. M. *J. Am. Chem. Soc.* **2014,** *136,* 8863. doi:10.1021/ja503296c
27. Boot-Handford, M. E.; Abanades, J. C.; Anthony, E. J.; Blunt, M. J.; Brandani, S.; Mac Dowell, N.; Fernández, J. R.; Ferrari, M.-C.; Gross, R.; Hallett, J. P.; Haszeldine, R. S.; Heptonstall, P.; Lyngfelt, A.; Makuch, Z.; Mangano, E.; Porter, R. T. J.; Pourkashanian, M.; Rochelle, G. T.; Shah, N.; Yao, J. G.; Fennell, P. S. *Energy Environ. Sci.* **2014,** *7,* 130. doi:10.1039/C3EE42350F
28. Porcheron, F.; Gibert, A.; Mougin, P.; Wender, A. *Environ. Sci. Technol.* **2011,** *45,* 2486. doi:10.1021/es103453f

License and Terms

BEILSTEIN JOURNAL OF ORGANIC CHEMISTRY

Synthesis of three-dimensional porous hyper-crosslinked polymers via thiol–yne reaction

Mathias Lang[1], Alexandra Schade[1] and Stefan Bräse[*1,2]

Full Research Paper

Open Access

Address:
[1]Institute of Organic Chemistry, Karlsruhe Institute of Technology – Campus South, Fritz-Haber-Weg 6, 76131 Karlsruhe, Germany and [2]Institute of Toxicology and Genetics, Karlsruhe Institute of Technology – Campus North, Hermann-von-Helmholtz-Platz 1, 76344 Eggenstein-Leopoldshafen, Germany

Email:
Stefan Bräse[*] - bräse@kit.edu

* Corresponding author

Keywords:
three-dimensional; porous hyper-crosslinked polymers; thiol–yne

Beilstein J. Org. Chem. **2016,** *12,* 2570–2576.
doi:10.3762/bjoc.12.252

Received: 03 August 2016
Accepted: 15 November 2016
Published: 29 November 2016

This article is part of the Thematic Series "Organic porous materials".

Associate Editor: H. Ritter

Abstract

Herein we report the syntheses of two porous hyper-crosslinked polymers (HCPs) via thiol–yne reaction with rigid tetrahedral and *pseudo*-octahedral core structures. Sorption measurements with nitrogen gas at 77 K revealed BET-surface areas up to 650 m²/g. Those networks also showed a high thermal stability as well as insolubility in common organic solvents.

Introduction

The synthesis of different organic networks has been previously reported. Among them, especially tetraphenylmethane cores are widely employed in the synthesis of covalent organic frameworks (COFs) [1,2], porous aromatic frameworks (PAFs) [3], porous polymer networks (PPNs) [4] and hyper-crosslinked polymers (HCPs) [5]. These organic networks are, due to their large surface areas, of interest in gas storage [6], gas separation [7] and catalysis [8-10]. For the synthesis of organic networks, many different reaction types such as condensation reactions [11,12], coupling reactions [3] and click reactions [5,13] have been reported. Herein we present the synthesis of porous, three-dimensional tetraphenylmethane-based networks by another click reaction, the thiol–yne reaction [14-19]. This reaction type has been known for several decades and relived a renaissance in the past decade, especially in material sciences [20-32], due to its mild, and metal-free reaction conditions, high yields and easy purification.

Results and Discussion

The first network shown here was synthesized by crosslinking the two tetrahedral tetraphenylmethane core structures **1** and **2** via the radical-mediated thiol–yne reaction using AIBN as initiator. The second network was synthesized with tetraphenylmethane core **2** and the *pseudo*-octahedral bistritylbenzene core **4** under the same reaction conditions (Scheme 1). The resulting HCPs **3** and **5** were obtained in 90% and 95% yields, respec-

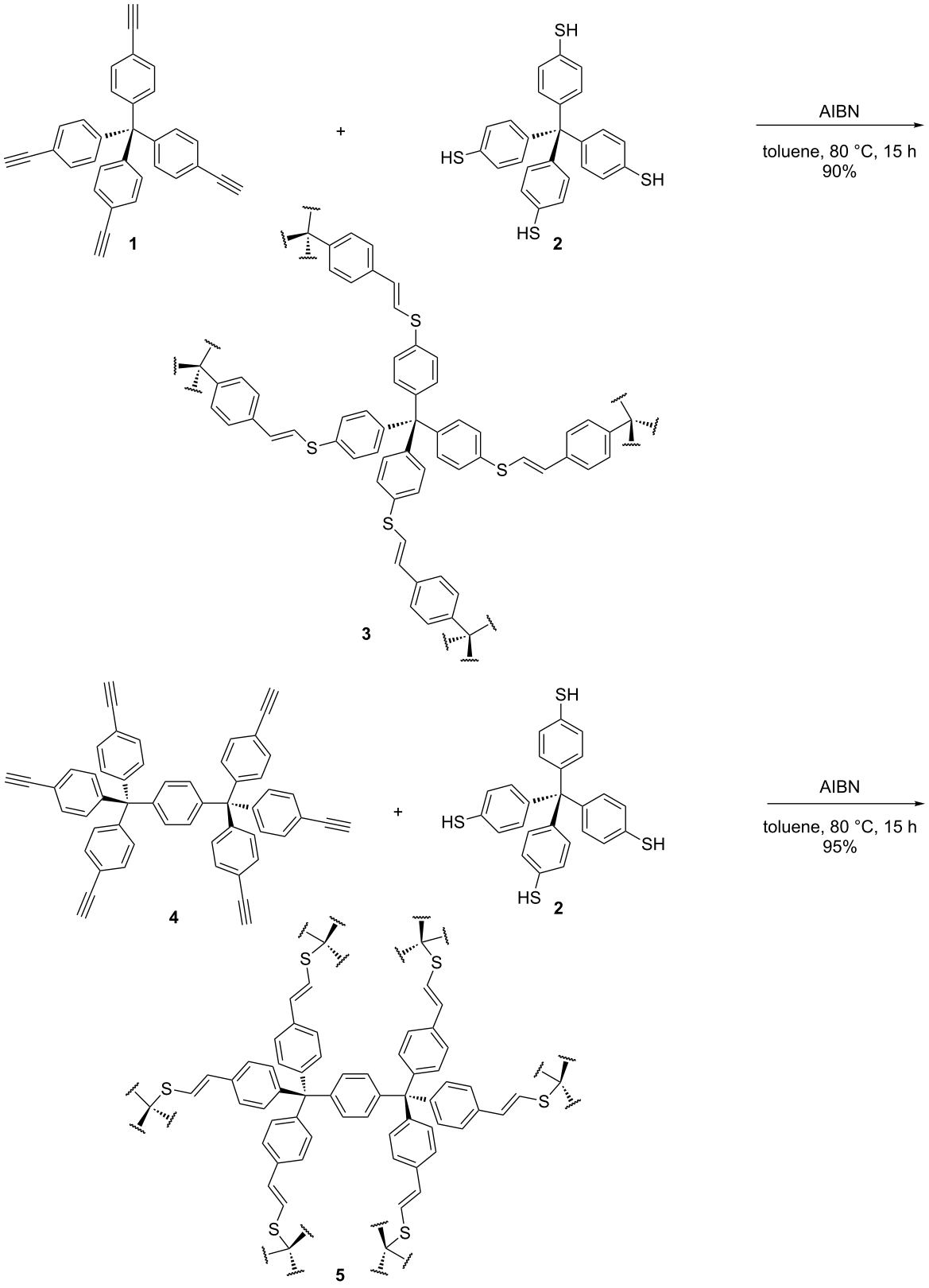

Scheme 1: Syntheses of the HCPs **3** and **5** via thiol–yne reaction.

tively. Both HCPs showed complete insolubility in common organic solvents. The monomers **1** [13], **2** [33] and **4** [34] were synthesized according to literature procedures.

The structures of HCPs **3** and **5** were analysed by elemental analysis and IR spectroscopy. The IR spectra of the monomers show the characteristic vibration bands of alkynes at 3300 cm^{-1} and the vibration band at 2550 cm^{-1} of thiols, respectively. However, these characteristic bands are nearly extinguished in the IR spectra of the HCPs showing a high ratio of crosslinking for these reactions. In addition, the vibration bands of the HCPs at 3000 cm^{-1} correspond to the presence of olefinic bonds, which is in accordance to a monoaddition of a thiol to an alkyne. The absence of a vibration band at 2900 cm^{-1} reveals that there are no saturated fragments in the HCPs, again showing that only a monoaddition and no further addition to the corresponding thioacetal or 1,2-disulfide took place (Figure 1 and Figure 2).

The elemental analyses (Table 1) of networks **3** and **5** showed equimolar turnover regarding the number of functional groups of the monomers. Further, TGA measurements showed a high thermal stability of the HCPs. The TGA curves of HCP **3** and **5** are shown in Supporting Information File 1, Figures S5 and S6.

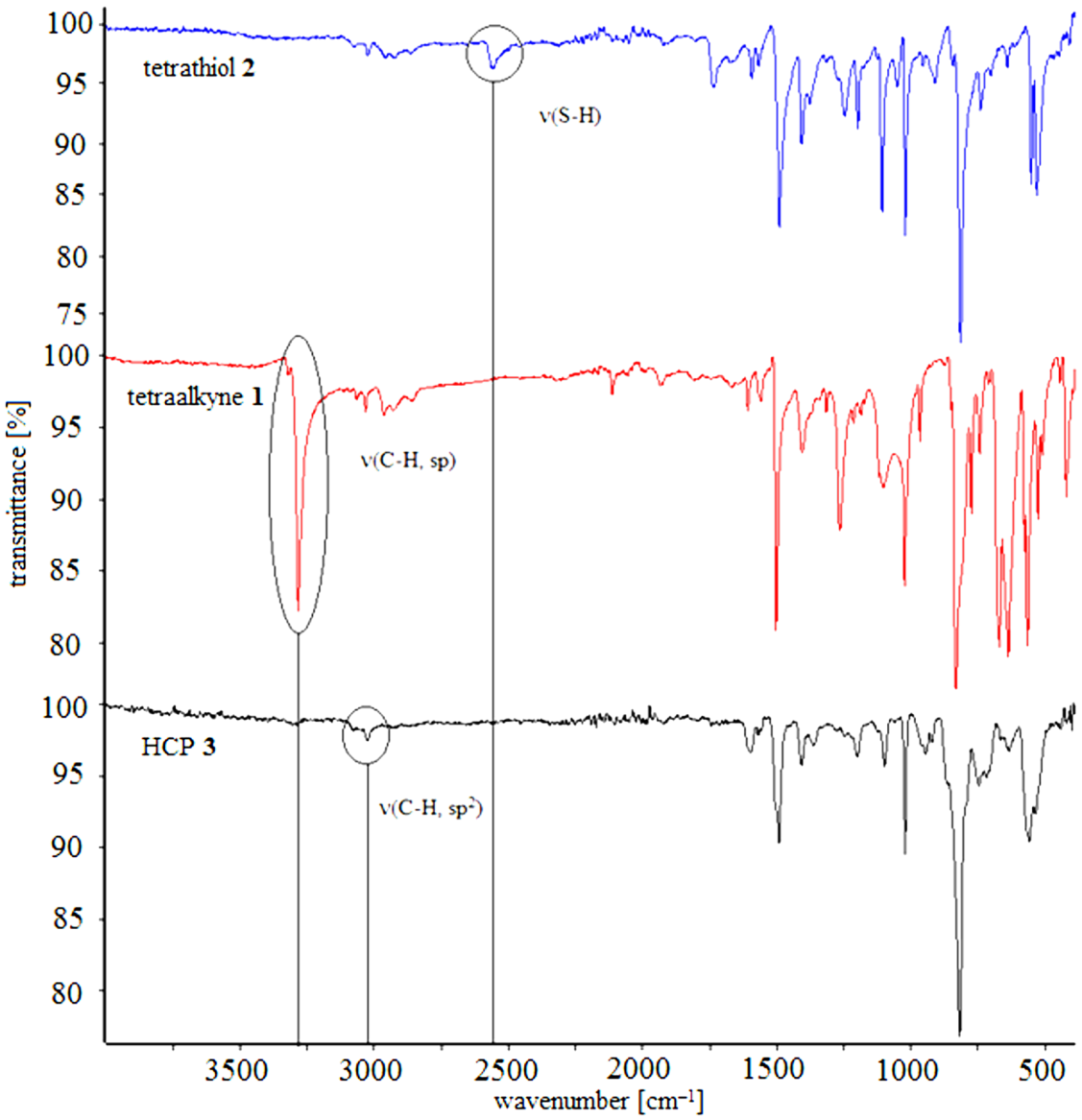

Figure 1: IR-spectra of tetrathiol **2** (blue), tetraalkyne **1** (red) and HCP **3** (black).

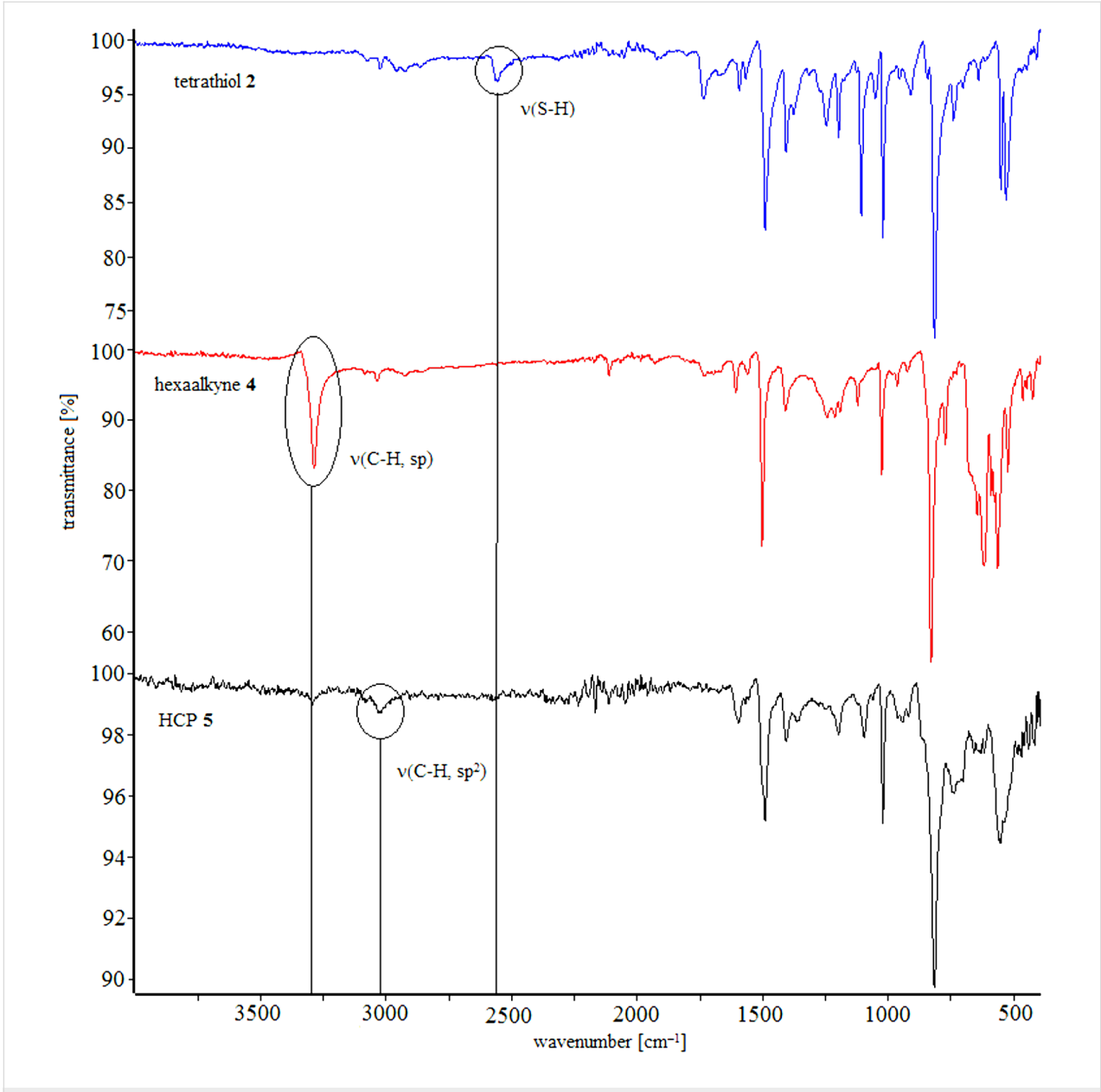

Figure 2: IR-spectra of tetrathiol **2** (blue), hexaalkyne **4** (red) and HCP **3** (black).

Table 1: Elemental analyses of HCPs **3** and **5**.

		C	H	S
HCP **3**	calcd.	80.52	4.66	14.84
	found	79.06	4.71	14.55
HCP **5**	calcd.	81.38	4.68	13.94
	found	79.34	4.49	13.20

The SEM pictures (Figure 3) show the amorphous character of the HCPs, which is consistent with the PXRD measurements (see Supporting Information File 1, Figures S3 and S4). The SEM pictures also reveal that HCP **3** consists of particles in the micrometer range while the particle size of HCP **5** is in the sub-micrometre area.

Furthermore, adsorption measurements of HCPs **3** and **5** were carried out with nitrogen gas at 77 K after pre-drying for 16 h at 80 °C in vacuum. Both HCPs showed BET-surface areas >400 m^2/g and the values of the specific surface area and cumulative volumes of the HCPs are collected in Table 2. The corresponding adsorption isotherms are depicted in Figure 4. The strong slope of the isotherms at low relative pressures indicates a permanent porous character of the materials. Also the step

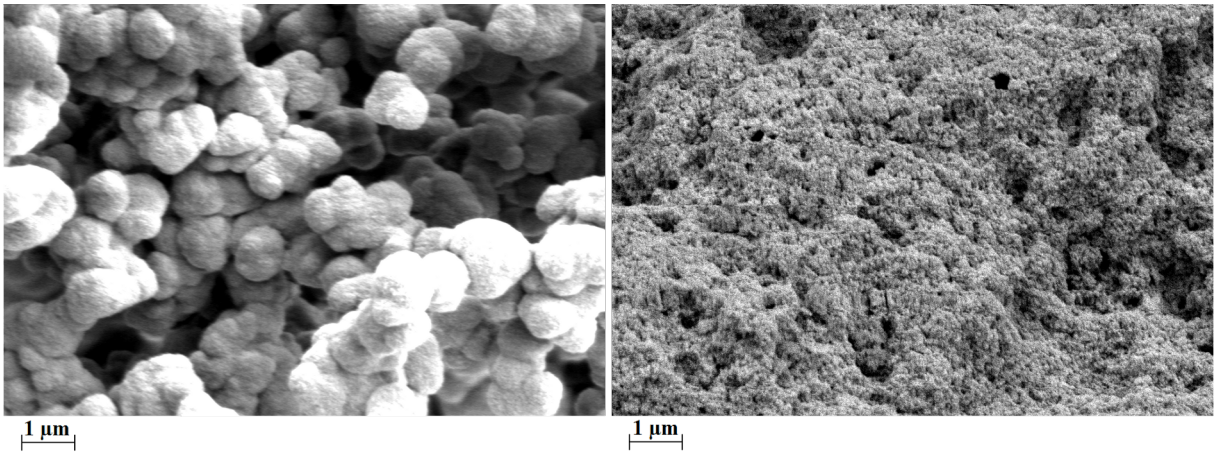

Figure 3: SEM images of HCP **3** (left) and HCP **5** (right).

Table 2: Data of adsorption measurements of HCPs **3** and **5**.

HCP	Specific surface area[a] (BET) [m²/g]	Specific surface area[a] (Langmuir) [m²/g]	Cumulative volume[b] [cm³/g]
3	470	696	0.314
5	650	989	0.510

[a]Surface areas were calculated at a relative pressure range of p/p^0 = 0.05–0.3. [b]Cumulative volumes were calculated at a relative pressure of p/p^0 = 0.35–0.95 using the Horvat & Kavazoe method.

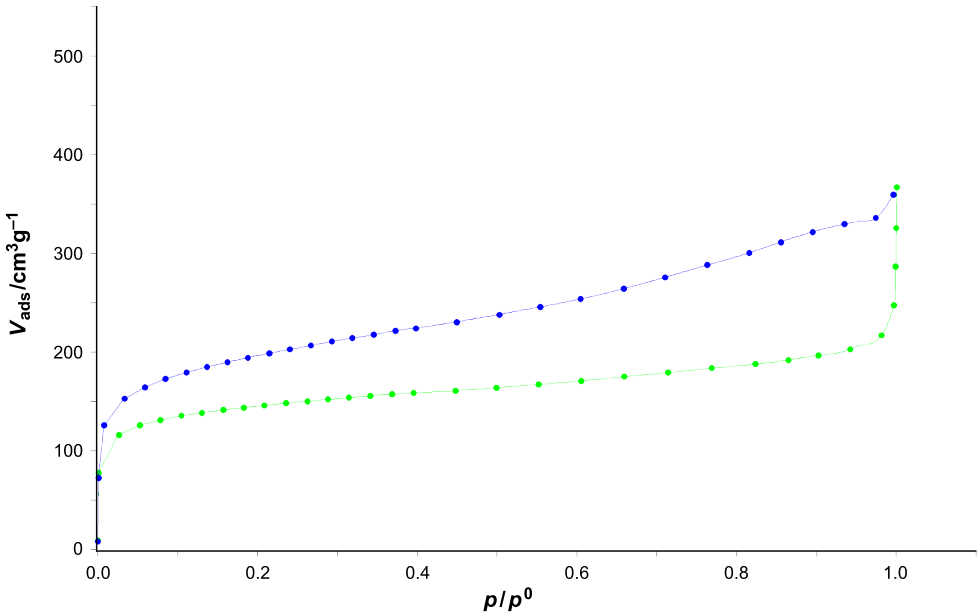

Figure 4: Adsorption isotherms of HCP **3** (green) and HCP **5** (blue) with nitrogen at 77 K. Desorption isotherms are not shown for the sake of improved clarity; they can be viewed in Supporting Information File 1, Figures S1 and S2.

around $p/p^0 = 0.5$ at desorption isotherms (Supporting Information File 1, Figures S1 and S2) indicates the mesoporous character of HCPs **3** and **5**. The low-pressure hysteresis is most probable due to swelling effects or ill-connected pores. The pore-size distributions of HCPs **3** and **5** both show a broad distribution in the microporous scale as well as in the mesoporous scale. These findings also point out that both HCPs have amorphous character as the networks are built up by an irreversible reaction leading to kinetically controlled networks with different sizes of the pores, which is in accordance with the PXRD and SEM measurements stated above. The pore-size distributions of HCPs **3** and **5** are illustrated in Supporting Information File 1 (Figure S8 and S9, respectively).

Conclusion

Herein we synthesised amorphous porous tetraphenylmethane-based organic hyper-crosslinked polymers (HCPs) through the thiol–yne reaction. The use of this versatile method reveals advantages such as high yields, cost effectiveness and metal-free crosslinking reaction conditions. The obtained HCPs showed BET surface areas up to 650 m²/g and are insoluble in common organic solvents. The characterisation of the networks was performed using IR spectroscopy, elemental analysis, thermogravimetric analysis (TGA), scanning electron microscopy (SEM), powder X-ray diffraction (PXRD) and adsorption measurements using nitrogen at 77 K.

Supporting Information

Supporting Information File 1

Experimental procedures and additional measurements.
[http://www.beilstein-journals.org/bjoc/content/supplementary/1860-5397-12-252-S1.pdf]

Acknowledgements

This research was financially supported by the Landesgraduiertenförderung Baden-Württemberg. We also gratefully acknowledge U. Geckle (IAM-EE, KIT), Dr. Manuel Tsotsalas (IFG, KIT) and Dr. Thomas Biet (INT, KIT) for their help.

References

1. El-Kaderi, H. M.; Hunt, J. R.; Mendoza-Cortés, J. L.; Côté, A. P.; Taylor, R. E.; O'Keeffe, M.; Yaghi, O. M. *Science* **2007,** *316,* 268–272. doi:10.1126/science.1139915
2. Uribe-Romo, F. J.; Hunt, J. R.; Furukawa, H.; Klöck, C.; O'Keeffe, M.; Yaghi, O. M. *J. Am. Chem. Soc.* **2009,** *131,* 4570–4571. doi:10.1021/ja8096256
3. Ben, T.; Ren, H.; Ma, S.; Cao, D.; Lan, J.; Jing, X.; Wang, W.; Xu, J.; Deng, F.; Simmons, J. M.; Qiu, S.; Zhu, G. *Angew. Chem., Int. Ed.* **2009,** *48,* 9457–9460. doi:10.1002/anie.200904637
4. Lu, W.; Yuan, D.; Zhao, D.; Schilling, C. I.; Plietzsch, O.; Muller, T.; Bräse, S.; Guenther, J.; Blümel, J.; Krishna, R.; Li, Z.; Zhou, H.-C. *Chem. Mater.* **2010,** *22,* 5964–5972. doi:10.1021/cm1021068
5. Plietzsch, O.; Schilling, C. I.; Grab, T.; Grage, S. L.; Ulrich, A. S.; Comotti, A.; Sozzani, P.; Muller, T.; Bräse, S. *New J. Chem.* **2011,** *35,* 1577–1581. doi:10.1039/c1nj20370c
6. Ben, T.; Pei, C.; Zhang, D.; Xu, J.; Deng, F.; Jing, X.; Qiu, S. *Energy Environ. Sci.* **2011,** *4,* 3991–3999. doi:10.1039/c1ee01222c
7. Lindemann, P.; Tsotsalas, M.; Shishatskiy, S.; Abetz, V.; Krolla-Sidenstein, P.; Azucena, C.; Monnereau, L.; Beyer, A.; Gölzhäuser, A.; Mugnaini, V.; Gliemann, H.; Bräse, S.; Wöll, C. *Chem. Mater.* **2014,** *26,* 7189–7193. doi:10.1021/cm503924h
8. Ma, P.; Lv, L.; Zhang, M.; Yuan, Q.; Cao, J.; Zhu, C. *J. Porous Mater.* **2015,** *22,* 1567–1571. doi:10.1007/s10934-015-0039-1
9. Kaur, P.; Hupp, J. T.; Nguyen, S. T. *ACS Catal.* **2011,** *1,* 819–835. doi:10.1021/cs200131g
10. Zhang, K.; Farha, O. K.; Hupp, J. T.; Nguyen, S. T. *ACS Catal.* **2015,** *5,* 4859–4866. doi:10.1021/acscatal.5b01388
11. Rabbani, M. G.; Sekizkardes, A. K.; Kahveci, Z.; Reich, T. E.; Ding, R.; El-Kaderi, H. M. *Chem. – Eur. J.* **2013,** *19,* 3324–3328. doi:10.1002/chem.201203753
12. Côté, A. P.; Benin, A. I.; Ockwig, N. W.; O'Keeffe, M.; Matzger, A. J.; Yaghi, O. M. *Science* **2005,** *310,* 1166–1170. doi:10.1126/science.1120411
13. Pandey, P.; Farha, O. K.; Spokoyny, A. M.; Mirkin, C. A.; Kanatzidis, M. G.; Hupp, J. T.; Nguyen, S. T. *J. Mater. Chem.* **2011,** *21,* 1700–1703. doi:10.1039/c0jm03483e
14. Lowe, A. B. *Polymer* **2014,** *55,* 5517–5549. doi:10.1016/j.polymer.2014.08.015
15. Massi, A.; Nanni, D. *Org. Biomol. Chem.* **2012,** *10,* 3791–3807. doi:10.1039/c2ob25217a
16. Griebenow, N.; Bräse, S.; Dilmac, A. M. *RSC Adv.* **2015,** *5,* 54301–54303. doi:10.1039/C5RA08787B
17. Hoogenboom, R. *Angew. Chem., Int. Ed.* **2010,** *49,* 3415–3417. doi:10.1002/anie.201000401
18. Feng, W.; Li, L.; Ueda, E.; Li, J.; Heißler, S.; Welle, A.; Trapp, O.; Levkin, P. A. *Adv. Mater. Interfaces* **2014,** *1,* 1400269. doi:10.1002/admi.201400269
19. Quick, A. S.; de los Santos Pereira, A.; Bruns, M.; Bückmann, T.; Rodriguez-Emmenegger, C.; Wegener, M.; Barner-Kowollik, C. *Adv. Funct. Mater.* **2015,** *25,* 3735–3744. doi:10.1002/adfm.201500683
20. Al Samad, A.; Bakkour, Y.; Fanny, C.; El Omar, F.; Coudane, J.; Nottelet, B. *Polym. Chem.* **2015,** *6,* 5093–5102. doi:10.1039/C5PY00391A
21. Chen, C.; Xu, H.; Qian, Y.-C.; Huang, X.-J. *RSC Adv.* **2015,** *5,* 15909–15915. doi:10.1039/C4RA14012E
22. Durham, O. Z.; Norton, H. R.; Shipp, D. A. *RSC Adv.* **2015,** *5,* 66757–66766. doi:10.1039/C5RA12553G
23. Lee, H.; Kim, H.; Choi, T. J.; Park, H. W.; Chang, J. Y. *Chem. Commun.* **2015,** *51,* 9805–9808. doi:10.1039/C5CC02269J
24. Martella, D.; Parmeggiani, C.; Wiersma, D. S.; Piñol, M.; Oriol, L. *J. Mater. Chem. C* **2015,** *3,* 9003–9010. doi:10.1039/C5TC01290B
25. Pötzsch, R.; Stahl, B. C.; Komber, H.; Hawker, C. J.; Voit, B. I. *Polym. Chem.* **2014,** *5,* 2911–2921. doi:10.1039/c3py01740k
26. Sprafke, J. K.; Spruell, J. M.; Mattson, K. M.; Montarnal, D.; McGrath, A. J.; Pötzsch, R.; Miyajima, D.; Hu, J.; Latimer, A. A.; Voit, B. I.; Aida, T.; Hawker, C. J. *J. Polym. Sci., Part A: Polym. Chem.* **2015,** *53,* 319–326. doi:10.1002/pola.27345

27. Sardo, C.; Nottelet, B.; Triolo, D.; Giammona, G.; Garric, X.; Lavigne, J.-P.; Cavallaro, G.; Coudane, J. *Biomacromolecules* **2014,** *15,* 4351–4362. doi:10.1021/bm5013772
28. van Hensbergen, J. A.; Burford, R. P.; Lowe, A. B. *Polym. Chem.* **2014,** *5,* 5339–5349. doi:10.1039/C4PY00604F
29. Wei, Q.; Pötzsch, R.; Komber, H.; Pospiech, D.; Voit, B. *Polymer* **2014,** *55,* 5600–5607. doi:10.1016/j.polymer.2014.07.030
30. Yao, B.; Mei, J.; Li, J.; Wang, J.; Wu, H.; Sun, J. Z.; Qin, A.; Tang, B. Z. *Macromolecules* **2014,** *47,* 1325–1333. doi:10.1021/ma402559a
31. Zhao, B.; Zheng, Y.; Weng, Z.; Cai, S.; Gao, C. *Polym. Chem.* **2015,** *6,* 3747–3753. doi:10.1039/C5PY00307E
32. Zuo, Y.; Wang, D.; Zhang, J.; Feng, S. *RSC Adv.* **2014,** *4,* 62827–62834. doi:10.1039/C4RA13620A
33. Plietzsch, O.; Schade, A.; Hafner, A.; Huuskonen, J.; Rissanen, K.; Nieger, M.; Muller, T.; Bräse, S. *Eur. J. Org. Chem.* **2013,** 283–299. doi:10.1002/ejoc.201201162
34. Monnereau, L.; Nieger, M.; Muller, T.; Bräse, S. *Adv. Funct. Mater.* **2014,** *24,* 1054–1058. doi:10.1002/adfm.201302483

License and Terms

BEILSTEIN JOURNAL OF ORGANIC CHEMISTRY

Supramolecular frameworks based on [60]fullerene hexakisadducts

Andreas Kraft[1], Johannes Stangl[2], Ana-Maria Krause[1], Klaus Müller-Buschbaum[2] and Florian Beuerle[*1,§]

Full Research Paper

Open Access

Address:
[1]Institut für Organische Chemie & Center for Nanosystems Chemistry, Universität Würzburg, Am Hubland, 97074 Würzburg, Germany and [2]Institut für Anorganische Chemie, Universität Würzburg, Am Hubland, 97074 Würzburg, Germany

Email:
Florian Beuerle[*] - florian.beuerle@uni-wuerzburg.de

* Corresponding author
§ Tel.: +49 931 31-83603

Keywords:
fullerenes; hexakisadducts; hydrogen bonding; porous materials; structure elucidation

Beilstein J. Org. Chem. **2017,** *13,* 1–9.
doi:10.3762/bjoc.13.1

Received: 11 August 2016
Accepted: 08 December 2016
Published: 02 January 2017

This article is part of the Thematic Series "Organic porous materials".

Guest Editor: S. Bräse

Abstract

[60]Fullerene hexakisadducts possessing 12 carboxylic acid side chains form crystalline hydrogen-bonding frameworks in the solid state. Depending on the length of the linker between the reactive sites and the malonate units, the distance of the [60]fullerene nodes and thereby the spacing of the frameworks can be controlled and for the most elongated derivative, continuous channels are obtained within the structure. Stability, structural integrity and porosity of the material were investigated by powder X-ray diffraction, thermogravimetry and sorption measurements.

Introduction

The utilization of confined nanospace in rigid frameworks [1], which are derived from small molecular precursors under dynamic conditions, has emerged as a novel design paradigm for functional materials with the prospect of applications in gas storage [2,3], catalysis [4,5], luminescence [6-9] and sensing [10-13] or optoelectronics [14-16]. Owing to a modular approach, building blocks and cross-linking interactions can be varied over a wide range resulting in metal-organic frameworks (MOFs) [17,18], covalent organic frameworks (COFs) [19,20] or covalent organic cage compounds [21-28] as the most prominent examples for such artificial porous materials. Purely organic systems such as COFs usually benefit from very low densities, high thermal stabilities and metal-free synthesis, but in most cases, have the disadvantages of poor crystallinity and limited processability or solution-phase characterization. In contrast, the formation of robust porous structures by means of supramolecular interactions between rigid organic molecules might be a promising alternative thus combining low-weight materials with easy processing. However, the crystallization of stable organic structures possessing permanent porosity is still

quite challenging and only a limited number of examples for supramolecular crystals based on hydrogen bonding [29-45] or π–π-stacking [46] that retain porosity in the solid state under activation conditions have been reported so far. One possible way to enhance stability and shape-persistency might be the implementation of polyfunctional building blocks in order to strengthen the non-covalent interactions in a cooperative manner. In this regard, [60]fullerene hexakisadducts [47], which can arrange up to twelve functional sites with icosahedral symmetry, exhibit one of the highest degrees of functionalization for organic molecules (see Figure 1). In recent years, a variety of derivatives have been synthesized as spherical branching units [48-53] and, more recently, functionalized fullerene derivatives have been implemented into coordination compounds [54-56]. However, to the best of our knowledge, no fullerene-containing crystalline frameworks retaining permanent porosity in the solvent-free state have been reported so far.

Here, we report on the crystallization of three-dimensional hydrogen-bonding frameworks based on [60]fullerene hexakisadducts bearing twelve carboxylic acid groups icosahedrally arranged on the fullerene surface. By varying the spacer length, the solvent-filled pore systems in the solid-state structures have been tuned and structural features such as porosity of the materials have been investigated by PXRD, TGA analysis and sorption studies.

Results and Discussion

Recently, we reported on the synthesis and solid-state structure of dodecaacid **C2** (**C*n*** stands for T_h symmetrical hexakisadducts $C_{60}\{C[COO(CH_2)_{n-1}COOH]_2\}_6$, see Figure 1) revealing a complex hydrogen-bonding network in the crystalline state [57]. Based on this initial finding, we also utilized **C2** and elongated derivative **C3** as organic connectivity centers in metal-organic assemblies obtained after reaction with Zn^{2+} ions [55], however, no crystal structure of metal-free **C3** has been reported yet. As a general packing motif for all fullerene-containing frameworks, the individual carbon building blocks are arranged in face centered cubic (fcc) packing with the distances between the molecules depending on the spacer length and the mode of cross-linking. For **HFF-1** (hydrogen-bonded fullerene framework) derived from **C2**, a densely packed structure is observed possessing only very small cavities within the octahedral sites of the fcc packing filled with one CH_2Cl_2 molecule (Figure 2a) [57].

In order to obtain porous supramolecular materials, we wondered if elongation of the alkyl spacers may result in increased fullerene–fullerene spacing associated with an enlargement of the cavitities and potential formation of a connected pore system. Therefore, we aimed for the crystallization of **C3** and also synthesized the next homologue **C4** starting from malonate **1** [59] according to a standard two-step protocol via a sixfold Bingel reaction followed by acidic deprotection (Scheme 1). As we observed the insertion of MeOH molecules into the hydrogen-bonding network of **HFF-1** [57], we also tested other polar solvents for crystallization in order to strengthen the supramolecular interactions that hold the networks together. For both **C3** and **C4**, we could finally grow single crystals suitable for X-ray diffraction by slow vapor

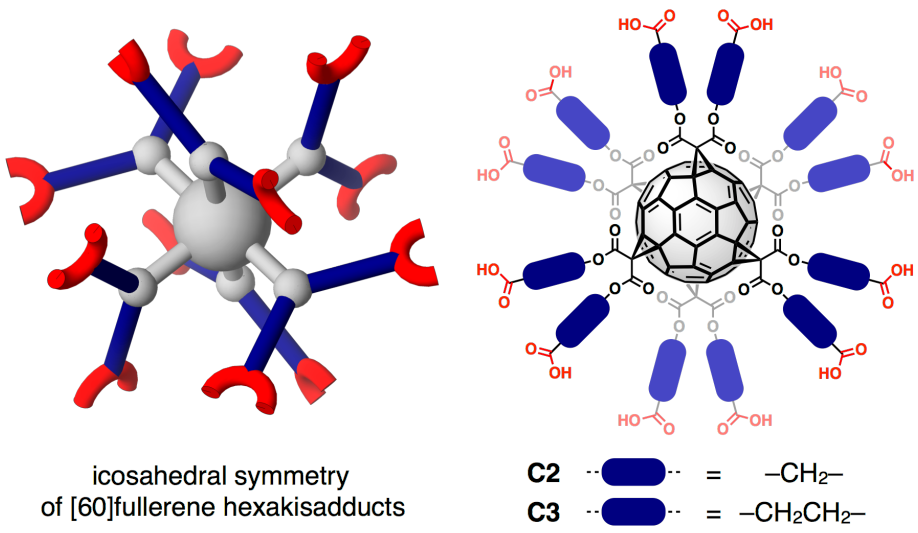

Figure 1: Icosahedral arrangement of functional addends for [60]fullerene hexakisadducts with dodecaacids **C2** and **C3** as prototypical examples for such carbon nanostructures.

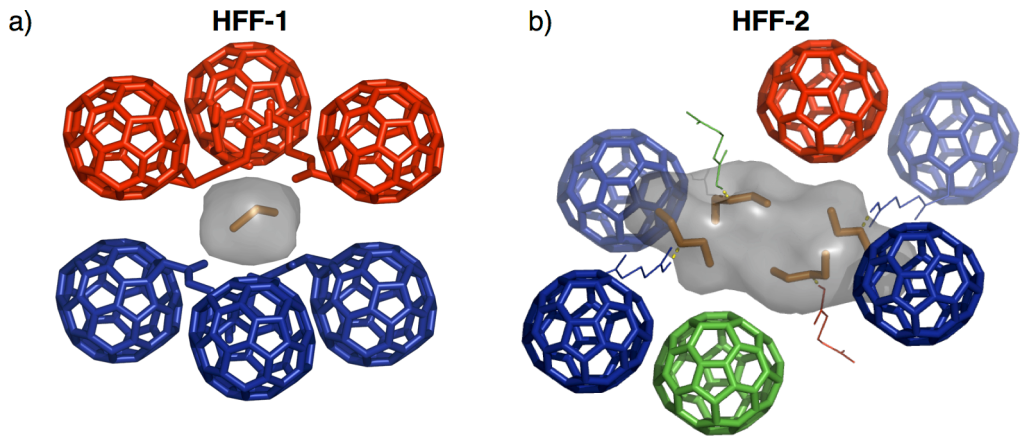

Figure 2: a) Small cavities within the octahedral sites of **HFF-1** filled with one CH_2Cl_2 molecule [57]; b) isolated cavities containing four Et_2O molecules for **HFF-2** (void spaces are indicated as grey surfaces and most side arms are omitted for clarity, images are created with PyMOL [58]).

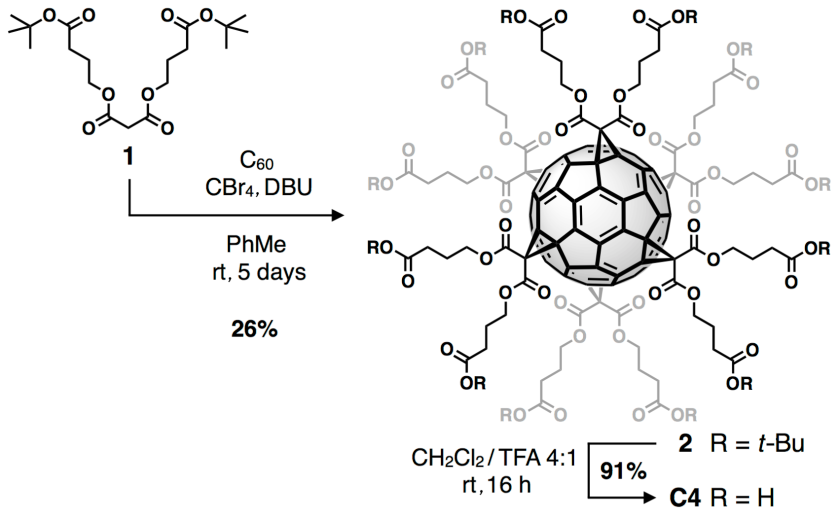

Scheme 1: Synthesis of [60]fullerene dodecaacid **C4**.

deposition of Et_2O into EtOH solutions of both fullerene derivatives thus resulting in the formation of frameworks **HFF-2** and **HFF-3**, respectively.

HFF-2 crystallizes in the triclinic space group $P\bar{1}$ with the composition [**C3**$(Et_2O)_4$] [60]. Despite the lower symmetry compared to **HFF-1**, the packing of **HFF-2** can still be described as a fcc arrangement of **C3** molecules, which are cross-linked by hydrogen bonding. Thereby, six of the twelve side arms form linear COOH dimers (four intralayer and two interlayer) and two carboxylic acids are bound to malonate ester groups from adjacent layers (see Figure S10 in Supporting Information File 1). The remaining four carboxylic acid side chains do not participate but rather coordinate one Et_2O molecule each, resulting in the formation of larger cavities filled with four solvent molecules (Figure 2b). Yet, these voids are still separated from each other and therefore not accessible for solvent exchange and porosity. Then again, dodecaacid **C4** possessing elongated butyric acid side chains crystallizes in the trigonal space group $R\bar{3}$ with the composition [**C4**]·6Et_2O [61] exhibiting a flattened fcc arrangement of **C4** molecules. Figure 3 illustrates the effect of spacer elongation on the fullerene distances, thus leading to larger intralayer spacing and shorter interlayer distances with increasing length of the alkyl spacers separating the hydrogen bonding sites from the malonate units.

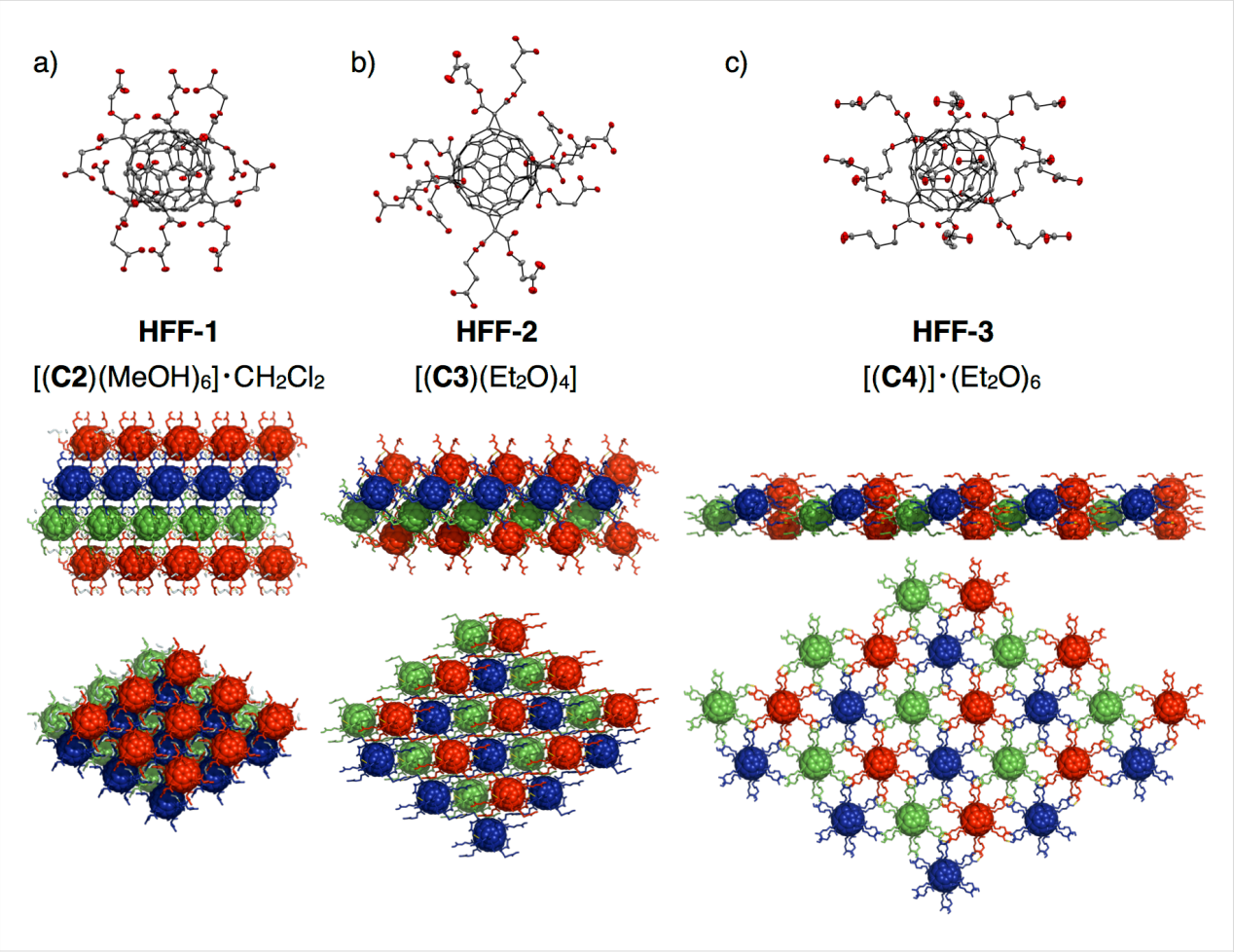

Figure 3: Face centered cubic arrangement of [60]fullerene dodecaacids for frameworks a) **HFF-1** [57], b) **HFF-2** and c) **HFF-3**: ORTEP representation of fullerene monomers (top, thermal ellipsoids set to 50% probability, carbon grey, oxygen red, hydrogen atoms omitted for clarity), side view indicating ABC-type packing (center) and top view indicating enlarged intralayer spacing for elongated derivatives (bottom); images are created with PyMOL [58].

For **HFF-3**, the butyric acid side arms are stretched out and form six pairs of carboxylic acid dimers with their closest neighbors from the next but one layers (left part of Figure 4). Interestingly, this packing motif results in the interpenetration of two independent hydrogen bonding networks (indicated in purple and cyan in Figure 5). Therefore, the individual layers are densely packed exhibiting linear columns of fullerenes in van-der-Waals distance alternating from the two interpenetrated frameworks (right part of Figure 4 and Figure 5). On the other hand, due to the large intralayer spacing and the linear stretching of the side chains, a continuous pore system is formed along the c axis (right part of Figure 4), which is filled with Et_2O molecules that are not bound to any carboxlic acids and may therefore be removable upon activation.

In order to elaborate on the materials properties, we synthesized **HFF-3** in bulk amounts and studied the thermal stability and sorption properties of this framework. The framework crystallizes as anisotropic needles and PXRD measurements in combination with BFDH morphology calculations indicated the structural integrity of the material and the fact that the pore channels are located along the long fiber axis (see Figure S15 in Supporting Information File 1). Thermal treatment of crystalline samples under a microscope indicated partial disintegration and cracking of the crystals at elevated temperatures above 40 °C, presumably due to the removal of solvent molecules. At 198 °C, melting of the crystals occurs (see Figure S12 in the Supporting Information File 1). These findings were also confirmed by TG/DTA measurements for both as-synthesized and preactivated (evacuation at 70 °C) samples, thus showing a weight loss of up to 16% for the nonactivated material after heating to 180 °C followed by an endothermic signal indicating melting of the crystals (see Figure S17 in Supporting Information File 1). Elemental analysis of an activated sample is in perfect agreement with a solvent-free structure (see Experimental section).

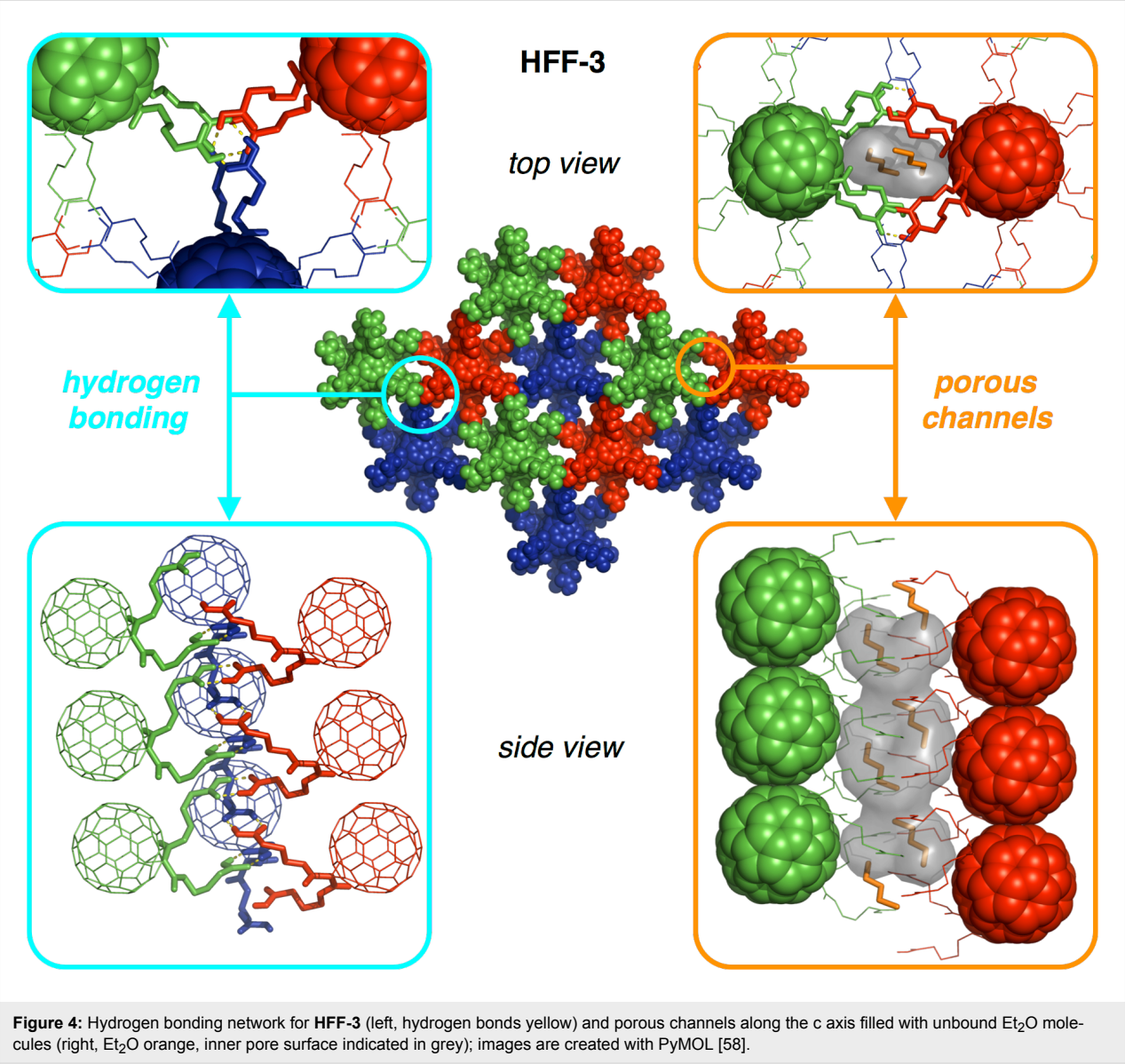

Figure 4: Hydrogen bonding network for **HFF-3** (left, hydrogen bonds yellow) and porous channels along the c axis filled with unbound Et_2O molecules (right, Et_2O orange, inner pore surface indicated in grey); images are created with PyMOL [58].

In order to activate **HFF-3** and to utilize the channel system for porosity, the compound was activated for 48 hours at different stages of vacuum (10^{-3} to 10^{-6} mbar) from room temperature to 70 °C. Sorption properties were determined for N_2 and Ar gas adsorption via a BET study at 77 K. Therein, the framework shows Henry behavior and no microporosity with a surface area of 40 $m^2\ g^{-1}$ for N_2 and only 18 $m^2\ g^{-1}$ for Ar (see Figure S14 in Supporting Information File 1). However, the measured N_2 surface area of 40 $m^2\ g^{-1}$ may indicate that the material still retains some porosity since this value is higher than it would be anticipated for sole coverage of the outer surface of the crystals. Since the channels are aligned along the long fiber axis, kinetic effects might also hamper efficient gas uptake. As this result did not point towards accessible microchannels of the crystal structure, the material was checked for structural and chemical integrity subsequent to activation. As stated, elemental analysis fits very well, so that decomposition is unlikely. Therefore, also SEM investigations by electron microscopy were carried out on activated and non-activated samples of **HFF-3**. They corroborate the strong anisotropic character of crystalline needles of the X-ray structure determination and do not show changes upon activation (see Figure S13 in Supporting in Information File 1). However, powder X-ray diffraction indicates a change in the pattern upon activation (see Figure S16 in Supporting Information File 1). Accordingly, a yet non-identified change in the structure occurs, which may lead to the non-accessibility of the channels. One possible explanation for the observed change upon activation might be that the flexible nature of the alkyl spacers facilitates structural reorganization resulting in a potential blocking of the channels after removal of the solvent mole-

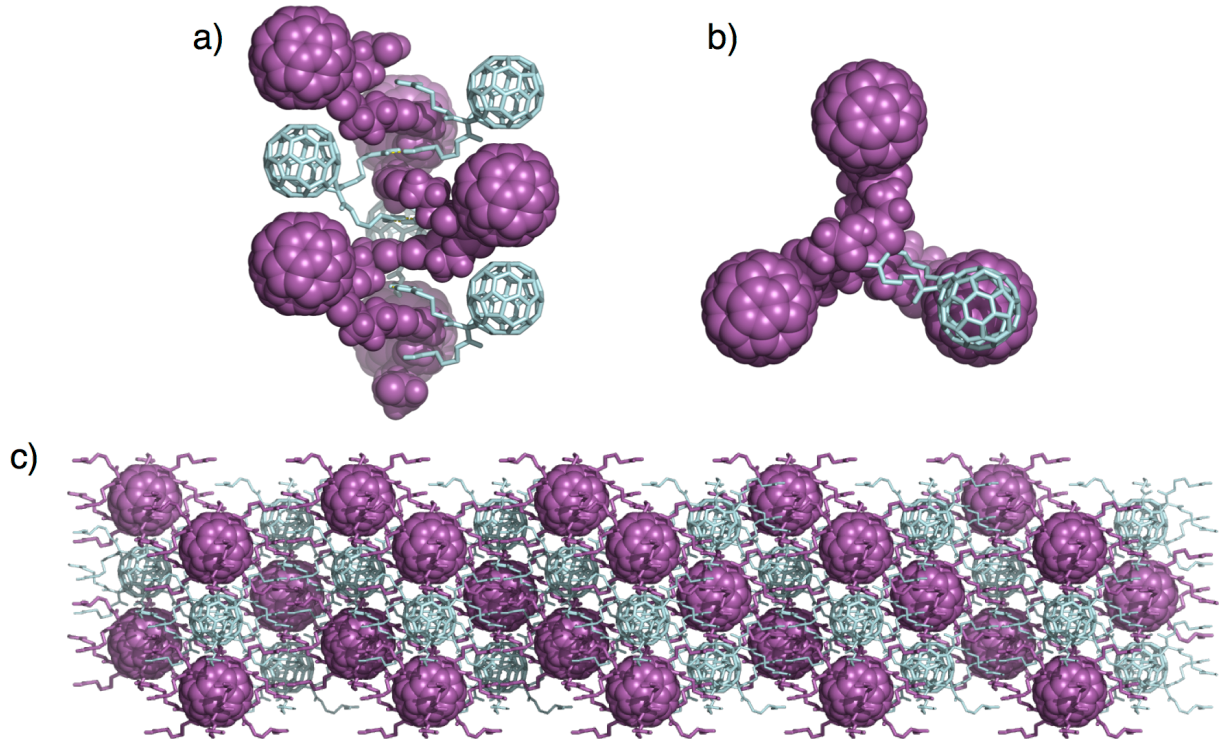

Figure 5: Interpenetration of two distinct hydrogen bonding networks for **HFF-3**: a) side view indicating the spiral staircase-like cross-linking of individual molecules of **C4**, b) top view and c) side view highlighting the interpenetration of two networks colored in purple and cyan.

cules. The Et_2O molecules appear to play a crucial role for the stabilization of both channel size and shape. For future investigations, the implementation of fullerene derivatives possessing long but rigid spacer units might be beneficial for retaining porosity of such supramolecular crystals.

Conclusion

We have presented the crystallization of two [60]fullerene dodecaacids possessing three-dimensional hydrogen bonding networks **HFF-2** and **HFF-3** in the solid state. Different extensions of the linker arms have been investigated for newly synthesized **C4** and compared to the known **C2** and **C3** lengths. Depending on the length of the linker arms, the distance of the fullerene moieties in the framework compounds increases resulting in a new framework structure and giving rise to the idea of permanent porosity for larger fullerene separation. **HFF-3** shows channels suitable for microporosity. However, during the activation process not only release of the solvent molecules from the channels but also a structural change occurs that leads to a Henry behavior in BET investigations. In order to rigidify the structures and stabilize the pore systems upon solvent removal, novel fullerene derivatives possessing less flexible spacers need to be designed and synthesized. Efforts in this regard are currently in progress in our laboratories.

Experimental

Hexakisadduct **C3** [55] and malonate **1** [59] were synthesized according to literature procedures. X-ray crystallography: Bruker D8 Quest diffractometer with Photon 100 CMOS APS detector and Montel multilayer optics monochromated Cu K_α radiation. PXRD diffraction: Bruker D8 Discovery with 1D-Lynxeye detector using Cu K_α radiation (unsplit $K_{\alpha1}$ + $K_{\alpha2}$ doublet, mean wavelength λ = 154.19pm), reflection and transmission geometry.

Hexakisadduct 2: C_{60} (565 mg, 785 µmol, 1 equiv), malonate **1** (3.10 g, 7.84 mmol, 10 equiv) and CBr_4 (26.0 g, 78.4 mmol, 100 equiv) were dissolved in dry toluene (500 mL). DBU (2.34 mL, 15.7 mmol, 20 equiv, 60 mL solution in dry toluene) was added dropwise within 20 minutes resulting in a color change from purple to dark-red. After additional stirring for five days at room temperature, the mixture was passed through a short silica-pad with ethyl acetate as eluent in order to remove the solvent and traces of unreacted C_{60}. After further column chromatographic separation (SiO_2; toluene/ethyl acetate 10:1), pure hexakisadduct **2** (600 mg, 197 µmol, 25%) was obtained as a yellow crystalline solid. mp >200 °C dec; ^{1}H NMR (400 MHz, $CDCl_3$, rt) δ 1.44 (s, 108H, C(CH_3)$_3$), 1.99 (m, ^3J = 6.8 Hz, 24H, $CH_2CH_2CH_2$), 2.31 (t, ^3J = 7.4 Hz, 24H, CH_2CO_2

t-Bu), 4.30 ppm (t, ^3J = 6.52 Hz, 24H, $CH_2CH_2CO_2t$-Bu); ^{13}C NMR (100 MHz, $CDCl_3$, rt) δ 24.10 (12C, $CH_2CH_2CH_2$), 28.26 (36C, $C(CH_3)_3$), 31.80 (12C, CH_2CO_2 *t*-Bu), 45.25 (6C, $O_2CCH_2CO_2$), 66.17 (12C, $CH_2CH_2CO_2$ *t*-Bu), 69.16 (12C, C_{60} sp^3), 80.72 (12C, $C(CH_3)_3$), 141.15 (24C, C_{60} sp^2), 145.99 (24C, C_{60} sp^2), 163.75 (12C, $O_2CCH_2CO_2$), 171.89 ppm (12C, CO_2 *t*-Bu); UV–vis (CH_2Cl_2) λ: 281, 315 (sh), 334 (sh) nm; MS (MALDI, DCTB, pos) *m/z*: 3038 $[M]^+$; anal, calcd for $C_{174}H_{180}O_{48}$: C, 68.76; H, 5.97; found: C, 68.87; H, 6.09.

Hexakisadduct C4: TFA (1.7 mL) was added to a solution of **2** (250 mg, 86.3 µmol) in CH_2Cl_2 (7 mL). The mixture was stirred for one day at room temperature. The precipitated yellow solid was isolated through decantation. Further purification was carried out by suspending the raw product in CH_2Cl_2, centrifugation and collection through decantation. After drying under high vacuum, hexakisadduct **C4** (185 mg, 78.2 µmol, 91%) was obtained as a light-yellow solid. mp 198 °C; ^{1}H NMR (400 MHz, DMSO-d_6, rt) δ 1.85 (m, 24H, $CH_2CH_2CH_2$), 2.27 (t, 24H, CH_2CO_2H), 4.30 (t, 24H, $COOCH_2$), 12.16 ppm (s br, 12H, CO_2H); ^{13}C NMR (100 MHz, DMSO-d_6, rt) δ 23.47 (12C, CH_2CO_2H), 29.71 (12C, $CH_2CH_2CH_2$), 45.44 (6C, $O_2CCH_2CO_2$), 66.35 (12C, $COOCH_2$), 68.67 (12C, C_{60} sp^3), 140.71 (24C, C_{60} sp^2), 145.02 (24C, C_{60} sp^2), 162.75 (12C, $O_2CCH_2CO_2$), 173.64 ppm (12C, CO_2H); UV–vis (CH_2Cl_2) λ: 281, 315 (sh), 334 (sh) nm; MS (MALDI, DCTB, pos) *m/z*: 2365 $[M]^+$; anal. calcd for $C_{126}H_{84}O_{48}$: C, 63.96; H, 3.58; found: C, 63.96; H, 3.58.

Crystal growth of HFF-2: Single crystals suitable for X-ray diffraction have been obtained by slow vapor deposition of Et_2O into a solution of **C3** in EtOH. CCDC deposition number: 1498265.

Crystal growth of HFF-3: Single crystals suitable for X-ray diffraction have been obtained by slow vapor deposition of Et_2O into a solution of **C4** in EtOH. CCDC deposition number: 1498266.

Supporting Information

Supporting Information File 1

Analytical and crystallographic data; SEM, BET, PXRD and TGA/DTA data.
[http://www.beilstein-journals.org/bjoc/content/supplementary/1860-5397-13-1-S1.pdf]

Acknowledgements

The authors would like to thank Dr. David Schmidt for PXRD measurements and Dr. Fabian Schönfeld (Quantachrome) for discussion on the adsorption behavior. Financal support by the Fonds der Chemischen Industrie (Liebig fellowship for FB), the DFG (SPP 1362/2 "Porous MOFs", BE 4808/ 1-2 and MU 1562/5-2) as well as the Bavarian Ministry of Science, Research and the Arts (Collaboratory Research Network "Solar Technologies Go Hybrid") is gratefully acknowledged.

References

1. Slater, A. G.; Cooper, A. I. *Science* **2015,** *348,* 988. doi:10.1126/science.aaa8075
2. Morris, R. E.; Wheatley, P. S. *Angew. Chem., Int. Ed.* **2008,** *47,* 4966–4981. doi:10.1002/anie.200703934
3. Mastalerz, M. *Chem. – Eur. J.* **2012,** *18,* 10082–10091. doi:10.1002/chem.201201351
4. Corma, A.; García, H.; Llabrés i Xamena, F. X. *Chem. Rev.* **2010,** *110,* 4606–4655. doi:10.1021/cr9003924
5. Catti, L.; Zhang, Q.; Tiefenbacher, K. *Chem. – Eur. J.* **2016,** *22,* 9060–9066. doi:10.1002/chem.201600726
6. Allendorf, M. D.; Bauer, C. A.; Bhakta, R. K.; Houk, R. J. T. *Chem. Soc. Rev.* **2009,** *38,* 1330–1352. doi:10.1039/b802352m
7. Chen, Y.; Ma, S. *Rev. Inorg. Chem.* **2012,** *32,* 81–100. doi:10.1515/revic-2012-0003
8. Heine, J.; Müller-Buschbaum, K. *Chem. Soc. Rev.* **2013,** *42,* 9232–9242. doi:10.1039/c3cs60232j
9. Meyer, L. V.; Schönfeld, F.; Müller-Buschbaum, K. *Chem. Commun.* **2014,** *50,* 8093–8108. doi:10.1039/c4cc00848k
10. Liu, D.; Lu, K.; Poon, C.; Lin, W. *Inorg. Chem.* **2014,** *53,* 1916–1924. doi:10.1021/ic402194c
11. Hu, Z.; Deibert, B. J.; Li, J. *Chem. Soc. Rev.* **2014,** *43,* 5815–5840. doi:10.1039/c4cs00010b
12. Roy, S.; Chakraborty, A.; Maji, T. K. *Coord. Chem. Rev.* **2014,** *273–274,* 139–164. doi:10.1016/j.ccr.2014.03.035
13. Müller-Buschbaum, K.; Beuerle, F.; Feldmann, C. *Microporous Mesoporous Mater.* **2015,** *216,* 171–199. doi:10.1016/j.micromeso.2015.03.036
14. Wang, C.; Zhang, T.; Lin, W. *Chem. Rev.* **2012,** *112,* 1084–1104. doi:10.1021/cr200252n
15. Rybak, J.-C.; Hailmann, M.; Matthes, P. R.; Zurawski, A.; Nitsch, J.; Steffen, A.; Heck, J. G.; Feldmann, C.; Götzendörfer, S.; Meinhardt, J.; Sextl, G.; Kohlmann, H.; Sedlmaier, S. J.; Schnick, W.; Müller-Buschbaum, K. *J. Am. Chem. Soc.* **2013,** *135,* 6896–6902. doi:10.1021/ja3121718
16. Dogru, M.; Bein, T. *Chem. Commun.* **2014,** *50,* 5531–5546. doi:10.1039/c3cc46767h
17. Kitagawa, S.; Kitaura, R.; Noro, S. *Angew. Chem., Int. Ed.* **2004,** *43,* 2334–2375. doi:10.1002/anie.200300610
18. Férey, G. *Chem. Soc. Rev.* **2008,** *37,* 191–214. doi:10.1039/b618320b
19. Feng, X.; Ding, X.; Jiang, D. *Chem. Soc. Rev.* **2012,** *41,* 6010–6022. doi:10.1039/c2cs35157a
20. Ding, S.-Y.; Wang, W. *Chem. Soc. Rev.* **2013,** *42,* 548–568. doi:10.1039/c2cs35072f
21. Zhang, G.; Mastalerz, M. *Chem. Soc. Rev.* **2014,** *43,* 1934–1947. doi:10.1039/c3cs60358j
22. Hasell, T.; Cooper, A. I. *Nat. Rev. Mater.* **2016,** *1,* No. 16053. doi:10.1038/natrevmats.2016.53
23. Mastalerz, M.; Schneider, M. W.; Oppel, I. M.; Presly, O. *Angew. Chem., Int. Ed.* **2011,** *50,* 1046–1051. doi:10.1002/anie.201005301

24. Schneider, M. W.; Oppel, I. M.; Ott, H.; Lechner, L. G.; Hauswald, H.-J.; Stoll, R.; Mastalerz, M. *Chem. – Eur. J.* **2012,** *18,* 836–847. doi:10.1002/chem.201102857
25. Brutschy, M.; Schneider, M. W.; Mastalerz, M.; Waldvogel, S. R. *Adv. Mater.* **2012,** *24,* 6049–6052. doi:10.1002/adma.201202786
26. Schneider, M. W.; Oppel, I. M.; Griffin, A.; Mastalerz, M. *Angew. Chem., Int. Ed.* **2013,** *52,* 3611–3615. doi:10.1002/anie.201208156
27. Zhang, G.; Presly, O.; White, F.; Oppel, I. M.; Mastalerz, M. *Angew. Chem., Int. Ed.* **2014,** *53,* 1516–1520. doi:10.1002/anie.201308924
28. Elbert, S. M.; Rominger, F.; Mastalerz, M. *Chem. – Eur. J.* **2014,** *20,* 16707–16720. doi:10.1002/chem.201404829
29. Lim, S.; Kim, H.; Selvapalam, N.; Kim, K.-J.; Cho, S. J.; Seo, G.; Kim, K. *Angew. Chem., Int. Ed.* **2008,** *47,* 3352–3355. doi:10.1002/anie.200800772
30. Comotti, A.; Bracco, S.; Distefano, G.; Sozzani, P. *Chem. Commun.* **2009,** 284–286. doi:10.1039/b820200a
31. Yang, W.; Greenaway, A.; Lin, X.; Matsuda, R.; Blake, A. J.; Wilson, C.; Lewis, W.; Hubberstey, P.; Kitagawa, S.; Champness, N. R.; Schröder, M. *J. Am. Chem. Soc.* **2010,** *132,* 14457–14469. doi:10.1021/ja1042935
32. He, Y.; Xiang, S.; Chen, B. *J. Am. Chem. Soc.* **2011,** *133,* 14570–14573. doi:10.1021/ja2066016
33. Dalapati, S.; Saha, R.; Jana, S.; Patra, A. K.; Bhaumik, A.; Kumar, S.; Guchhait, N. *Angew. Chem., Int. Ed.* **2012,** *51,* 12534–12537. doi:10.1002/anie.201205439
34. Mastalerz, M.; Oppel, I. M. *Angew. Chem.* **2012,** *124,* 5345–5348. doi:10.1002/ange.201201174
35. Luo, X.-Z.; Jia, X.-J.; Deng, J.-H.; Zhong, J.-L.; Liu, H.-J.; Wang, K.-J.; Zhong, D.-C. *J. Am. Chem. Soc.* **2013,** *135,* 11684–11687. doi:10.1021/ja403002m
36. Natarajan, R.; Bridgland, L.; Sirikulkajorn, A.; Lee, J.-H.; Haddow, M. F.; Magro, G.; Ali, B.; Narayanan, S.; Strickland, P.; Charmant, J. P. H.; Orpen, A. G.; McKeown, N. B.; Bezzu, C. G.; Davis, A. P. *J. Am. Chem. Soc.* **2013,** *135,* 16912–16925. doi:10.1021/ja405701u
37. Chen, T.-H.; Popov, I.; Kaveevivitchai, W.; Chuang, Y.-C.; Chen, Y.-S.; Daugulis, O.; Jacobson, A. J.; Miljanić, O. S. *Nat. Commun.* **2014,** *5,* No. 5131. doi:10.1038/ncomms6131
38. Li, P.; He, Y.; Arman, H. D.; Krishna, R.; Wang, H.; Weng, L.; Chen, B. *Chem. Commun.* **2014,** *50,* 13081–13084. doi:10.1039/c4cc05506c
39. Li, P.; He, Y.; Guang, J.; Weng, L.; Zhao, J. C.-G.; Xiang, S.; Chen, B. *J. Am. Chem. Soc.* **2014,** *136,* 547–549. doi:10.1021/ja4129795
40. Lü, J.; Perez-Krap, C.; Suyetin, M.; Alsmail, N. H.; Yan, Y.; Yang, S.; Lewis, W.; Bichoutskaia, E.; Tang, C. C.; Blake, A. J.; Cao, R.; Schröder, M. *J. Am. Chem. Soc.* **2014,** *136,* 12828–12831. doi:10.1021/ja506577g
41. Hisaki, I.; Nakagawa, S.; Tohnai, N.; Miyata, M. *Angew. Chem., Int. Ed.* **2015,** *54,* 3008–3012. doi:10.1002/anie.201411438
42. Li, P.; He, Y.; Zhao, Y.; Weng, L.; Wang, H.; Krishna, R.; Wu, H.; Zhou, W.; O'Keeffe, M.; Han, Y.; Chen, B. *Angew. Chem., Int. Ed.* **2015,** *54,* 574–577. doi:10.1002/anie.201410077
43. Wang, H.; Li, B.; Wu, H.; Hu, T.-L.; Yao, Z.; Zhou, W.; Xiang, S.; Chen, B. *J. Am. Chem. Soc.* **2015,** *137,* 9963–9970. doi:10.1021/jacs.5b05644
44. Patil, R. S.; Banerjee, D.; Zhang, C.; Thallapally, P. K.; Atwood, J. L. *Angew. Chem., Int. Ed.* **2016,** *55,* 4523–4526. doi:10.1002/anie.201600658
45. Zhou, D.-D.; Xu, Y.-T.; Lin, R.-B.; Mo, Z.-W.; Zhang, W.-X.; Zhang, J.-P. *Chem. Commun.* **2016,** *52,* 4991–4994. doi:10.1039/c6cc00366d
46. Kohl, B.; Rominger, F.; Mastalerz, M. *Org. Lett.* **2014,** *16,* 704–707. doi:10.1021/ol403383y
47. Yan, W.; Seifermann, S. M.; Pierrat, P.; Bräse, S. *Org. Biomol. Chem.* **2015,** *13,* 25–54. doi:10.1039/c4ob01663g
48. Beuerle, F.; Hirsch, A. *Chem. – Eur. J.* **2009,** *15,* 7447–7455. doi:10.1002/chem.200900330
49. Nierengarten, J.-F.; Iehl, J.; Oerthel, V.; Holler, M.; Illescas, B. M.; Muñoz, A.; Martín, N.; Rojo, J.; Sánchez-Navarro, M.; Cecioni, S.; Vidal, S.; Buffet, K.; Durka, M.; Vincent, S. P. *Chem. Commun.* **2010,** *46,* 3860–3862. doi:10.1039/c0cc00034e
50. Dey, S. K.; Beuerle, F.; Olson, M. A.; Stoddart, J. F. *Chem. Commun.* **2011,** *47,* 1425–1427. doi:10.1039/c0cc03963b
51. Hörmann, F.; Hirsch, A. *Chem. – Eur. J.* **2013,** *19,* 3188–3197. doi:10.1002/chem.201203881
52. Luczkowiak, J.; Muñoz, A.; Sánchez-Navarro, M.; Ribeiro-Viana, R.; Ginieis, A.; Illescas, B. M.; Martín, N.; Delgado, R.; Rojo, J. *Biomacromolecules* **2013,** *14,* 431–437. doi:10.1021/bm3016658
53. Muñoz, A.; Sigwalt, D.; Illescas, B. M.; Luczkowiak, J.; Rodríguez-Pérez, L.; Nierengarten, I.; Holler, M.; Remy, J.-S.; Buffet, K.; Vincent, S. P.; Rojo, J.; Delgado, R.; Nierengarten, J.-F.; Martín, N. *Nat. Chem.* **2016,** *8,* 50–57. doi:10.1038/nchem.2387
54. Peng, P.; Li, F.-F.; Neti, V. S. P. K.; Metta-Magana, A. J.; Echegoyen, L. *Angew. Chem., Int. Ed.* **2014,** *53,* 160–163. doi:10.1002/anie.201306761
55. Kraft, A.; Roth, P.; Schmidt, D.; Stangl, J.; Müller-Buschbaum, K.; Beuerle, F. *Chem. – Eur. J.* **2016,** *22,* 5982–5987. doi:10.1002/chem.201505137
56. Kraft, A.; Beuerle, F. *Tetrahedron Lett.* **2016,** *57,* 4651–4663. doi:10.1016/j.tetlet.2016.08.082
57. Kraft, A.; Gsänger, M.; Beuerle, F. *Eur. J. Org. Chem.* **2014,** 523–528. doi:10.1002/ejoc.201301298
58. *The PyMOL Molecular Graphics System,* Version 1.8.2.3; Schrödinger, LLC.
59. Witte, P.; Hörmann, F.; Hirsch, A. *Chem. – Eur. J.* **2009,** *15,* 7423–7433. doi:10.1002/chem.200900319
60. Supplementary crystallographic data for **HFF-2** can be obtained free of charge from The Cambridge Crystallographic Data Centre via http://www.ccdc.cam.ac.uk/data_request/cif (CCDC 1498265); crystal data: $C_{114}H_{60}O_{48}{\cdot}4C_4H_{10}O$, M = 2494.09 g mol^{-1}, triclinic, $P\bar{1}$, a = 13.1513(5), b = 14.4631(7), c = 15.2117(7) Å, α = 107.332(3), β = 95.752(3)°, γ = 94.594(2)°, V = 2729.6(2) Å3, Z = 1, ρ_{calc} = 1.517 g cm^{-3}, μ(Cu K_α) = 1.010 mm^{-1}, T = 100(2) K; 42237 independent measured reflections. $F2$ refinement, R_1 = 0.0490, wR_2 = 0.1302 (observed), 11068 independent observed reflections (R_{int} = 0.0346) [$|F_0| > 4\sigma(|F_0|)$, 2Θ ≤ 149.4°], 830 parameters, no restraints.
61. Supplementary crystallographic data for **HFF-3** can be obtained free of charge from The Cambridge Crystallographic Data Centre via http://www.ccdc.cam.ac.uk/data_request/cif (CCDC 1498266); crystal data: $C_{126}H_{84}O_{48}{\cdot}6C_4H_{10}O$, M = 2810.64 g mol^{-1}, trigonal, $R\bar{3}$, a = 33.8114(9), b = 33.8114(9), c = 9.8056(3) Å, α = 90, β = 90, γ = 120°, V = 9708.0(6) Å3, Z = 3, ρ_{calc} = 1.442 g cm^{-3}, μ(Cu K_α) = 0.927 mm^{-1}, T = 100(2) K; 44836 independent measured reflections. $F2$ refinement, R_1 = 0.0488, wR_2 = 0.1414 (observed), 4438 independent observed reflections (R_{int} = 0.0442) [$|F_0| > 4\sigma(|F_0|)$, 2Θ ≤ 150.28°], 350 parameters, no restraints.

BEILSTEIN JOURNAL OF ORGANIC CHEMISTRY

Synthesis of structurally diverse 3,4-dihydropyrimidin-2(1*H*)-ones via sequential Biginelli and Passerini reactions

Andreas C. Boukis, Baptiste Monney and Michael A. R. Meier*

Full Research Paper

Open Access

Address:
Karlsruhe Institute of Technology (KIT), Institute of Organic Chemistry, Materialwissenschaftliches Zentrum MZE, Building 30.48, Straße am Forum 7, 76131 Karlsruhe, Germany

Email:
Michael A. R. Meier* - m.a.r.meier@kit.edu

* Corresponding author

Keywords:
Biginelli reaction; molecular diversity; multicomponent reactions; Passerini reaction; tandem reactions

Beilstein J. Org. Chem. **2017,** *13,* 54–62.
doi:10.3762/bjoc.13.7

Received: 29 July 2016
Accepted: 21 December 2016
Published: 09 January 2017

This article is part of the Thematic Series "Organic porous materials".

Guest Editor: S. Bräse

Abstract

The Biginelli reaction was combined with the Passerini reaction for the first time in a sequential multicomponent tandem reaction approach. After evaluation of all possible linker components and a suitable solvent system, highly functionalized dihydropyrimidone–α-acyloxycarboxamide compounds were obtained in good to excellent yields. In a first reaction step, different 3,4-dihydropyrimidin-2(1*H*)-one acids were synthesized, isolated and fully characterized. These products were subsequently used in a Passerini reaction utilizing a dichloromethane/dimethyl sulfoxide solvent mixture. By variation of the components in both multicomponent reactions, a large number of structurally diverse compounds could be synthesized. In addition, a one-pot Biginelli–Passerini tandem reaction was demonstrated. All products were carefully characterized via 1D and 2D NMR as well as IR and HRMS.

Introduction

Multicomponent reactions (MCRs) are fascinating straightforward reactions for the preparation of diversely substituted products starting from three or more precursor molecules, forming products containing atoms/moieties of all precursor components. MCRs are often one-pot reactions with high-atom economy, convergence and efficiency. Generally, one-pot procedures have many advantages compared to multiple-step syntheses [1-3]. One-pot MCRs can shorten reaction times, provide high yields, reduce work-up steps and waste as well as energy consumption and hence lead to more effective and sustainable processes [4-6]. MCRs found numerous applications, i.e., in combinatorial chemistry, target oriented synthesis or polymer science [6-8]. The most important MCRs are the Strecker amino acid synthesis (1850), the Hantzsch dihydropyridine synthesis (1882), the Biginelli dihydropyrimidone synthesis (1891), the Mannich reaction (1912), the Passerini three-component reaction (1921) and the Ugi four-component reaction (1959) [9]. In this work, we used Biginelli and Passerini reactions to synthesize highly functionalized compounds, hence both reactions will be described in detail.

The Biginelli reaction

The Biginelli reaction is a three-component reaction between an aldehyde (in many cases aromatic aldehydes give much better results than aliphatic ones), a β-keto ester (α-acidic compound) and urea or thiourea (some mono *N*-substituted ureas can also be employed). The Biginelli reaction was discovered in 1891 by the chemist Pietro Biginelli [10]. Later, Biginelli identified the reaction product as a 3,4-dihydropyrimidin-2(1*H*)-one (DHMP) [11]. DHMPs are of great interest due to their pharmaceutic activities (i.e., calcium channel modulation, α_{1a} adrenoceptor-selective antagonists, cancer therapy, anti-HIV alkaloids) [12-15]. The mechanism of the Biginelli cyclocondensation was proposed and investigated by Kappe and is illustrated in Scheme 1a [16]. According to the generally accepted mechanism of the Biginelli reaction, aldehyde **1** is activated by a Lewis- or a Brønsted acid. In the next step, urea/thiourea **2** can serve as a nucleophile and react with the activated carbonyl carbon to form a heminal species. However, under acidic conditions heminals can eliminate water and form an *N*-acyliminium cation **3**. This reactive cation **3** can then react with the nucleophilic α-carbon atom of β-ketoester **4** to an open chain ureide **5**. Subsequent ring closure results in a hexahydropyrimidine intermediate **6**. In the last step, the irreversible elimination of water forms the thermodynamically favored DHMP product **7**. This accepted mechanism was supported by spectroscopic data. However, alternative mechanisms are discussed in the literature [17,18]. In the so called enamine route, urea **2** and the β-ketoester **4** form an enamine in the first reaction step. Subsequently, the enamine reacts with the aldehyde **1** [19]. A third mechanism discussed, is the Knoevenagel type reaction be-

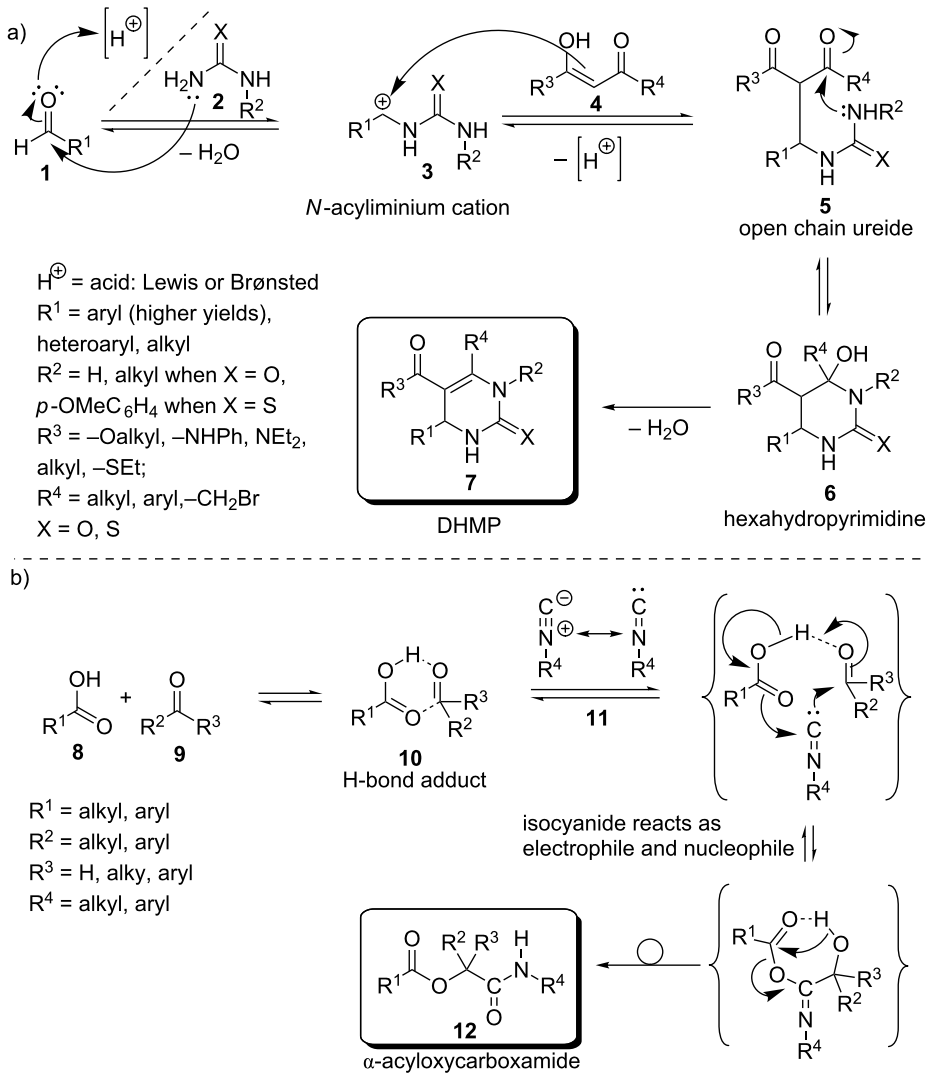

Scheme 1: a) Proposed mechanism of the Biginelli reaction according to [6]. b) Proposed mechanism of the Passerini reaction.

tween the aldehyde **1** and β-ketoester **4** followed by a subsequent reaction with urea **2** [20].

The Passerini reaction

The Passerini reaction was discovered in 1921 by Mario Passerini and is a three-component reaction between a carboxylic acid **8**, a carbonyl compound **9** and an isocyanide **11** [21]. The Passerini reaction works best in non-polar solvents like dichloromethane. The mechanism of the Passerini reaction (Scheme 1b) is proposed to proceed via the formation of a hydrogen bond (H-bond) adduct between carboxylic acid **8** and carbonyl component **9**, resulting in a six-membered cyclic H-bond adduct **10**. Subsequently, isocyanide **11** reacts with **10**, thereby showing a simultaneous nucleophilic and electrophilic reactivity (α-addition). The herein formed seven-membered intermediate has not been isolated, because it immediately undergoes a rearrangement, affording the Passerini α-acyloxycarboxamide adduct **12** [18].

Tandem reactions

Tandem reactions (also known as cascade [22] or domino reactions [23]) are chemical transformations that involve at least two independent reactions utilizing different functional groups with distinct chemical reactivities [24-27]. So far, only a few examples of multicomponent tandem reactions are described in the literature [28,29]. Portlock et al. reported on Petasis–Ugi tandem reactions leading to a product with six different side chains [30,31]. Al-Tel et al. combined the Groebke–Blackburn reaction with either Passerini or Ugi reactions in a sequential one-pot procedure [32]. Furthermore, up to eight components were reacted by the combination of three multicomponent reactions [33]. In 2010, the Ugi reaction and the Ugi–Smiles reaction were combined by Westermann et al. [34]. In addition, the Ugi reaction was used in combination with the Biginelli reaction by Brodsky et al. [35]. In this work, five Biginelli acids were synthesized in 33–83% yields and utilized in a Ugi reaction for the synthesis of six DHMP amides with 21–63% yields. In a similar reaction strategy, Wipf et al. synthesized a library of twelve Biginelli compounds and reacted them with the respective Ugi components under reflux in methanol to yield 30 different DHMP amides in 5–51% yield [36]. Furthermore, the Biginelli reaction has been used in a polymerization process combined with the Hantzsch reaction to from copolycondensates [37]. It is noteworthy that in the literature the term tandem is not always used consistently with the initial definition by Tieze et al. [23].

In this work, the Biginelli reaction was combined in a sequential approach with the Passerini reaction for the first time. Furthermore, both reactions were combined in a one-pot tandem procedure. A general overview of our investigations is illustrated in Supporting Information File 1, Scheme S1. All synthesized substances are displayed in Supporting Information File 1, Figure S1.

Results and Discussion

For the Biginelli–Passerini sequential reaction, the Biginelli reaction was performed first, in order to avoid undesired transesterification reactions (of the Passerini product) due to the acidic conditions of the Biginelli reaction [33]. A general challenge, which has to be faced in this context, is the choice of solvent and the selection of bifunctional components (which can interlink both the Biginelli and the Passerini reaction). In the earlier reported Biginelli–Ugi tandem reaction of Wipf et al. [36], methanol was used as solvent. As mentioned previously, the solvent of choice for the Passerini reaction is dichloromethane, providing the highest yields. The DHMP Biginelli products, however, are in most cases very poorly soluble in non-polar solvents. In our investigations, a solvent mixture of dichloromethane with a small amount of dimethyl sulfoxide (polar but aprotic) allowed the successful combination of both chemistries. All possible bifunctional components for the Biginelli–Passerini reaction are represented in Figure 1. Compared to the above mentioned multicomponent tandem approaches, our strategy provides higher yields and makes use of more bifunctional linker components.

Careful evaluation of the bifunctional components allowed a pre-selection: **A3**, **B3** and **C3** in Figure 1 carry an isocyanide functionality, which could hydrolyze under the acidic conditions for the Biginelli reaction [38]. Components **A2**, **B2** and **C2** carry an aldehyde functional group for the Passerini reaction, but this could react on both sides in the Biginelli reaction. Therefore, **A2**, **B2**, **C2** as well as **A3**, **B3**, **C3** were excluded from our investigations. The remaining components **A1**, **B1** and **C1** seemed most promising for our purposes. Hence, we focused on commercially available components with **A1**, **B1** and **C1** like structures, i.e., **C1**: 4-formylbenzoic acid; **B1**: *N*-carbamoylglycine, **A1**: benzyl acetoacetate for the Biginelli reaction and subsequent hydrogenolytic deprotection to the corresponding acid.

The Biginelli reactions were performed in dimethyl sulfoxide at 110 °C in order to remove the water formed in course of the reaction. After a simple washing procedure, the desired DHMP acids **13**–**18** were obtained in 63–93% yield (Table 1). Alternative syntheses for DHMP acids (**13**–**15** and **17**) were described in literature and can be found in Supporting Information File 1. However, our Biginelli approach is simple, utilizes *p*-TSA as a cheap catalyst, provides high yields and can be used for the preparation of various DHMP acids with different bifunctional linkers. Aliphatic aldehydes did not react well under these

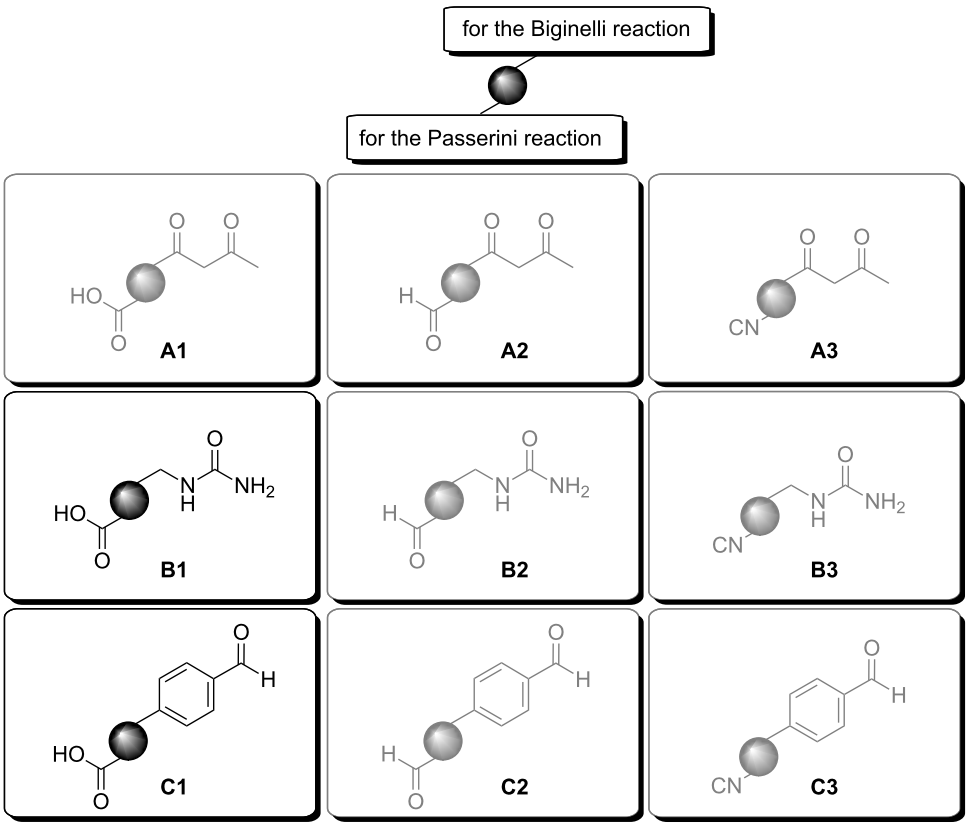

Figure 1: Bifunctional components for the Biginelli–Passerini tandem reaction.

Table 1: Biginelli reactions for the preparation of DHMP acids.[a]

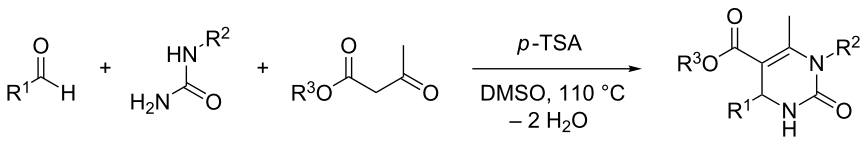

1 4 13–18

Entry	R^1	R^2	R^3	Yield [%]	Product
1	Ph	H	Bn	91	**13**
2[b]	Ph	H	H	93	**14**
3	Ph	CH_2CO_2H	Et	63	**15**
4	Ph	CH_2CO_2H	Bn	78	**16**
5	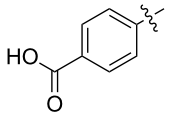	H	Et	90	**17**
6	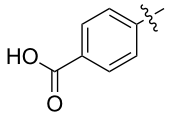	H	Bn	91	**18**

[a]Conditions: 0.10 equiv *p*-TSA, 110 °C 8–48 h in DMSO. [b]Obtained via hydrogenolytic deprotection of product **13** (entry 1). Conditions: H_2 (balloon), 10 wt % Pd/C, acetic acid/ethanol (1:3), 50 °C, 15 h.

conditions (even after longer reaction periods of up to six days) and product isolation was not straightforward.

For the subsequent Passerini reactions, the DHMP acids were dissolved in a mixture of dichloromethane and dimethyl sulfoxide (4:1 → 2:1). After the subsequent addition of the aldehyde and isocyanide components, three days reaction time at room temperature and subsequent purification via column chromatography, the Biginelli–Passerini products **19**–**25** were obtained in 22–99% yield (Table 2).

The lower yield for **25** (39%) might be due to the tertiary amine structure of the morpholinoethyl side chain, requiring a more complex purification. The reaction mixture for the Passerini reaction of DHMP **18** was not completely homogeneous, which might be responsible for the lower yield of **20** (22%). For the other reactions investigated in this work, our Passerini protocol proved to be robust and very effective providing very good to quantitative yields (up to 99% for **23**). In Figure 2, a representative ^{1}H NMR comparison between the DHMP acid **17** and the Passerini product **19** is illustrated. The CO_2H proton at 12.9 ppm disappeared after the Passerini reaction, while all other DHMP signals, i.e., the N*H*C at 9.2 ppm, the C*H*NH at 5.2 ppm or the CCH_3 at 2.3 ppm, did not shift. Furthermore, the new characteristic signals for the CC*H*O at 4.9 ppm, the C(CH_3)$_3$ at 1.2 ppm and the terminal CH_2CH_3 methyl group at 0.84 ppm strongly indicate the formation of the respective Biginelli–Passerini product.

Table 2: Passerini reaction on DHMP acids.[a]

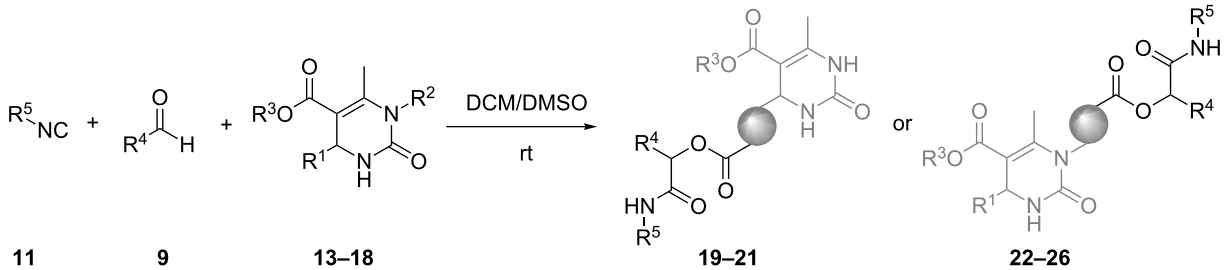

11 **9** **13–18** **19–21** **22–26**

Entry	DHMP acid	R^1	R^2	R^3	R^4	R^5	Yield [%]	Product
1	**17**	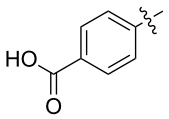	H	Et	C_6H_{13}	*t*-Bu	67	**19**
2	**18**	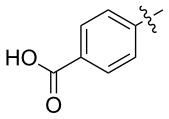	H	Bn	C_6H_{13}	*t*-Bu	22	**20**
3	**17**	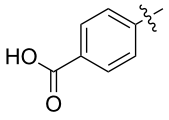	H	Et	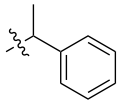	cyclohexyl	98	**21**
4	**15**	Ph	CH_2COOH	Et	iPr	*t*-Bu	76	**22**
5	**15**	Ph	CH_2COOH	Et	$C_{10}H_{19}$	*t*-Bu	99	**23**
6	**15**	Ph	CH_2COOH	Et	C_7H_{15}	Bn	76	**24**
7	**15**	Ph	CH_2COOH	Et	C_7H_{15}	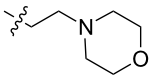	39	**25**
8	**15**	Ph	CH_2COOH	Et		C_5H_{11}	79	**26**
9[b]	–	*p*-$C_6H_4F_c$	CH_2COOH	Et	*p*-$C_6H_4F_c$	C_5H_{11}	41	**27**

[a]Conditions: Room temperature, 3 d in DCM. [b]One pot procedure: Biginelli acid was not isolated.

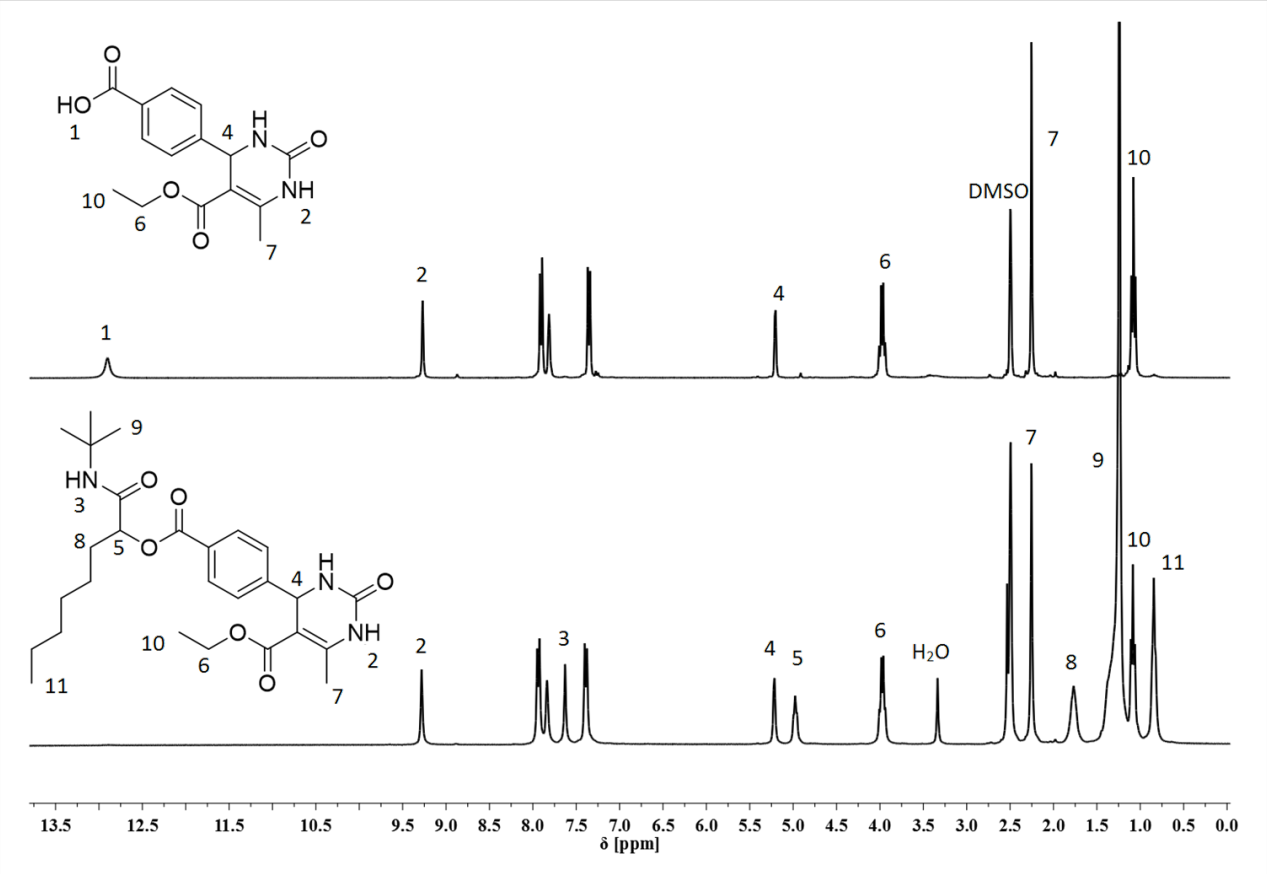

Figure 2: Stacked ^{1}H NMR spectra and signal assignment. Top: DHMP acid **17**; bottom: Biginelli–Passerini tandem product **19**.

As a proof of principle, the Biginelli and Passerini reaction were combined in a one-pot synthesis. In this experiment, the Biginelli reaction was performed with an excess of the aldehyde component (three equivalents) in a minimal amount of dimethyl sulfoxide. After completion of the Biginelli reaction, the crude reaction mixture was cooled to room temperature and diluted with dichloromethane. Subsequently, an isocyanide was added to the mixture enabling the Passerini reaction with the exceeding aldehyde. The resulting one-pot product **27** was obtained in 41% yield after column chromatography (Table 2, entry 9). However, the structural diversity in this approach is limited if compared to the previously described two-step approach (isolation of Biginelli acid) because the same aldehyde component is participating in both MCRs.

Interestingly, the ^{1}H and ^{13}C NMR spectra of the chromatographically pure Biginelli–Passerini products displayed a signal splitting for distinct signals (Figure 3).

A more detailed analysis revealed that most of the split signals were located either next to chiral centres in the molecule or in the six-membered DHMP core. In order to identify the cause of this peak splitting, high temperature NMR experiments at 40 °C, 60 °C and 80 °C were conducted. Even at higher temperatures the peak splitting remained, evidencing that the splitting was not caused by rotational barriers or conformational effects. Furthermore, the splitting was not observed in the DHMP acids **13**–**18** (after the Biginelli reaction, which was performed first). In principle, the Biginelli and Passerini reactions both form a new chiral centre, which was not controlled in our investigations, leading to a racemic mixture (*R* and *S*). After the Passerini reactions, four different stereoisomers (*RR*, *RS*, *SR*, *SS*) are thus obtained. The homo (*RR*, *SS*) and hetero pairs (*RS*, *SR*) are diastereomers with slightly different physical properties. In the context of our experimental NMR data, it is thus fair to assume that the peak splitting is caused by these diastereomers (Figure 4).

Conclusion

The Biginelli reaction was successfully combined with the Passerini reaction to obtain highly functionalized DHMP heterocyclic products. For this purpose, different DHMP acids were prepared by variation of the components and the bifunctional linker. The DHMP acids were then reacted in a Passerini reaction employing a dichloromethane/dimethyl sulfoxide solvent mixture. The respective Biginelli–Passerini reaction prod-

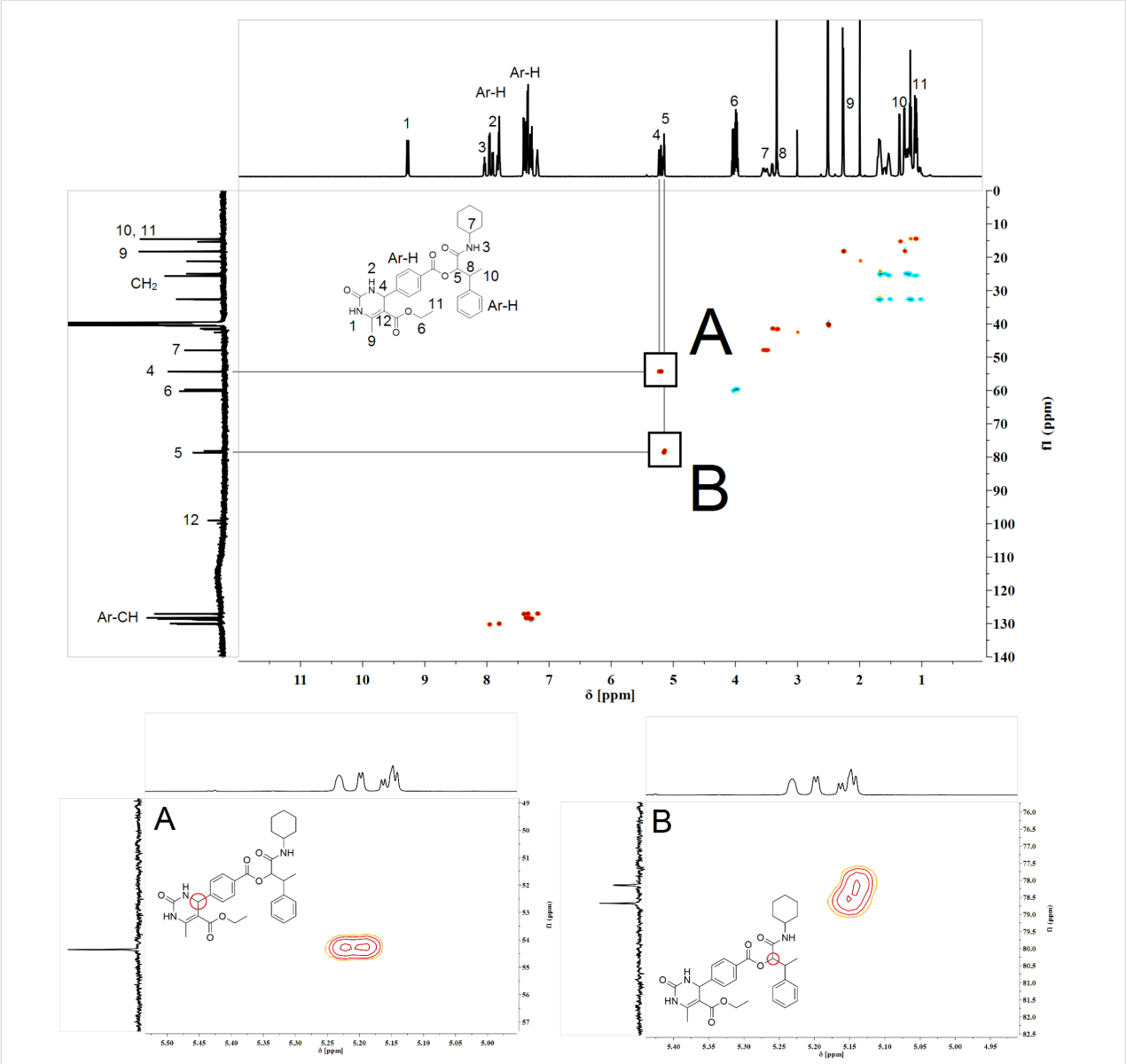

Figure 3: Representative HSQC spectrum of the pure Biginelli–Passerini tandem product **21**, expansions and signal assignment for two asymmetric carbon atoms. A: Diastereomeric signal splitting in ^{1}H NMR solely. B: Diastereomeric splitting in both ^{1}H and ^{13}C NMR, two different species can be identified.

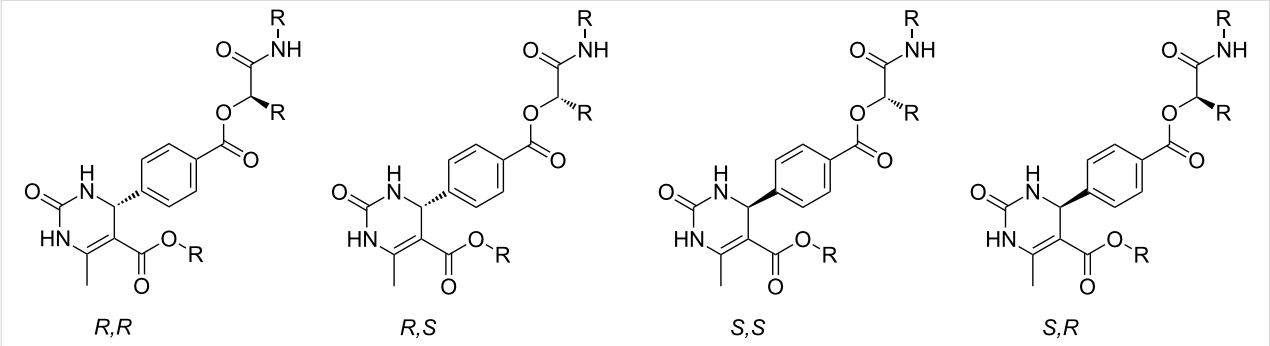

Figure 4: Stereoisomers formed in the Biginelli–Passerini tandem reaction. The homo (*RR*, *SS*) and hetero pairs (*RS*, *SR*) are diastereomers.

ucts were in most cases obtained in good to excellent yields. Furthermore, a one-pot Biginelli–Passerini reaction without intermediate work-up was demonstrated. All compounds of this investigation were carefully characterized via NMR (1D and 2D), IR and HRMS. The herein presented strategy is currently under investigation for the preparation of sequence-defined macromolecules [39,40]. Furthermore, the obtained compounds present a rigid, geometrically fixed and highly functionalized DHMP moiety, which could potentially be utilized for covalent organic frameworks and porous materials [41,42].

Supporting Information

Supporting Information File 1

Experimental section and NMR spectra of all synthesized compounds.
[http://www.beilstein-journals.org/bjoc/content/supplementary/1860-5397-13-7-S1.pdf]

Acknowledgements

A.B. is grateful for a scholarship from the Fonds der Chemischen Industrie. We would like to thank SFB1176 (project A3) for financial support and our colleague Prof. Podlech from the Institute of Organic Chemistry at KIT for kindly sharing lab space with us.

References

1. Touré, B. B.; Hall, D. G. *Chem. Rev.* **2009,** *109,* 4439–4486. doi:10.1021/cr800296p
2. D'Souza, D. M.; Müller, T. J. J. *Chem. Soc. Rev.* **2007,** *36,* 1095–1108. doi:10.1039/B608235C
3. Dömling, A.; Ugi, I. *Angew. Chem., Int. Ed.* **2000,** *39,* 3168–3210. doi:10.1002/1521-3773(20000915)39:18<3168::AID-ANIE3168>3.0.CO;2-U
4. Gu, Y. *Green Chem.* **2012,** *14,* 2091–2128. doi:10.1039/c2gc35635j
5. Ganem, B. *Acc. Chem. Res.* **2009,** *42,* 463–472. doi:10.1021/ar800214s
6. Boukis, A. C.; Llevot, A.; Meier, M. A. R. *Macromol. Rapid Commun.* **2016,** *37,* 643–649. doi:10.1002/marc.201500717
7. Xue, H.; Zhao, Y.; Wu, H.; Wang, Z.; Yang, B.; Wei, Y.; Wang, Z.; Tao, L. *J. Am. Chem. Soc.* **2016,** *138,* 8690–8693. doi:10.1021/jacs.6b04425
8. Hu, R.; Li, W.; Tang, B. Z. *Macromol. Chem. Phys.* **2016,** *217,* 213–224. doi:10.1002/macp.201500291
9. Zhu, J.; Bienaymé, H. *Multicomponent reactions;* John Wiley & Sons: Hoboken, New Jersey, 2006.
10. Biginelli, P. *Ber. Dtsch. Chem. Ges.* **1891,** *24,* 1317–1319. doi:10.1002/cber.189102401228
11. Tron, G. C.; Minassi, A.; Appendino, G. *Eur. J. Org. Chem.* **2011,** 5541–5550. doi:10.1002/ejoc.201100661
12. Kappe, C. O. *Eur. J. Med. Chem.* **2000,** *35,* 1043–1052. doi:10.1016/S0223-5234(00)01189-2
13. Ajani, O. O.; Isaac, J. T.; Owoeye, T. F.; Akinsiku, A. A. *Int. J. Biol. Chem.* **2015,** *9,* 148–177. doi:10.3923/ijbc.2015.148.177
14. Selvam, T. P.; James, C. R.; Dniandev, P. V.; Valzita, S. K. *Res. Pharm.* **2012,** *2* (4), 1–9.
15. Sepehri, S.; Sanchez, H. P.; Fassihi, A. *J. Pharm. Pharm. Sci.* **2015,** *18,* 1–52. doi:10.18433/J3Q01V
16. Kappe, C. O. *J. Org. Chem.* **1997,** *62,* 7201–7204. doi:10.1021/jo971010u
17. Puripat, M.; Ramozzi, R.; Hatanaka, M.; Parasuk, W.; Parasuk, V.; Morokuma, K. *J. Org. Chem.* **2015,** *80,* 6959–6967. doi:10.1021/acs.joc.5b00407
18. Alvim, H. G. O.; da Silva Júnior, E. N.; Neto, B. A. D. *RSC Adv.* **2014,** *4,* 54282–54299. doi:10.1039/C4RA10651B
19. Folkers, K.; Johnson, T. B. *J. Am. Chem. Soc.* **1933,** *55,* 3784–3791. doi:10.1021/ja01336a054
20. Sweet, F.; Fissekis, J. D. *J. Am. Chem. Soc.* **1973,** *95,* 8741–8749. doi:10.1021/ja00807a040
21. Passerini, M.; Simone, L. *Gazz. Chim. Ital.* **1921,** *51,* 126–129.
22. Nicolaou, K. C.; Edmonds, D. J.; Bulger, P. G. *Angew. Chem., Int. Ed.* **2006,** *45,* 7134–7186. doi:10.1002/anie.200601872
23. Tietze, L. F. *Chem. Rev.* **1996,** *96,* 115–136. doi:10.1021/cr950027e
24. Parsons, P. J.; Penkett, C. S.; Shell, A. J. *Chem. Rev.* **1996,** *96,* 195–206. doi:10.1021/cr950023+
25. Behr, A.; Vorholt, A. J.; Ostrowski, K. A.; Seidensticker, T. *Green Chem.* **2014,** *16,* 982–1006. doi:10.1039/C3GC41960F
26. Zhou, J. *Chem. – Asian J.* **2010,** *5,* 422–434. doi:10.1002/asia.200900458
27. Batey, R. A. *J. Am. Chem. Soc.* **2007,** *129,* 7476. doi:10.1021/ja069820n
28. Brauch, S.; van Berkel, S. S.; Westermann, B. *Chem. Soc. Rev.* **2013,** *42,* 4948–4962. doi:10.1039/c3cs35505e
29. Cioc, R. C.; Ruijter, E.; Orru, R. V. A. *Green Chem.* **2014,** *16,* 2958–2975. doi:10.1039/c4gc00013g
30. Portlock, D. E.; Ostaszewski, R.; Naskar, D.; West, L. *Tetrahedron Lett.* **2003,** *44,* 603–605. doi:10.1016/S0040-4039(02)02619-9
31. Portlock, D. E.; Naskar, D.; West, L.; Ostaszewski, R.; Chen, J. J. *Tetrahedron Lett.* **2003,** *44,* 5121–5124. doi:10.1016/S0040-4039(03)01119-5
32. Al-Tel, T. H.; Al-Qawasmeh, R. A.; Voelter, W. *Eur. J. Org. Chem.* **2010,** 5586–5593. doi:10.1002/ejoc.201000808
33. Elders, N.; van der Born, D.; Hendrickx, L. J. D.; Timmer, B. J. J.; Krause, A.; Janssen, E.; de Kanter, F. J. J.; Ruijter, E.; Orru, R. V. A. *Angew. Chem., Int. Ed.* **2009,** *48,* 5856–5859. doi:10.1002/anie.200902683
34. Brauch, S.; Gabriel, L.; Westermann, B. *Chem. Commun.* **2010,** *46,* 3387–3389. doi:10.1039/b927388c
35. Fewell, S. W.; Smith, C. M.; Lyon, M. A.; Dumitrescu, T. P.; Wipf, P.; Day, B. W.; Brodsky, J. L. *J. Biol. Chem.* **2004,** *279,* 51131–51140. doi:10.1074/jbc.M404857200
36. Werner, S.; Turner, D. M.; Lyon, M. A.; Huryn, D. M.; Wipf, P. *Synlett* **2006,** 2334–2338. doi:10.1055/s-2006-949648
37. Wu, H.; Fu, C.; Zhao, Y.; Yang, B.; Wei, Y.; Wang, Z.; Tao, L. *ACS Macro Lett.* **2015,** *4,* 1189–1193. doi:10.1021/acsmacrolett.5b00637
38. Sung, K.; Chen, C.-C. *Tetrahedron Lett.* **2001,** *42,* 4845–4848. doi:10.1016/S0040-4039(01)00863-2
39. Solleder, S. C.; Zengel, D.; Wetzel, K. S.; Meier, M. A. R. *Angew. Chem., Int. Ed.* **2016,** *55,* 1204–1207. doi:10.1002/anie.201509398
40. Lutz, J.-F.; Lehn, J.-M.; Meijer, E. W.; Matyjaszewski, K. *Nat. Rev. Mater.* **2016,** *1,* No. 16024. doi:10.1038/natrevmats.2016.24

41. Feng, X.; Ding, X.; Jiang, D. *Chem. Soc. Rev.* **2012,** *41,* 6010–6022. doi:10.1039/c2cs35157a
42. Muller, T.; Bräse, S. *RSC Adv.* **2014,** *4,* 6886–6907. doi:10.1039/c3ra46951d

License and Terms

BEILSTEIN JOURNAL OF ORGANIC CHEMISTRY

Fast and efficient synthesis of microporous polymer nanomembranes via light-induced click reaction

Qi An[1], Youssef Hassan[1,2], Xiaotong Yan[1], Peter Krolla-Sidenstein[1], Tawheed Mohammed[1,3], Mathias Lang[4], Stefan Bräse[4,5] and Manuel Tsotsalas[*1,4]

Full Research Paper

Open Access

Address:
[1]Institute of Functional Interfaces (IFG), Karlsruhe Institute of Technology (KIT), Hermann-von-Helmholtz-Platz 1, D-76344 Eggenstein-Leopoldshafen, Germany, [2]Zewail City of Science and Technology, Center for Materials Science, Sheikh Zayed District, 6th of October City, 12588, Giza, Egypt, [3]Institute of Physics and Technology, International X-ray Optics Lab, National Research Tomsk Polytechnic University (TPU), 30 Lenin ave., Tomsk 634050, Russia, [4]Institute for Organic Chemistry (IOC), Karlsruhe Institute of Technology (KIT), Fritz-Haber-Weg 6, D-76131 Karlsruhe, Germany, and [5]Institute of Toxicology and Genetics (ITG), Karlsruhe Institute of Technology (KIT), Hermann-von-Helmholtz-Platz 1, D-76344 Eggenstein-Leopoldshafen, Germany

Email:
Manuel Tsotsalas* - manuel.tsotsalas@kit.edu

* Corresponding author

Keywords:
click chemistry; conjugated microporous polymers (CMPs); microporous materials; nanomembranes; thin films; thiol–yne coupling reaction (TYC)

Beilstein J. Org. Chem. **2017,** *13,* 558–563.
doi:10.3762/bjoc.13.54

Received: 21 November 2016
Accepted: 02 March 2017
Published: 17 March 2017

This article is part of the Thematic Series "Organic porous materials".

Associate Editor: P. J. Skabara

Abstract

Conjugated microporous polymers (CMPs) are materials of low density and high intrinsic porosity. This is due to the use of rigid building blocks consisting only of lightweight elements. These materials are usually stable up to temperatures of 400 °C and are chemically inert, since the networks are highly crosslinked via strong covalent bonds, making them ideal candidates for demanding applications in hostile environments. However, the high stability and chemical inertness pose problems in the processing of the CMP materials and their integration in functional devices. Especially the application of these materials for membrane separation has been limited due to their insoluble nature when synthesized as bulk material. To make full use of the beneficial properties of CMPs for membrane applications, their synthesis and functionalization on surfaces become increasingly important. In this respect, we recently introduced the solid liquid interfacial layer-by-layer (LbL) synthesis of CMP-nanomembranes via Cu catalyzed azide–alkyne cycloaddition (CuAAC). However, this process featured very long reaction times and limited scalability. Herein we present the synthesis of surface grown CMP thin films and nanomembranes via light induced thiol–yne click reaction. Using this reaction, we could greatly enhance the CMP nanomembrane synthesis and further broaden the variability of the LbL approach.

Introduction

The synthesis of microporous organic and inorganic materials such as zeolites [1], mesoporous silica [2] as well as metal-organic frameworks (MOF) [3,4] and covalent organic frameworks (COF) [5-7] attracted large attention because of their high potential in catalysis, gas storage and separation as well as in organic electronics [8]. Among the microporous materials, conjugated microporous polymers (CMPs) [9,10] or porous aromatic frameworks (PAF) [11] have favorable properties for many applications, since they combine a high chemical and thermal stability, which is comparable to inorganic materials, with the variability of organic compounds.

Nevertheless, their insoluble nature has so far greatly limited their processing and integration into functional devices, since CMPs and PAF are usually synthesized as highly crosslinked interconnected and insoluble powders [12]. Only few examples of soluble and therefore processable CMP materials are known, all limited to linear CMPs [13,14].

To overcome the issue of low processability, recently the group of Jiang and our group introduced the interfacial synthesis using an electro-activated approach [15] and a copper catalyzed azide–alkyne cycloaddition (CuAAC) approach, respectively [16]. These procedures are still limited to conductive substrates or associated with long reaction times.

In this work, we present a novel strategy for the LbL synthesis of CMP thin films and nanomembranes, using the light-induced and catalyst-free thiol–yne coupling (TYC) reaction.

TYC has gained large attention as a representative of the click chemistry concept [17]. In the TYC reaction, usually a photoinitiator creates thiyl radicals [18-20], which react with nearby alkyne moieties to form covalent sulfur–carbon bonds and vinyl radicals. Additional thiol moieties can undergo hydrogen transfer to the vinyl radical leading to thiyl radicals and vinyl sulfides. The vinyl sulfides can then undergo a thiol–ene coupling (TEC) reaction, leading to bis-sulfide species. TYC has been used for surface modification [21,22], biofunctionalization [23,24] and fabrication of 3D structures via direct laser writing (DLW) [25].

Results and Discussion

Synthesis of CMP thin films

We prepared the CMP nanomembranes in a LbL approach using the thiol–yne coupling (TYC) reaction. In order to perform the reaction on surfaces, we first functionalized the substrates with an alkyne terminated self-assembled monolayer, which presents initial groups for the stepwise growing of the CMPs using the TYC reaction.

In the first step, we immersed the functionalized surface in a solution of the tetra-topic thiol building block (tetrakis(4-sulfanylphenyl)methane, TPM-SH) and a small amount of photoinitiator (2-hydroxy-1-[4-(2-hydroxyethoxy)phenyl]-2-methylpropan-1-one) [26]. Afterwards we irradiated the substrate using a standard UV lamp at a wavelength of 365 nm for 3 minutes. We then rinsed the substrate thoroughly with absolute THF and immersed the substrate in a solution of the tetra-topic alkyne building block (tetrakis(4-ethynylphenyl)methane, TPM-alkyne), again with a small amount of photoinitiator. Then we irradiated the substrate for 3 minutes and rinsed the substrate thoroughly with absolute THF.

Figure 1 shows the LbL synthesis procedure as well as the molecular structures of the reactants used in the described reaction.

We repeated the described reaction cycle 20 times to obtain CMPs thin films on functionalized gold wafers.

Characterization of CMP thin films

We characterized the reaction using infrared reflection absorption spectroscopy (IRRAS). Figure 2 shows the IRRA spectrum of the CMP thin film after 20 reaction cycles and the corresponding band assignments.

The absence of bands associated to alkyne and thiol functional groups in the IRRA-spectra suggest an almost quantitative reaction. (For IRRA-spectra of the starting materials, see Supporting Information File 1, Figures S1–S3.)

We evaluated the thickness of the CMP thin film using ellipsometry. The measurements show an average thickness of about 25.1 ± 0.1 nm with a mean squared error (MSE) value of 5.69 after fitting with Cauchy mode with the parameters $A_n = 1.399$, $B_n = 0.051$, $C_n = -0.0026$, k-amplitude = 0 and exponent = 1.5 suggesting a very low surface roughness. To further confirm the thickness we performed the LbL synthesis on a sacrificial substrate [27,28]. Prior to the dissolution of the substrate, we coated the CMP thin film with a stabilizing layer of poly(methyl methacrylate) (PMMA). Upon substrate dissolution, we transferred the PMMA stabilized CMP thin film to a fresh gold substrate. After drying, we dissolved the PMMA layer in acetone, leaving only the CMP thin film. We then investigated the thickness of the film by an atomic force microscope (AFM) line scan along the edge of the film. Figure 3 shows the AFM image and the line-scan across the edge of the CMP thin film.

The AFM investigation also suggests a homogeneous thickness of the CMP thin film and the line-scan across the edge confirms

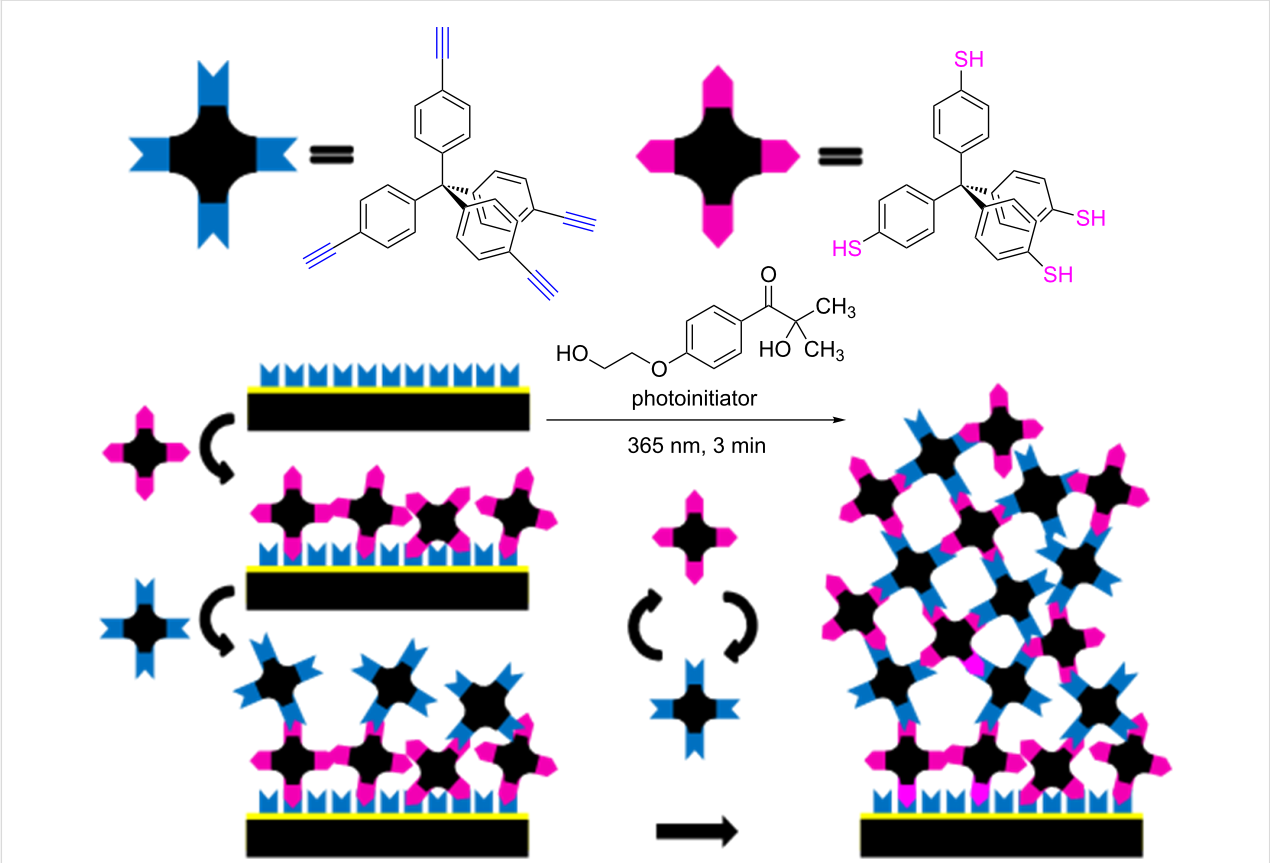

Figure 1: LbL synthesis with TPM-SH and TPM-alkyne using light-induced TYC reaction in the presence of the photoinitiator 2-hydroxy-1-[4-(2-hydroxyethoxy)phenyl]-2-methylpropan-1-one.

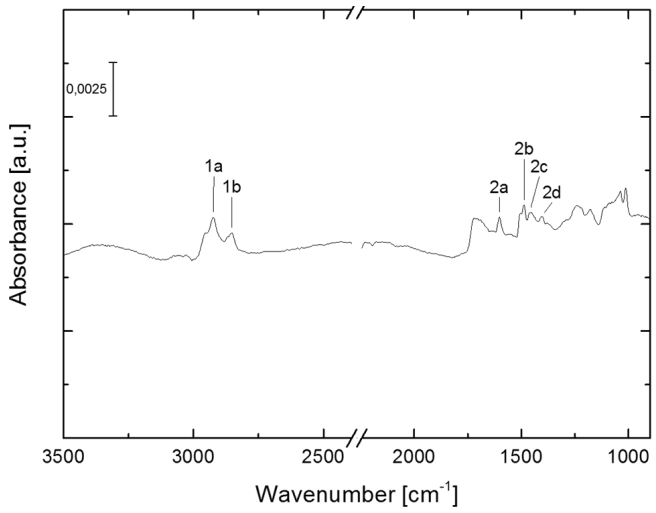

Band	Wavenumber [cm^{-1}]	Functional group
1a	2923	ν_{as} CH2
1b	2853	ν_{s} CH2
2a	1602	Vibration of aromatic backbone
2b	1487	Vibration of aromatic backbone
2c	1461	Vibration of aromatic backbone
2d	1405	Vibration of aromatic backbone

Figure 2: IRRA-Spectrum of the CMP thin film on a gold-coated silicon wafer and the corresponding band assignments.

a thickness of roughly 20 nm after 20 reaction cycles. The growth rate of roughly 1 nm per reaction cycle is in the same order as the previously described LbL synthesis of CMP nanomembranes using CuAAC click chemistry [16].

Synthesis of freestanding CMP nanomembranes

In order to produce freestanding CMP nanomembranes, we coated the CMP thin films on sacrificial substrates with a stabi-

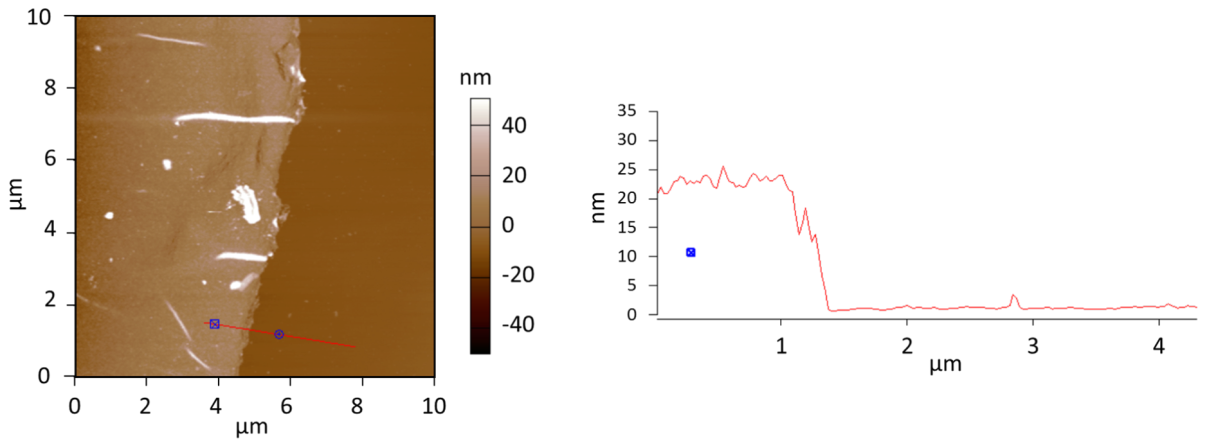

Figure 3: AFM image and line-scan across the edge of the CMP thin film.

lizing layer of PMMA containing large holes [29]. This stabilizing layer was spin-coated from a dichloromethane (DCM) solution containing PMMA and polystyrene (PS) in a weight ratio of PMMA/PS = 4:1. During spin-coating, the PS phase separates into islands, which then were selectively dissolved using cyclohexane. Afterwards we dissolved the sacrificial substrate to obtain the freestanding CMP membranes. To investigate the freestanding CMP nanomembrane we transferred it to a copper grid and recorded scanning electron microscopy (SEM) images. Figure 4 shows the SEM images of the CMP nanomembrane.

Conclusion

We described a new synthesis of CMP thin films and nanomembranes using a thiol–yne coupling (TYC) reaction. The TYC reaction allows a rapid synthesis of homogeneous thin films with a thickness of about 1 nm per reaction cycle as confirmed by ellipsometry and AFM investigations. The thin films show high mechanical stability as evidenced by the possibility to create feestanding membranes across holes of about 3–5 µm diameter. The rapid and scalable synthetic method for CMP nanomembranes described in this article, along with the possibility to transfer the nanomembranes to virtually any support, allows the integration of TYC based CMP materials in functional devices for applications in organic electronics or gas and liquid phase separation.

Experimental

Chemicals: All chemicals were purchased from commercial sources and used without further purification if not stated otherwise. Cyclohexane, dichloromethane and dry tetrahydrofuran (THF) were purchased from Merck Millipore; acetone was purchased from VWR Chemicals. Dry THF was degassed three times via freeze-pump-thaw prior to use. PMMA average M_w ≈120.000, PS average M_w ≈170.000, 2-hydroxy-1-[4-(2-hydroxyethoxy)phenyl]-2-methylpropan-1-one), iodine and

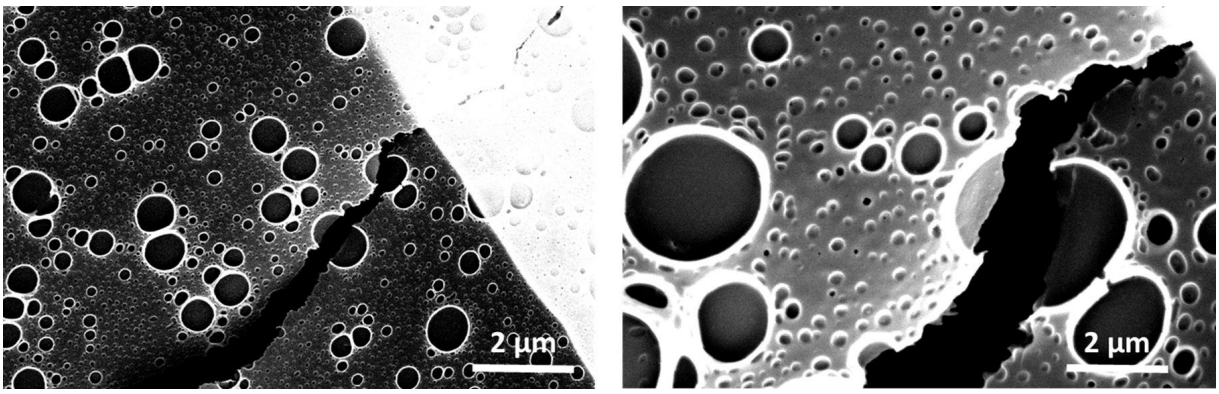

Figure 4: SEM images of freestanding CMP nanomembranes coated with a stabilizing PMMA layer containing large holes. The SEM images confirm the homogeneous thickness and freestanding nature of the CMP nanomembranes synthesized via TYC reaction.

potassium iodide were purchased from Sigma-Aldrich. TPM-SH [30] and TPM-alkyne [31] were synthesized as described in the literature.

Substrates: The sacrificial substrate consists of a 150 nm gold film on mica. For analytical measurements, we transferred the membrane to a Si(100) wafer, coated with 5 nm titanium and 100 nm gold (Au/Ti/Si). The substrates were obtained from Georg-Albert-PVD, Germany and stored under an argon atmosphere prior to use.

Infrared reflection absorption spectroscopy (IRRAS): The IRRA-spectra were recorded on a Bruker Vertex 80 purged with dried air. The IRRAS accessory (A518) has a fixed angle of incidence of 80°. The data were collected on a middle band liquid nitrogen cooled MCT detector. Perdeuterated hexadecanethiol-SAMs on Au/Ti/Si were used for reference measurements [32]. The absorption band positions are given in wavenumbers $\tilde{\nu}$ (cm^{-1}).

Scanning electron microscopy (SEM): We recorded SEM images using a FEI Philips XL30 (FEI Co., Eindhoven, NL), a field emission gun environmental scanning electron microscope (FEG-ESEM). Samples have been coated with a thin layer (about 5 nm) of a gold/palladium film in order to avoid charging and improve samples conductivity. All specimen were imaged under high-vacuum conditions (1.0 Torr), using an acceleration voltage of 20 keV.

Atomic force microscopy (AFM): AFM-imaging was performed using an Asylum Research Atomic Force Microscope, MFP-3D BIO. The AFM was operated at 25 °C in an isolated chamber in alternating current mode (AC mode). AFM cantilevers were purchased from Ultrasharptm MikroMasch. Three types of AFM-cantilevers were used, an NSC-35 (resonance frequency 315 kHz; spring constant 14 N/m), an NSC-36 (resonance frequency: 105 KHz; spring constant: 0.95 N/m) and an NSC-18 (resonance frequency: 75 kHz; spring constant: 3.5 N/m).

Self-assembled monolayer (SAM) preparation: For SAM formation, a clean gold substrate (2.2 cm × 2.2 cm) was rinsed with absolute ethanol and then immersed in a solution of *S*-[11-oxo-11-(propargylamino)undecyl] thioacetate ($AcSC_{10}H_{20}C(O)NHCH_2C{\equiv}CH$) (with a concentration of 1 mmol/L) in ethanol for 18 h. Afterwards the substrate was taken out, rinsed thoroughly with ethanol and dried in a nitrogen stream [33].

Preparation of conjugated microporous polymer (CMP) films: 6.7 mg of TPM-SH (15.0 µmol, 1.00 equiv), 6.3 mg of TPM-alkyne (15.0 µmol, 1.00 equiv) and 1.1 mg of 2-hydroxy-1-[4-(2-hydroxyethoxy)phenyl]-2-methylpropan-1-one) (5 µmol, 0.333 equiv) as photoinitiator were separately dissolved in 20 mL abs. THF. The synthesis was carried out under inert conditions using an argon atmosphere. At first, 1 mL of TPM-SH solution and 0.5 mL of the photoinitiator solution were added to the SAM coated substrate and stirred gently to ensure proper mixing. Then the mixture was exposed to 365 nm UV-light for 3 minutes. Afterwards, the substrate was rinsed with dry THF. Subsequently, 1 mL of TPM-alkyne solution and 0.5 mL of the photoinitiator solution were added to the substrate and stirred gently to ensure proper mixing. Then the mixture was exposed to 365 nm UV-light for 3 minutes. Then, the substrate was again rinsed with dry THF. The procedure was then repeated for the next reactant 20 times each. After the cycles were completed, the wafer was taken out of the inert environment, washed thoroughly with dry THF and ethanol and dried using a nitrogen stream.

Transfer of CMP nanomembranes: To obtain freestanding nanomembranes, the CMP-films were grown on sacrificial substrates using the above-described procedure. The membrane was then obtained by following a procedure described in literature [28]. First, PMMA was spin coated as a supporting layer. Then, the mica was removed by floating in solutions of $I_2/KI/H_2O$; KI/H_2O and in the last step by immersing the substrate in H_2O. The retaining gold film was etched in a solution of $I_2/KI/H_2O$. The membrane was washed 3 times with water [28]. Then the membrane was transferred to Cu-TEM grids. The obtained membrane size was 0.3 cm × 0.3 cm.

Preparation of freestanding nanomembranes: To obtain freestanding nanomembranes, the CMP-films were grown on sacrificial substrates using the above-described procedure. The membrane was then obtained by following a procedure described in literature [29]: First PMMA/PS was spin coated as a supporting layer and afterwards rinsed overnight in cyclohexane to remove the PS. Then, the mica was removed by floating in solutions of $I_2/KI/H_2O$; KI/H_2O and in the last step by immersing the substrate in H_2O. The retaining gold film was etched in a solution of $I_2/KI/H_2O$. The membrane was washed 3 times with water [28]. Afterwards the membrane was transferred to either a glass slide or a gold coated Si-wafer. The obtained membrane size was 2 cm × 2 cm.

Supporting Information

Supporting Information File 1

Additional IRRA spectra.
[http://www.beilstein-journals.org/bjoc/content/supplementary/1860-5397-13-54-S1.pdf]

Acknowledgements

We acknowledge the SFB 1176 funded by the German Research Council (DFG), the Helmholtz Association's Initiative and Networking Fund (Grant VH-NG-1147) and the Landesgraduiertenförderung Baden-Württemberg.

References

1. Srivastava, R.; Choi, M.; Ryoo, R. *Chem. Commun.* **2006,** 4489–4491. doi:10.1039/B612116K
2. Nandiyanto, A. B. D.; Kim, S.-G.; Iskandar, F.; Okuyama, K. *Microporous Mesoporous Mater.* **2009,** *120,* 447–453. doi:10.1016/j.micromeso.2008.12.019
3. Kitagawa, S.; Kitaura, R.; Noro, S.-i. *Angew. Chem., Int. Ed.* **2004,** *43,* 2334–2375. doi:10.1002/anie.200300610
4. Furukawa, H.; Cordova, K. E.; O'Keeffe, M.; Yaghi, O. M. *Science* **2013,** *341,* 1230444. doi:10.1126/science.1230444
5. Côté, A. P.; Benin, A. I.; Ockwig, N. W.; O'Keeffe, M.; Matzger, A. J.; Yaghi, O. M. *Science* **2005,** *310,* 1166–1170. doi:10.1126/science.1120411
6. Colson, J. W.; Woll, A. R.; Mukherjee, A.; Levendorf, M. P.; Spitler, E. L.; Shields, V. B.; Spencer, M. G.; Park, J.; Dichtel, W. R. *Science* **2011,** *332,* 228–231. doi:10.1126/science.1202747
7. Feng, X.; Ding, X.; Jiang, D. *Chem. Soc. Rev.* **2012,** *41,* 6010–6022. doi:10.1039/C2CS35157A
8. Davis, M. E. *Nature* **2002,** *417,* 813–821. doi:10.1038/nature00785
9. Jiang, J.-X.; Su, F.; Trewin, A.; Wood, C. D.; Campbell, N. L.; Niu, H.; Dickinson, C.; Ganin, A. Y.; Rosseinsky, M. J.; Khimyak, Y. Z.; Cooper, A. I. *Angew. Chem., Int. Ed.* **2007,** *46,* 8574–8578. doi:10.1002/anie.200701595
10. Plietzsch, O.; Schilling, C. I.; Tolev, M.; Nieger, M.; Richert, C.; Muller, T.; Bräse, S. *Org. Biomol. Chem.* **2009,** *7,* 4734–4743. doi:10.1039/B912189G
11. Ben, T.; Qiu, S. *CrystEngComm* **2013,** *15,* 17–26. doi:10.1039/C2CE25409C
12. Dawson, R.; Cooper, A. I.; Adams, D. J. *Prog. Polym. Sci.* **2012,** *37,* 530–563. doi:10.1016/j.progpolymsci.2011.09.002
13. Cheng, G.; Hasell, T.; Trewin, A.; Adams, D. J.; Cooper, A. I. *Angew. Chem., Int. Ed.* **2012,** *51,* 12727–12731. doi:10.1002/anie.201205521
14. Cheng, G.; Bonillo, B.; Sprick, R. S.; Adams, D. J.; Hasell, T.; Cooper, A. I. *Adv. Funct. Mater.* **2014,** *24,* 5219–5224. doi:10.1002/adfm.201401001
15. Gu, C.; Huang, N.; Chen, Y.; Qin, L.; Xu, H.; Zhang, S.; Li, F.; Ma, Y.; Jiang, D. *Angew. Chem., Int. Ed.* **2015,** *54,* 13594–13598. doi:10.1002/anie.201506570
16. Lindemann, P.; Tsotsalas, M.; Shishatskiy, S.; Abetz, V.; Krolla-Sidenstein, P.; Azucena, C.; Monnereau, L.; Beyer, A.; Gölzhäuser, A.; Mugnaini, V.; Gliemann, H.; Bräse, S.; Wöll, C. *Chem. Mater.* **2014,** *26,* 7189–7193. doi:10.1021/cm503924h
17. Kolb, H. C.; Finn, M. G.; Sharpless, K. B. *Angew. Chem., Int. Ed.* **2001,** *40,* 2004–2021. doi:10.1002/1521-3773(20010601)40:11<2004::AID-ANIE2004>3.0.CO;2-5
18. Massi, A.; Nanni, D. *Org. Biomol. Chem.* **2012,** *10,* 3791–3807. doi:10.1039/C2OB25217A
19. Yao, B.; Sun, J.; Qin, A.; Tang, B. Z. *Chin. Sci. Bull.* **2013,** *58,* 2711–2718. doi:10.1007/s11434-013-5892-1
20. Hoyle, C. E.; Lowe, A. B.; Bowman, C. N. *Chem. Soc. Rev.* **2010,** *39,* 1355–1387. doi:10.1039/B901979K
21. Lindemann, P.; Schade, A.; Monnereau, L.; Feng, W.; Batra, K.; Gliemann, H.; Levkin, P.; Bräse, S.; Wöll, C.; Tsotsalas, M. *J. Mater. Chem. A* **2016,** *4,* 6815–6818. doi:10.1039/c5ta09429a
22. Li, L.; Zahner, D.; Su, Y.; Gruen, C.; Davidson, G.; Levkin, P. A. *Biomaterials* **2012,** *33,* 8160–8166. doi:10.1016/j.biomaterials.2012.07.044
23. Hao, R.; Xing, R.; Xu, Z.; Hou, Y.; Gao, S.; Sun, S. *Adv. Mater.* **2010,** *22,* 2729–2742. doi:10.1002/adma.201000260
24. Schmitt, S.; Hümmer, J.; Kraus, S.; Welle, A.; Grosjean, S.; Hanke-Roos, M.; Rosenhahn, A.; Bräse, S.; Wöll, C.; Lee-Thedieck, C.; Tsotsalas, M. *Adv. Funct. Mater.* **2016,** *26,* 8455–8462. doi:10.1002/adfm.201603054
25. Quick, A. S.; de los Santos Pereira, A.; Bruns, M.; Bückmann, T.; Rodriguez-Emmenegger, C.; Wegener, M.; Barner-Kowollik, C. *Adv. Funct. Mater.* **2015,** *25,* 3735–3744. doi:10.1002/adfm.201500683
26. Köhler, M.; Ohngemach, J.; Wehner, G.; Gehlhaus, J. Photoinitiators for photopolymerization of unsaturated systems. WO Patent WO1986005777 A1, Oct 9, 1986.
27. Lindemann, P.; Trautlein, Y.; Wöll, C.; Tsotsalas, M. *J. Visualized Exp.* **2015,** e53324. doi:10.3791/53324
28. Ai, M.; Shishatskiy, S.; Wind, J.; Zhang, X.; Nottbohm, C. T.; Mellech, N.; Winter, A.; Vieker, H.; Qiu, J.; Dietz, K.-J.; Golzhauser, A.; Beyer, A. *Adv. Mater.* **2014,** *26,* 3421–3426. doi:10.1002/adma.201304536
29. Zhang, H.; Takeoka, S. *Macromolecules* **2012,** *45,* 4315–4321. doi:10.1021/ma3005394
30. Monnereau, L.; Nieger, M.; Muller, T.; Bräse, S. *Adv. Funct. Mater.* **2014,** *24,* 1054–1058. doi:10.1002/adfm.201302483
31. Pandey, P.; Farha, O. K.; Spokoyny, A. M.; Mirkin, C. A.; Kanatzidis, M. G.; Hupp, J. T.; Nguyen, S. T. *J. Mater. Chem.* **2011,** *2,* 1700–1703. doi:10.1039/C0JM03483E
32. Arnold, R.; Azzam, W.; Terfort, A.; Wöll, C. *Langmuir* **2002,** *18,* 3980–3992. doi:10.1021/la0117000
33. Chelmowski, R.; Käfer, D.; Köster, S. D.; Klasen, T.; Winkler, T.; Terfort, A.; Metzler-Nolte, N.; Wöll, C. *Langmuir* **2009,** *25,* 11480–11485. doi:10.1021/la9012813

License and Terms

BEILSTEIN JOURNAL OF ORGANIC CHEMISTRY

Energy down converting organic fluorophore functionalized mesoporous silica hybrids for monolith-coated light emitting diodes

Markus Börgardts and Thomas J. J. Müller*

Full Research Paper

Open Access

Address:
Institut für Organische Chemie und Makromolekulare Chemie, Heinrich-Heine-Universität Düsseldorf, Universitätsstr. 1, D-40225 Düsseldorf, Germany

Email:
Thomas J. J. Müller* - ThomasJJ.Mueller@uni-duesseldorf.de

* Corresponding author

Keywords:
benzofurazane; LED; luminophores; mesoporous silica hybrids; monoliths; Nile red; perylene; postsynthetic grafting; white light emission

Beilstein J. Org. Chem. **2017,** *13,* 768–778.
doi:10.3762/bjoc.13.76

Received: 21 December 2016
Accepted: 05 April 2017
Published: 25 April 2017

This article is part of the Thematic Series "Organic porous materials".

Guest Editor: S. Bräse

Abstract

The covalent attachment of organic fluorophores in mesoporous silica matrices for usage as energy down converting phosphors without employing inorganic transition or rare earth metals is reported in this article. Triethoxysilylpropyl-substituted derivatives of the blue emitting perylene, green emitting benzofurazane, and red emitting Nile red were synthesized and applied in the synthesis of mesoporous hybrid materials by postsynthetic grafting to commercially available MCM-41. These individually dye-functionalized hybrid materials are mixed in variable ratios to furnish a powder capable of emitting white light with CIE chromaticity coordinates of x = 0.33, y = 0.33 and an external quantum yield of 4.6% upon irradiation at 410 nm. Furthermore, as a proof of concept two different device setups of commercially available UV light emitting diodes, are coated with silica monoliths containing the three triethoxysilylpropyl-substituted fluorophore derivatives. These coatings are able to convert the emitted UV light into light with correlated color temperatures of very cold white (41100 K, 10700 K) as well as a greenish white emission with correlated color temperatures of about 5500 K.

Introduction

The development of new efficient illumination materials has received increasing attention in the past years [1-3]. For the generation of white light the combination of a UV emitting light source and energy down converting phosphor emitting in the full visible spectrum is an intriguing approach [4,5]. This concept bears the advantage of producing white light with a high color rendering index (CRI) as well as the generation of white light with a warm correlated color temperature (CCT) [4-6]. Usually several UV excitable red, green and blue (RGB) emitting phosphors generally relying on inorganic

luminophores, such as rare earth metals as Ce^{3+} or Eu^{2+}, are employed for white light generation [3,4,7]. However, the development of purely organic down converting phosphors would offer a sustainable and potentially cost-effective access alternative, eventually starting from renewable organic materials [8,9].

Other than inorganic luminophores these organic analogues cannot simply be intercalated in a robust inorganic host structure and, therefore, ligating materials are required. Since the host structure should not undergo photodegradation, stable structures like silica-based materials, in particular mesoporous silica, offer favorable properties [4,10]. Eventually, organic–inorganic hybrid materials can be easily accessed by covalent ligation of the functional guest chromophore to a silica host matrix [11,12]. As a consequence the inherent robustness and stability of the rigid inorganic silica material can be combined with the functionality and tunability of the organic chromophore. In addition, these mesoporous materials possess defined pore structures in which the organic dye can be homogeneously distributed [13]. Thereby aggregation induced self-quenching and singlet oxygen dependent dye degradation can be efficiently prevented [14,15]. By the rigid silica host framework bimolecular photochemical reactions are also suppressed [16]. Additionally, mesoporous materials possess the crucial advantage that they can be synthesized as transparent monoliths in different shapes [17-19]. Here, we communicate our first efforts to design red, green, and blue light-emitting mesoporous materials from organic chromophores, their blending to white light-emitting silica hybrids based upon additive color mixing, and as a proof of principle, the implementation in a white light emitting monolith for down converting commercially available UV light emitting diodes.

Results and Discussion

A general approach to mesoporous organo–silica hybrid materials takes advantage of the condensation of triethoxysilyl-functionalized functional organic molecules with inorganic silica hosts [11,20]. Therefore, a terminal triethoxysilyl group has to be coupled to luminescent dyes with blue, green, and red emission characteristics for generating hybrid materials with white light emission based upon additive color mixing. A rapid and versatile functionalization can be achieved upon ligating a triethylsiloxy-functionalized azide and a terminal alkynyl-functionalized luminophore by CuAAC (Cu-catalyzed azide–alkyne cycloaddition) [21-23].

Commencing from a 2-hydroxy-substituted Nile red **1** or 3-hydroxymethylperylene (**2**) the alkyne-substituted fluorophore derivatives **4** and **5** were accessible by Williamson ether synthesis [24]. The alkyne-functionalized green benzofurazane derivate **6** was obtained by nucleophilic aromatic substitution of 4-chloro-7-nitrobenzo[*c*][1,2,5]oxadiazole (**3**) with propargylamine. The alkyne-functionalized derivatives **4**, **5** and **6** were then reacted with azide **7** via CuAAC to furnish the triethoxysilyl-substituted luminophore precursor molecules **8** (red emission), **9** (blue emission), and **10** (green emission) (Scheme 1). In contrast to usually high yields of the CuAAC the precursor synthesis only gives yields between 44 to 45% after purification by column chromatography on silica gel [22,23]. The diminished yields are a consequence of the reaction of the terminal triethoxysilyl groups with the free silanol groups of the silica gel taking place already at room temperature.

For generating white light emission with good color rendering index and tunable color temperature the characteristics of red emissive Nile red, blue emissive perylene, and green emissive benzofurazane have to be matched with comparable emission intensity. All three chromophores exhibit absorption in the UV–vis region with comparable molar absorption coefficients (Figure 1a). Neglecting energy transfer between the luminophores superposition of the emission spectra of the three dyes covers the whole range of the visible region (400–800 nm) (Figure 1b).

The three dyes were additionally analyzed with respect to their CIE chromaticity coordinates, i.e., their fluorescence color in order to determine the color space which should be accessible by additive color mixing [25-28]. As shown in Figure 2 CIE chromaticity coordinates of the blue, green and red colors were determined as follows: perylene precursor **10**: x = 0.14, y = 0.11; benzofurazane precursor **9**: x = 0.33, y = 0.60; Nile red precursor **8**: x = 0.68, y = 0.32.

Thus, by mixing of the three precursors **8**, **10**, and **9** the color space within the triangle defined by the pure colors should be accessible. As this triangle comprises the spectrum of a black body radiator an emission of white light with tunable color temperature is possible. The synthesis of silica hybrid materials functionalized with a single dye was performed via postsynthetic grafting of commercially available MCM-41 according to literature procedures [12,13,17]. Therefore, the respective dye precursors **9**, **10**, and **8** at variable concentrations were reacted with free silanol groups displayed on the surface of MCM-41 furnishing hybrid materials with different dye loadings in a $\mu mol \cdot g^{-1}$ range. The amount of dye incorporated into the hybrid material was estimated by UV–vis spectroscopic analysis according to our previous report [24].

The synthesized materials with the corresponding dye loading and solid state quantum yields are summarized in Table 1. Especially for the Nile red-functionalized hybrid materials the highest quantum yield of 23% was obtained at a low dye

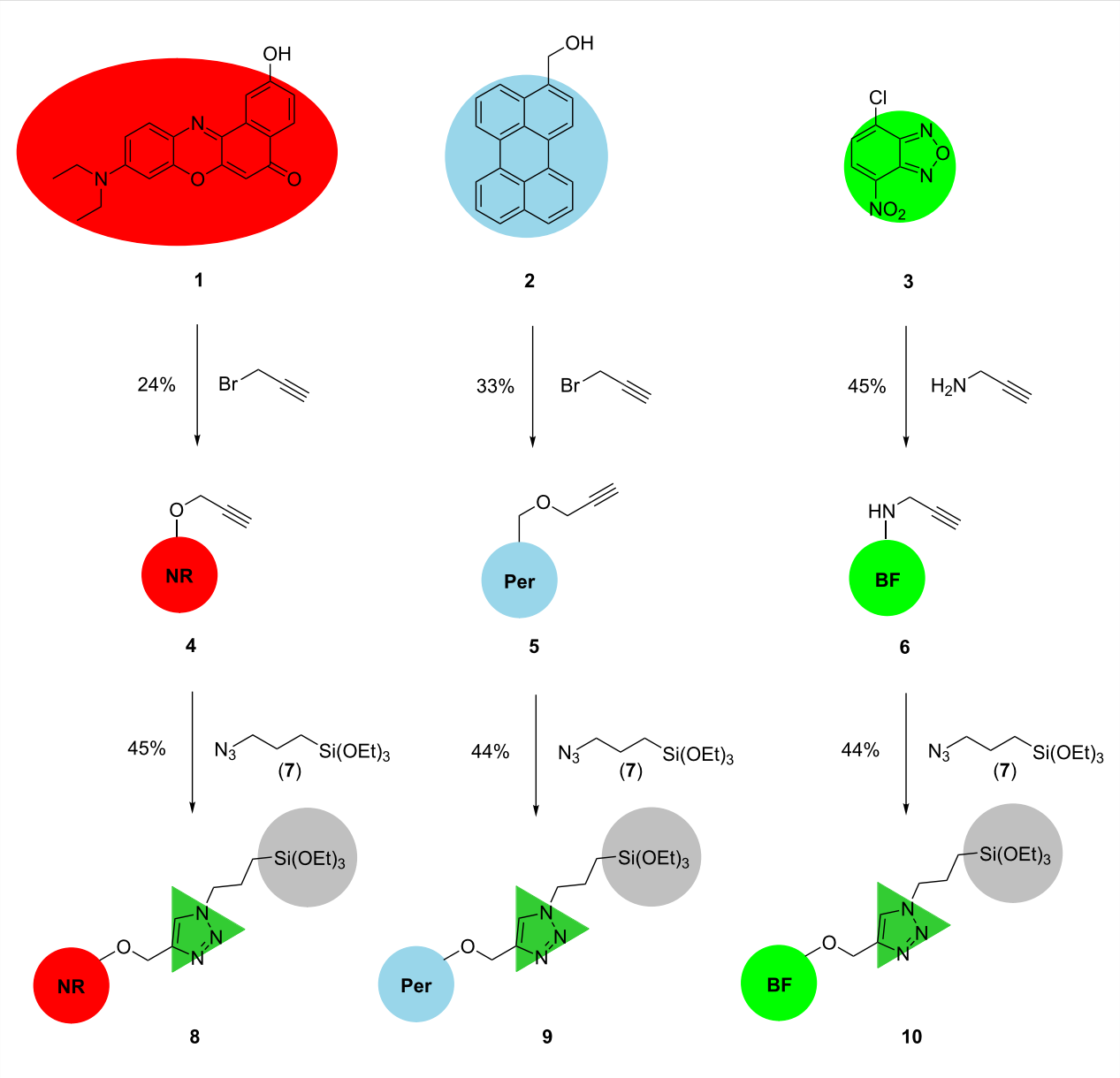

Scheme 1: Synthesis of the triethoxysilyl-functionalized dye precursors **8**, **9**, and **10**.

loading of 1.5 μmol·g^{-1} (**8@MCM-2**). A further increase of Nile red loading causes a drop of quantum yields, presumably due to self-quenching effects.

Based on the assumption that energy transfer typically occurs at distances of less than 10 nm between two dye molecules, self-quenching should be observed if more than one molecule is found in an area of 10 × 10 nm [29]. If dye loadings of the hybrids are correlated with the surface area of the silica material, typically 700 m^2·g^{-1}, self-quenching effects should occur at loadings higher than 10 μmol·g^{-1} as illustrated in Figure 3 [24]. Although aggregation-induced self-quenching can be prevented by covalently ligating dye molecules to the silica matrix, intermolecular energy transfer causing losses in quantum yield can be expected at higher dye loadings.

Likewise, for the perylene and benzofurazane-functionalized hybrid materials **9@MCM-3** and **10@MCM-6** similar dye loadings in the lower μmol·g^{-1} range were ascertained for furnishing optima of their solid-state fluorescence quantum yields Φ_f (Figure 4).

The optical properties of the dye-functionalized hybrid materials differ slightly from the properties of their precursor molecules in solution. For all hybrid materials a broad band can be observed in the spectra, which can be attributed to an inhomo-

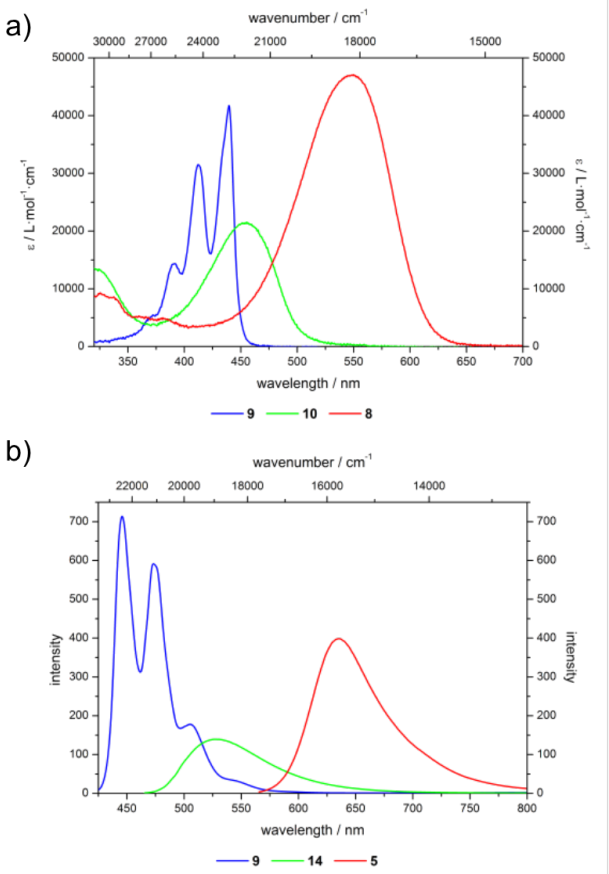

Figure 1: Absorption (a) and emission (b) spectra of perylene **9**, benzofurazane **10**, and Nile red precursors **8** (recorded in ethanol at T = 298 K; ([9] = 4.1 × 10^{-6} M, [10] = 4.0 × 10^{-6} M, [8] = 4.1 × 10^{-6} M; λ_{exc}(**9**) = 409 nm, λ_{exc}(**10**) = 450 nm, λ_{exc}(**8**) = 540 nm).

Table 1: Calculated dye loadings and solid state fluorescence quantum yields Φ_f of grafted hybrid materials.

dye@MCM	calculated dye loading [μmol·g^{-1}]	Φ_f [%]
8@MCM		
8@MCM-1	0.6 of **8**	14
8@MCM-2	1.5 of **8**	23
8@MCM-3	2.9 of **8**	20
8@MCM-4	5.9 of **8**	20
8@MCM-5	8.8 of **8**	17
8@MCM-6	12 of **8**	12
8@MCM-7	12 of **8**	11
8@MCM-8	18 of **8**	8.6
8@MCM-9	23 of **8**	6.7
9@MCM		
9@MCM-1	0.8 of **9**	5.8
9@MCM-2	2.0 of **9**	7.6
9@MCM-3	4.0 of **9**	12
9@MCM-4	6.0 of **9**	7.3
9@MCM-5	8.0 of **9**	6.6
9@MCM-6	20 of **9**	7.6
10@MCM		
10@MCM-1	1.2 of **10**	10
10@MCM-2	2.3 of **10**	17
10@MCM-3	4.6 of **10**	14
10@MCM-4	6.9 of **10**	14
10@MCM-5	9.3 of **10**	16
10@MCM-6	12 of **10**	19
10@MCM-7	16 of **10**	14

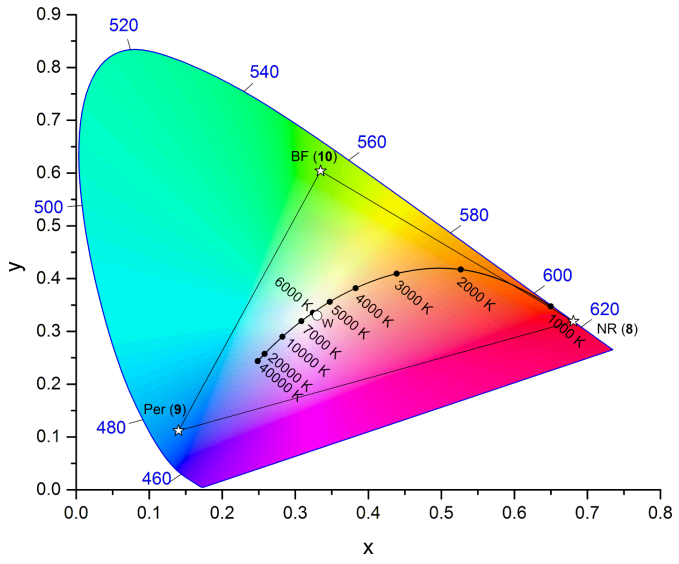

Figure 2: CIE 1931 color space chromaticity diagram (2° observer) with the CIE chromaticity coordinates of the emitting precursors **9** (blue), **10** (green), and **8** (red) in ethanol as well as the color space accessible by mixing these three precursors shown as triangle.

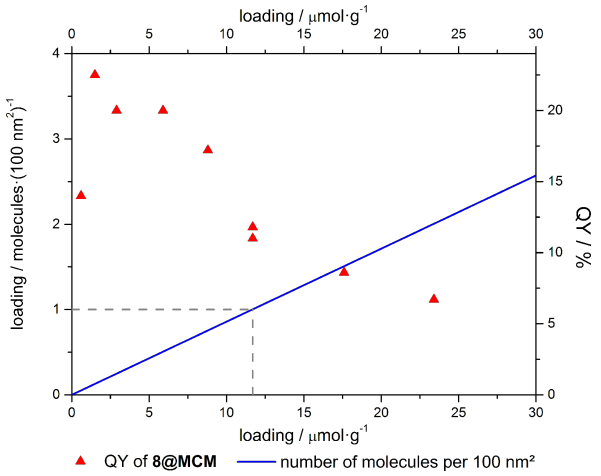

Figure 3: Number of molecules per 100 nm² and quantum yields of **8@MCM** in relation to the loading of hybrid materials.

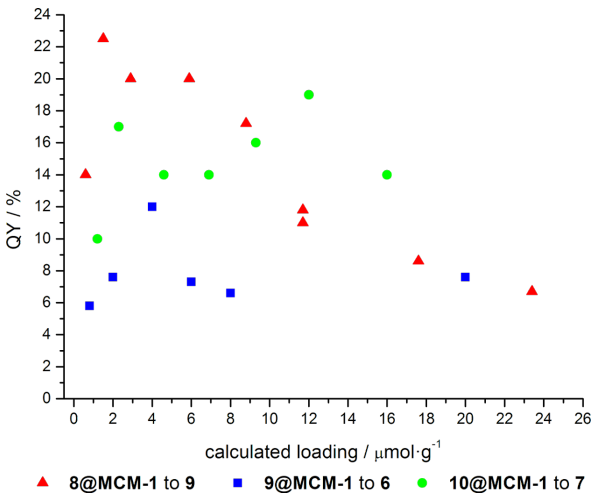

Figure 4: Solid-state fluorescence quantum yields Φ_f of grafted hybrid materials in relation to the calculated dye loading (λ_{exc}(**9@MCM**) = 409 nm, λ_{exc}(**10@MCM**)) = 450 nm, λ_{exc} (**8@MCM**)) = 540 nm).

geneous line broadening in the solid state. As benzofurazane and Nile red dyes exhibit solvatochomism, their spectral properties are clearly affected by incorporation into the polar silica environment. A detailed study of the spectral properties and solvatochromism of the Nile red hybrid materials in comparison to the precursor molecule **8** was previously reported and extensively discussed [24].

Also for perylene-functionalized hybrids a peculiar influence on the optical properties by incorporation into a silica matrix was found. Most striking is the change of the vibrational fine structure. The solution spectra of the perylene precursor **9** in ethanol show an increasing intensity of the vibrations with increasing wavelength in the absorption spectrum as well as a typical mirror image of the emission spectrum (vide supra Figure 1a and b). But as shown in Figure 7 (vide infra) for the perylene-functionalized hybrid materials, the second vibrational band becomes the most intense in the emission spectrum. This behavior clearly reflects the change in the fluorescence spectra of the free precursor at higher concentrations. This is typical for dyes with small Stokes shifts capable of inner filter and energy transfer effects.

With single dye-functionalized silica hybrid materials in hand displaying highest quantum yields, blends with tunable color temperature should be realized. In order to get an estimate of the mixing ratio of blue, green and red emitting hybrids to yield a white light emitting material upon excitation at 410 nm, a blend of the hybrid materials displaying the second highest quantum yields (**8@MCM-4**, **9@MCM-2**, **10@MCM-2**) was prepared.

Starting from a blend of **8@MCM-4**, **9@MCM-2**, **10@MCM-2** with a molar ratio of 1:0.1:0.1 the CIE coordinates were determined as x = 0.17 and y = 0.19. Thus, as this first blend was blue emissive and lacked portions of the green and red components, the amount of the green and red hybrid was increased as depicted in Table 2 with their corresponding CIE coordinates shown in Figure 5. Thereby, a blend **[8@MCM-4 + 9@MCM-2 + 10@MCM-2]-5** with CIE coordinates in the proximity of the white point could be obtained. The molar ratio of that blend was used as a starting point for the mixing of the hybrid materials with the highest quantum yields. Thus after determination of the CIE coordinates of a blend of **8@MCM-2**, **9@MCM-3** and **10@MCM-6** with a similar molar ratio, the missing color com-

Table 2: Molar ratios of the hybrid blends **[9@MCM-2 + 10@MCM-2 + 8@MCM-4]** with their corresponding CIE coordinates x and y (λ_{ex} = 410 nm).

hybrid blends	9@MCM-2	10@MCM-2	8@MCM-4	x	y
[9@MCM-2 + 10@MCM-2 + 8@MCM-4]-1	1	0.1	0.1	0.17	0.19
[9@MCM-2 + 10@MCM-2 + 8@MCM-4]-2	1	0.5	0.6	0.23	0.28
[9@MCM-2 + 10@MCM-2 + 8@MCM-4]-3	1	0.9	0.7	0.24	0.30
[9@MCM-2 + 10@MCM-2 + 8@MCM-4]-4	1	2.7	1.4	0.27	0.38
[9@MCM-2 + 10@MCM-2 + 8@MCM-4]-5	1	2.7	2.6	0.27	0.34

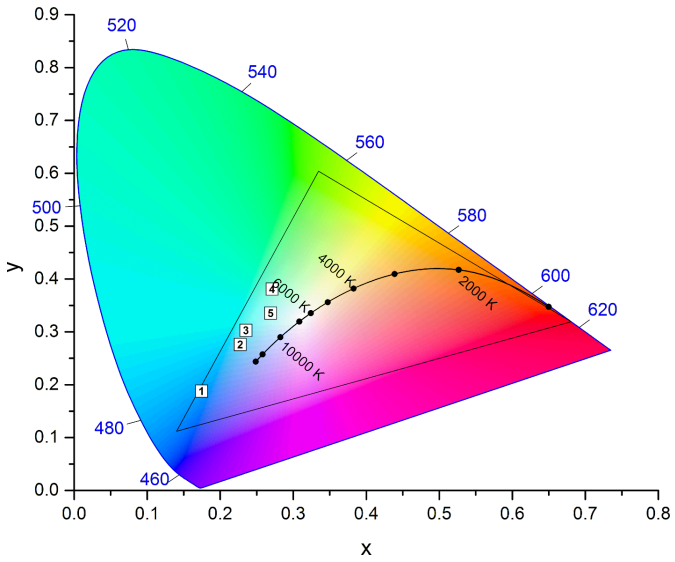

Figure 5: CIE 1931 color space chromaticity diagram (2° observer) with the color space accessible by mixing these three precursors **9** (blue), **10** (green), and **8** (red) in ethanol shown as triangle as well as the CIE coordinates of the hybrid blends **[9@MCM-2 + 10@MCM-2 + 8@MCM-4]-1** to **5**.

ponents could be admixed to yield a white light emitting powder **[8@MCM-2 + 9@MCM-3 +10@MCM-6]-1** with CIE chromaticity coordinates of x = 0.33 and y = 0.33, an external solid state fluorescence quantum yield Φ_f of 4.6% and a correlated color temperature of 5500 K (λ_{exc} = 410 nm, molar ratio: 1.0:4.9:1.3). Pictures of a blend of the hybrid materials **8@MCM-4**, **9@MCM-2**, and **10@MCM-2** upon UV excitation (λ_{exc} = 365 nm) in suspension as well as in the solid state are shown in Figure 6.

Investigation of the excitation and emission spectra of the single dye-functionalized hybrid materials **8@MCM-3**, **9@MCM-3**,

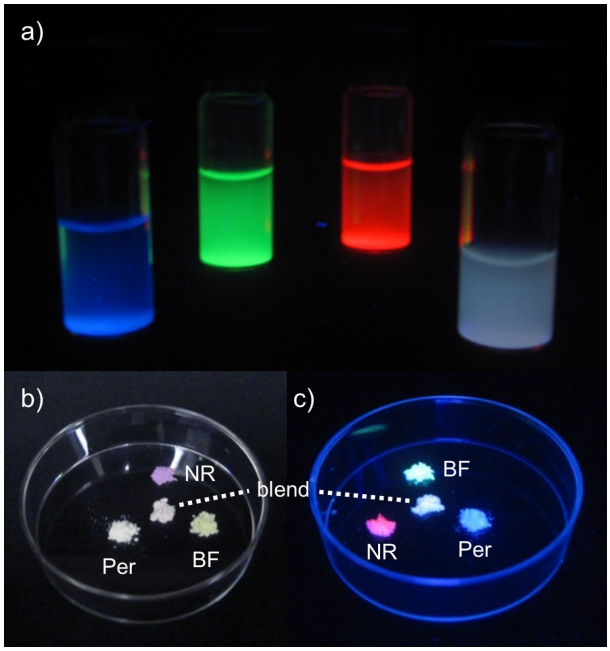

Figure 6: a) Suspensions of the dye-functionalized silica hybrid materials **8@MCM-3**, **9@MCM-3**, and **10@MCM-6** as well as their mixture in dichloromethane under UV light (λ_{exc} = 365 nm). b) Solids of dye-functionalized silica hybrid materials **8@MCM-4**, **9@MCM-2**, and **10@MCM-2** as well as their mixture under daylight. c) Solids of dye-functionalized silica hybrid materials **8@MCM-4**, **9@MCM-2**, and **10@MCM-2** as well as their mixture under UV light (λ_{exc} = 365 nm).

and **10@MCM-6** as well as their white light-emitting mixture **[8@MCM-2 + 9@MCM-3 + 10@MCM-6]-1** revealed in first approximation that blending did not alter the spectral appearance in comparison to the constituents, i.e., the recorded spectra are in agreement with an additive spectral behavior (superimposition of the individual spectra of **8@MCM-3**, **9@MCM-3**, and **10@MCM-6**) void of intermolecular energy transfer effects (Figure 7). However, minor differences in the excitation and emission spectra can be found upon comparison of the single dye-functionalized hybrids and their blend, especially for the benzofurazane part.

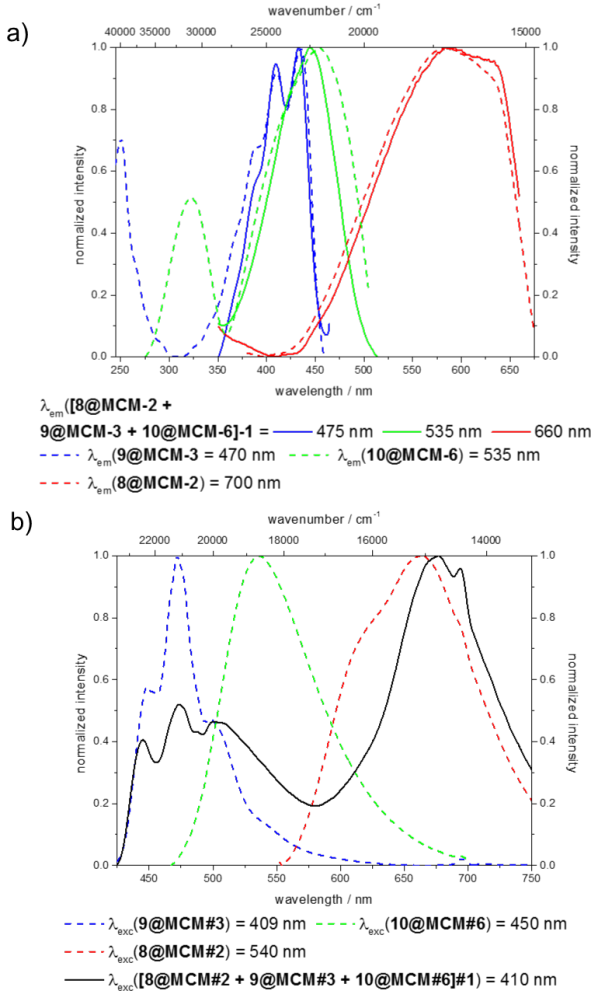

Figure 7: a) Excitation and b) emission spectra of the single dye-functionalized hybrid materials **8@MCM-2**, **9@MCM-3**, and **10@MCM-6** as well as their blend **[8@MCM-2 + 9@MCM-3 + 10@MCM-6]-1**.

In the excitation spectra the excitation of the green constituent of the blend **[8@MCM-2 + 9@MCM-3 + 10@MCM-6]-1** detected at an emission wavelength of 535 nm is bathochromically shifted compared to the excitation of the single dye-functionalized material **10@MCM-6**. This dissimilarity arises from the fact that at the emission wavelength of 535 nm not only the benzofurazane-functionalized hybrid **10@MCM-6** shows an emission, but also the perylene-functionalized hybrid **9@MCM-3** (Figure 7b). Thus the excitation spectra at an emission wavelength of 535 nm gives a superimposition of the excitation spectra of the blue and green component in the blend, resulting in a virtual blue shift of the excitation of the green component relative to the pure hybrid **10@MCM-6**.

Similarly, the emission spectra are affected as both the blue and green constituents show emissions in the range of 475–600 nm resulting in a superimposition of both emissions leading to a virtual hypsochromic shift of the emission maximum of the green component of the white light emitting powder **[8@MCM-2 + 9@MCM-3 + 10@MCM-6]-1** relative to the emission spectra of the benzofurazane-functionalized hybrid **10@MCM-6**.

Additional information on the excitation mechanism of all three chromophores was gained upon excitation with UV light and recording of emission spectra at different excitation wavelengths (Figure 8).

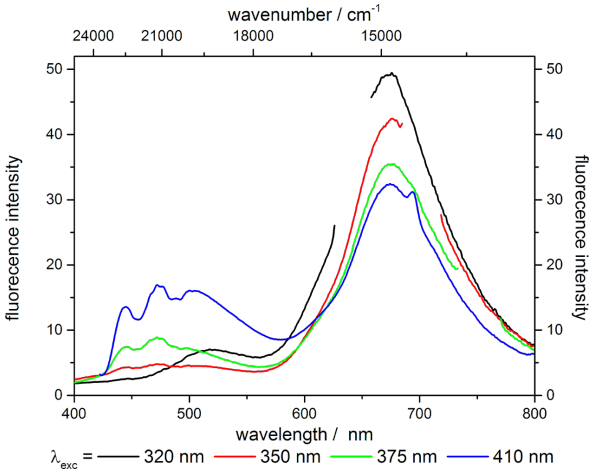

Figure 8: Emission spectra of blend **[8@MCM-2 + 9@MCM-3 + 10@MCM-6]-1** at different excitation wavelengths (2nd order of excitation beam not shown).

Upon excitation at 320 nm green as well as intense red emission was found. With increasing excitation wavelength to 350 nm the emissions in the red and green component decrease while the blue component starts to emit. Upon excitation at higher wavelengths, the emissions of the blue and green components increase while the emission intensity of the red component decreases.

These observations are in accordance with the excitation spectra shown in Figure 7a, where only the benzofurazane and Nile red hybrids are excited at 320 nm. With increasing excitation wavelength, the excitation spectra of benzofurazane and Nile red hybrids show a decrease in intensity thus explaining the decrease in fluorescence intensity for the green and red components at an excitation wavelength of 350 nm. Upon further increase of the excitation wavelength the perylene and benzofurazane hybrids show increasing fluorescence intensity as their excitation spectra concomitantly reveal increasing excitation intensity starting from 310 nm for the perylene hybrid and from 355 nm for the benzofurazane material.

As the excitation intensity of the Nile red hybrid decreases up to 400 nm, the decrease in emission intensity shown in Figure 8 is presumably due to this decrease in excitation intensity. These findings thus indicate a direct excitation of all three chromophores in the blend of **[8@MCM-2 + 9@MCM-3 + 10@MCM-6]-1**. Although reabsorption effects are possible, they seem to affect the spectra only to a minor extent, as otherwise an increase of the emission intensity of the red component in Figure 8 should be obtained as the emission intensity of the green component increases. This direct excitation of all three dyes in the blend of **[8@MCM-2 + 9@MCM-3 + 10@MCM-6]-1** also rationalizes the low external solid-state fluorescence quantum yield Φ_f of 4.6% as the red component is only poorly excited at 410 nm.

Encouraged by generating white light emitting dye-functionalized silica hybrids upon blending pure dye hybrids we considered incorporating all three dyes simultaneously for the formation of samples of monolithic silica according to literature procedures [17]. For the synthesis of monolithic materials the precursor molecules **8**, **9**, and **10** were mixed in ethanol in a ratio of 1:6:17 furnishing a perfect white emission with the CIE chromaticity coordinates of x = 0.33 and y = 0.33. This mixture was then mixed with TEOS (tetraethoxysilane), surfactant P123 (poly(ethylene glycol)-poly(propylene glycol)-poly(ethylene glycol/$(EtO)_{20}(iPrO)_{70}(EtO)_{20}$), HCl and water. After 36 h of aging at room temperature, the samples were covered with *n*-octane and aged at 60 °C for a period of 1–4 d, depending on the shape of the reaction vessel, until the samples were dry.

With this formation of white light emitting monoliths, as a proof of concept, we prepared four examples of white light emitting LEDs with organic phosphors. Therefore, UV-emitting LEDs were early immersed into the reaction mixture upon monolith formation. After aging, according to the described method, the UV emitting diodes were coated with the white light emitting hybrid materials as shown in Figure 9. Two dif-

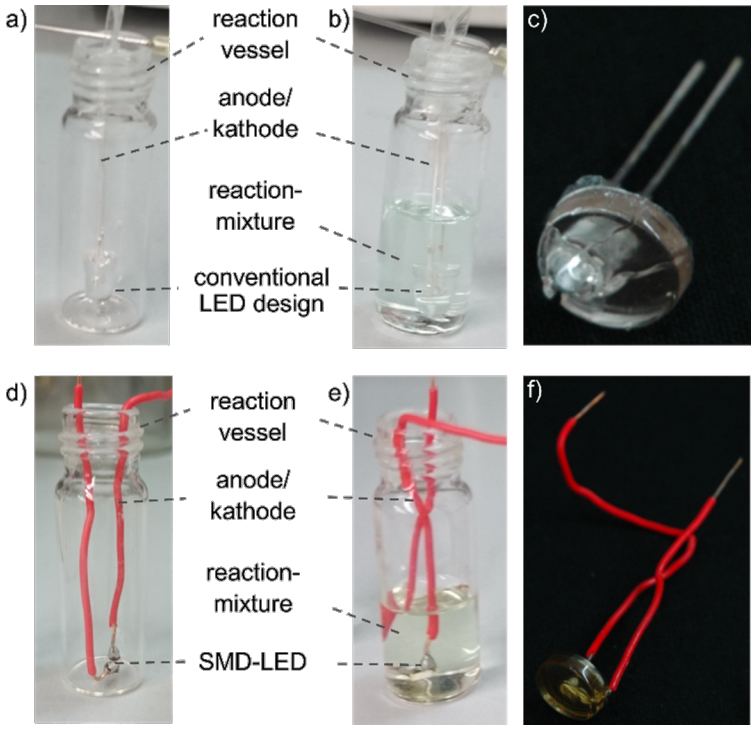

Figure 9: Coating of the a) conventional diode setup and b) surface-mounted device (SMD) (left: prior to the addition of the reaction mixture, right: after the addition), c) coated conventional diode setup, d) coated surface-mounted device.

ferent LED designs were investigated, a conventional diode setup as well as a much smaller surface mounted device (SMD).

These coated LEDs were spectroscopically analyzed displaying correlated color temperatures of 10700 K and 41100 K for the conventional LED setup, overlapping with the spectrum of the black body radiator. For the SMD setup warmer color temperatures were obtained, but their CIE chromaticity coordinates are slightly shifted from the emission of the black body radiator (Table 3, Figure 10, Figure 11).

Conclusion

In summary, we were able to synthesize triethoxysilylpropyl-substituted perylene, benzofurazane, and Nile red precursor molecules and to incorporate them into sol–gel derived silica matrices. This was achieved by postsynthetic grafting of commercially available MCM-41 yielding single dye-functionalized powders, which could be mixed to give white light-emitting powders upon excitation with UV light. Furthermore, commercially available UV emitting diodes were coated with silica monoliths composed of a mixture of the perylene, benzofurazane and Nile red precursor molecules serving as UV light converting phosphors to yield white light emission without employing of inorganic luminophores. Further optimization of the dye loadings of these monoliths as well as fine tuning of the correlated color temperatures and determination of their luminescence efficiencies is currently under way. Additionally, studies on the photostability of the hybrid materials are in the focus of further research. Further investigations are directed to the determination of quantum yields of the monolith-functional-

Table 3: CIE-coordinates x and y and correlated color temperatures of the four monolith coated LEDs.

Sample	x	y	correlated color temperature [K]
W-LED-1	0.25	0.23	41104
W-LED-2	0.27	0.29	10686
W-SMD-1	0.32	0.40	5785
W-SMD-2	0.33	0.41	5530

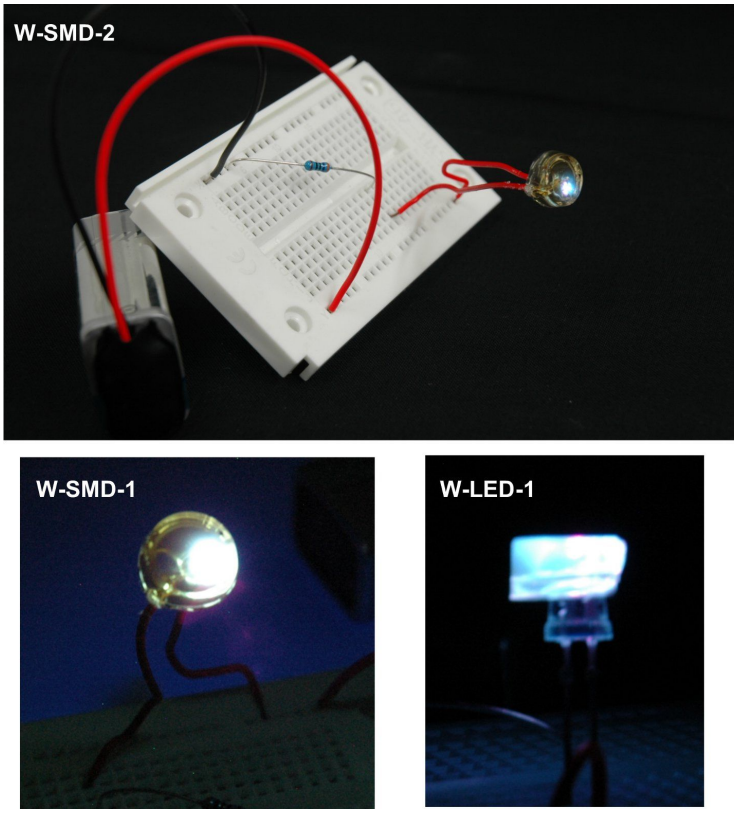

Figure 10: Pictures of the coated LEDs in compact device set-up (SMD) and conventional diode design (LED).

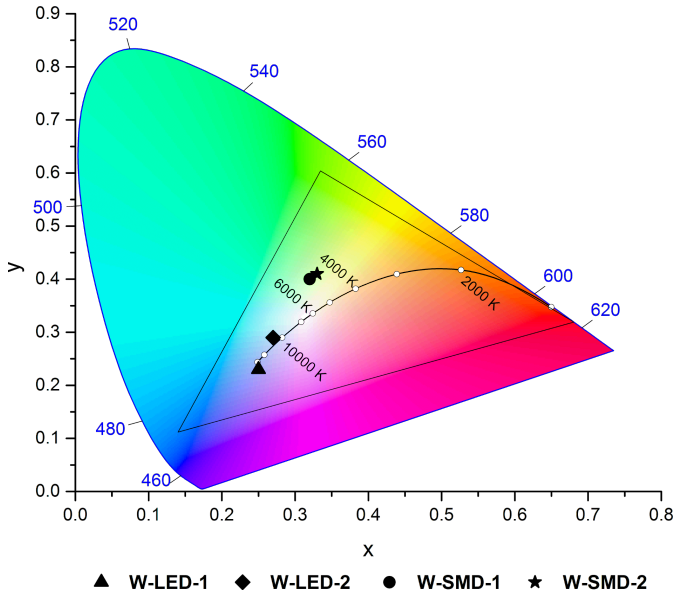

Figure 11: CIE chromaticity coordinates of the coated LEDs in compact device set-up (SMD) and conventional diode design (LED) in the CIE 1931 color space (2° standard observer).

ized materials since their quantum yields could show higher efficiencies in comparison to the powder samples due to elimination of scattering of the excitation and emission light in the silica particles.

Supporting Information

Supporting Information File 1

Multistep synthetic procedures, spectroscopic and analytical data of the precursors **9** and **10**, and the syntheses of the dye-functionalized MCM-41 hybrid materials **8@MCM**, **9@MCM**, and **10@MCM** as well as the determined dye loadings of the hybrids.
[http://www.beilstein-journals.org/bjoc/content/supplementary/1860-5397-13-76-S1.pdf]

Acknowledgements

The authors cordially thank the Strategic Research Fund of the Heinrich Heine University, the Fonds der Chemischen Industrie, and the Deutsche Forschungsgemeinschaft (Mu 1088/9-1) for financial support.

References

1. Höppe, H. A. *Angew. Chem., Int. Ed.* **2009,** *48,* 3572–3582. doi:10.1002/anie.200804005
2. George, N. C.; Denault, K. A.; Seshadri, R. *Annu. Rev. Mater. Res.* **2013,** *43,* 481–501. doi:10.1146/annurev-matsci-073012-125702
3. Lin, C. C.; Liu, R.-S. *J. Phys. Chem. Lett.* **2011,** *2,* 1268–1277. doi:10.1021/jz2002452
4. Silver, J.; Withnall, R. Color Conversion Phosphors for LEDS. In *Luminescent Materials and Applications;* Kitai, A., Ed.; John Wiley & Sons Ltd.: West Sussex, 2008; pp 75–109. doi:10.1002/9780470985687
5. Kaufmann, U.; Kunzer, M.; Köhler, K.; Obloh, H.; Pletschen, W.; Schlotter, P.; Wagner, J.; Ellens, A.; Rossner, W.; Kobusch, M. *Phys. Status Solidi A* **2002,** *192,* 246–253. doi:10.1002/1521-396X(200208)192:2<246::AID-PSSA246>3.0.CO;2-I
6. McKittrick, J.; Shea-Rohwer, L. E. *J. Am. Ceram. Soc.* **2014,** *97,* 1327–1352. doi:10.1111/jace.12943
7. Feldmann, C.; Jüstel, T.; Ronda, C. R.; Schmidt, P. J. *Adv. Funct. Mater.* **2003,** *13,* 511–516. doi:10.1002/adfm.200301005
8. Findlay, N. J.; Bruckbauer, J.; Inigo, A. R.; Breig, B.; Arumugam, S.; Wallis, D. J.; Martin, R. W.; Skabara, P. J. *Adv. Mater.* **2014,** *26,* 7290–7294. doi:10.1002/adma.201402661
9. Jung, H.-S.; Kim, Y.-J.; Ha, S.-W.; Lee, J.-K. *J. Mater. Chem. C* **2013,** *1,* 5879–5884. doi:10.1039/C3TC30967C
10. Mizoshita, N.; Goto, Y.; Tani, T.; Inagaki, S. *Adv. Mater.* **2009,** *21,* 4798–4801. doi:10.1002/adma.200901168
11. Hoffmann, F.; Cornelius, M.; Morell, J.; Fröba, M. *Angew. Chem., Int. Ed.* **2006,** *45,* 3216–3251. doi:10.1002/anie.200503075
12. Lim, M. H.; Stein, A. *Chem. Mater.* **1999,** *11,* 3285–3295. doi:10.1021/cm990369r
13. Hemgesberg, M.; Dörr, G.; Schmitt, Y.; Seifert, A.; Zhou, Z.; Klupp Taylor, R.; Bay, S.; Ernst, S.; Gerhards, M.; Müller, T. J. J.; Thiel, W. R. *Beilstein J. Nanotechnol.* **2011,** *2,* 284–292. doi:10.3762/bjnano.2.33
14. Kajiwara, Y.; Nagai, A.; Chujo, Y. *J. Mater. Chem.* **2010,** *20,* 2985–2992. doi:10.1039/B923449G
15. Kajiwara, Y.; Nagai, A.; Tanaka, K.; Chujo, Y. *J. Mater. Chem. C* **2013,** *1,* 4437–4444. doi:10.1039/C3TC30276H

16. Costela, A.; García-Moreno, I.; Gómez, C.; García, O.; Sastre, R. *Chem. Phys. Lett.* **2003,** *369,* 656–661.
17. Yang, H.; Shi, Q.; Tian, B.; Xie, S.; Zhang, F.; Yan, Y.; Tu, B.; Zhao, D. *Chem. Mater.* **2003,** *15,* 536–541. doi:10.1021/cm020135z
18. Sachse, A.; Galarneau, A.; Fajula, F.; Di Renzo, F.; Creux, P.; Coq, B. *Microporous Mesoporous Mater.* **2011,** *140,* 58–68. doi:10.1016/j.micromeso.2010.10.044
19. El-Safty, S. A. *J. Porous Mater.* **2011,** *18,* 259–287. doi:10.1007/s10934-010-9390-4
20. Chauhan, B. P. S. *Hybrid Nanomaterials: Synthesis, Characterization, and Applications;* John Wiley & Sons Ltd.: Hoboken, New Jersey, 2011. doi:10.1002/9781118003497
21. Rostovtsev, V. V.; Green, L. G.; Folkin, V. V.; Sharpless, K. B. *Angew. Chem., Int. Ed.* **2002,** *41,* 2596–2599. doi:10.1002/1521-3773(20020715)41:14<2596::AID-ANIE2596>3.0.CO;2-4
22. Himo, F.; Lovell, T.; Hilgraf, R.; Rostovtsev, V. V.; Noodleman, L.; Sharpless, K. B.; Fokin, V. V. *J. Am. Chem. Soc.* **2005,** *127,* 210–216. doi:10.1021/ja0471525
23. Bock, V. D.; Hiemstra, H.; van Maarseveen, J. H. *Eur. J. Org. Chem.* **2006,** 51–68. doi:10.1002/ejoc.200500483
24. Börgardts, M.; Verlinden, K.; Neidhardt, M.; Wöhrle, T.; Herbst, A.; Laschat, S.; Janiak, C.; Müller, T. J. J. *RSC Adv.* **2016,** *6,* 6209–6222. doi:10.1039/C5RA22736D
25. Schanda, J., Ed. *Colorimetry - Understanding the CIE System;* John Wiley & Sons Inc.: New Jersey, 2007. doi:10.1002/9780470175637
26. Wyszecki, G.; Stiles, W. S. *Color Science: Concepts and Methods, Quantitative Data and Formulae,* 2nd ed.; John Wiley & Sons: New York, 2000.
27. Chamberlin, G. J.; Chamberlin, D. G. *Colour Its Measurement, Computation and Application;* Heyden & Son Ltd.: London, Philadelphia, Rheine, 1979.
28. Colour Matching Functions. Colour & Vision Research laboratory and database (CVRL). http://www.cvrl.org/cmfs.htm (accessed April 23, 2016).
29. Lakowicz, J. R., Ed. *Principles of Fluorescence Spectroscopy,* 3rd ed.; Springer: New York, 2006. doi:10.1007/978-0-387-46312-4

License and Terms

BEILSTEIN JOURNAL OF ORGANIC CHEMISTRY

Sugar-based micro/mesoporous hypercross-linked polymers with in situ embedded silver nanoparticles for catalytic reduction

Qing Yin[1,2], Qi Chen[*2,§], Li-Can Lu[*1,¶] and Bao-Hang Han[*2,†]

Full Research Paper

Open Access

Address:
[1]College of Chemistry, Xiangtan University, Xiangtan 411105, China and [2]CAS Key Laboratory of Nanosystem and Hierarchical Fabrication, CAS Center for Excellence in Nanoscience, National Center for Nanoscience and Technology, Beijing 100190, China

Email:
Qi Chen[*] - chenq@nanoctr.cn; Li-Can Lu[*] - lulican@xtu.edu.cn; Bao-Hang Han[*] - hanbh@nanoctr.cn

* Corresponding author
§ Tel: +86 10 8254 5708
¶ Tel: +86 731 5829 2207
† Tel: +86 10 8254 5576

Keywords:
catalytic reduction; hypercross-linking; porous polymers; silver nanoparticles; sugar

Beilstein J. Org. Chem. **2017,** *13,* 1212–1221.
doi:10.3762/bjoc.13.120

Received: 22 February 2017
Accepted: 23 May 2017
Published: 22 June 2017

This article is part of the Thematic Series "Organic porous materials".

Guest Editor: S. Bräse

Abstract

Porous hypercross-linked polymers based on perbenzylated monosugars (**SugPOP-1–3**) have been synthesized by Friedel–Crafts reaction using formaldehyde dimethyl acetal as an external cross-linker. Three perbenzylated monosugars with similar chemical structure were used as monomers in order to tune the porosity. These obtained polymers exhibit microporous and mesoporous features. The highest Brunauer–Emmett–Teller specific surface area for the resulting polymers was found to be 1220 $m^2\ g^{-1}$, and the related carbon dioxide storage capacity was found to be 14.4 wt % at 1.0 bar and 273 K. As the prepared porous polymer **SugPOP-1** is based on hemiacetal glucose, Ag nanoparticles (AgNPs) can be successfully incorporated into the polymer by an in situ chemical reduction of freshly prepared Tollens' reagent. The obtained AgNPs/**SugPOP-1** composite demonstrates good catalytic activity in the reduction of 4-nitrophenol (4-NP) with an activity factor $k_a = 51.4\ s^{-1}\ g^{-1}$, which is higher than some reported AgNP-containing composite materials.

Introduction

Hypercross-linked polymers (HCPs) are microporous organic materials with a high specific surface area (SSA) [1,2]. The preparation of HCPs mainly includes three different synthesis strategies, namely postcross-linking of polymeric precursors containing functional groups [3], the "knitting" of rigid aromatic building blocks by external cross-linkers [4], and self-polycondensation of small molecular monomers [5]. Since the Tan group proposed the new synthetic strategy that "knits" low func-

tionality rigid aromatic compounds with formaldehyde dimethyl acetal (FDA) as an external cross-linking agent through a Friedel–Crafts reaction to synthesize a polymer network with a high SSA [6], HCPs with knitted building blocks have been widely utilized because of their high SSA [7,8], mild synthesis conditions [9,10], and wide range of monomers [11].

The porosity and functionality of HCPs is highly dependent on the core structural monomers [12-15]. However, most aromatic skeleton monomers are non-renewable and could generate additional environmental problems. Therefore, the selection and use of low cost, green, raw materials is critical. Sugars are a ubiquitous resource, which plays many different and important roles in the world [16]. The chemical structure of monosaccharides is commonly a polyhydroxylated aldehyde or ketone with a pyranose ring structure. These hydroxy groups can be easily benzylated to afford sugar-based monomers containing multiple aromatic skeletons. Recently, Liu and Dai have reported a class of novel microporous HCPs based on carbohydrates for carbon dioxide capture and storage by hydrogen bonding and dipole–quadrupole interactions [17]. The reported pore-size distribution (PSD) and related porosity tuning are in the range of micropore size. Considering that the polyhydroxylated and chiral structure derived from the monosaccharide has certain effects on the SSA and PSD of the prepared porous polymers, porosity tuning can be likely achieved with varying monomer molecular structures. Moreover, the aldehyde or ketone groups of the material provide the possibility for further modification and functionalization of the materials.

Silver nanoparticles (AgNPs) have received extensive attention because of their unique properties and applications in catalysis [18], antibacterial use [19], phase separation [20], surface-enhanced Raman scattering (SERS) [21], etc. Compared with bulk silver, AgNPs have a more negative reduction potential and higher SSA, which make them more effective in catalytic reactions [22]. However, AgNPs with high surface energy are subject to certain limitations in catalysis due to their extreme tendency to aggregate. In order to solve this problem, an effective method is to encapsulate or embed the AgNPs into a supporting matrix. The loading of AgNPs on different substrates has been reported, for instance, SiO_2 [23], TiO_2 [24], Al_2O_3 [25], porous carbon [26], carbonaceous matrix [27], carboxymethyl chitosan [28], zeolite [29], cellulose [30], ZnO paper [31] and polymers such as PVP [32-34]. In the catalytic process, porous organic polymers with a high SSA, low framework density and permanent porosity represent a new type of catalyst support [35-37]. The porosity of the matrix can particularly improve the efficiency of the catalyst due to the promotion of the reactant molecules into the holes with the catalyst active sites [38,39]. Therefore, it is of great interest to improve the catalytic efficiency by encapsulating the nanocatalyst in a porous organic polymer.

Keeping these issues in mind, three novel sugar-based porous organic polymers **SugPOP-1–3** were designed and synthesized using a Friedel–Crafts hypercross-linking reaction via knitted perbenzylated monosugars by FDA. Three perbenzylated monosugars **Sug-1–3** having similar chemical structure were used as monomers to tune the porosity and PSD. The SSA values of the obtained porous polymer are around 1000 $m^2\ g^{-1}$. As the porous polymer **SugPOP-1** is based on hemiacetal glucose, it was further postfunctionalized to embed the AgNPs into the material using an in situ chemical reduction of the freshly prepared Tollens' reagent. The related catalytic reduction by the AgNPs/**SugPOP-1** composite was also explored at room temperature.

Results and Discussion

All the sugar-based porous organic polymers (**SugPOP-1–3**) were synthesized by Friedel–Crafts reaction using FDA as an external cross-linker in a similar way. The preparation routes are shown in Scheme 1. Using benzylated monosaccharides as monomers and FDA as the cross-linker, the Friedel–Crafts cross-linking polymerization is promoted smoothly by anhydrous $FeCl_3$ in dry 1,2-dichloroethane (DCE). The monomers were either commercially available (**Sug-1**) or prepared (**Sug-2** and **Sug-3**) by benzylation of free sugars with benzyl bromide and sodium hydride. The chemical structures of **Sug-2** and **Sug-3** have been characterized by ^{1}H NMR, ^{13}C NMR, and MALDI–TOF MS.

The chemical structure of the obtained polymers was confirmed by ^{13}C CP/MAS NMR and Fourier transform infrared spectroscopy (FTIR) (Figure S1, Supporting Information File 1). For example, the backbone and structure features of **SugPOP-3** are characterized by ^{13}C CP/MAS NMR shown in Figure 1. The resonance signals of the polymer are located at 145–110, 90–50, and 50–15 ppm. The aromatic carbons resonate in the range of 145–110 ppm and the signals at 90–50 ppm are attributed to the carbon backbone of the sugar and methylene carbons connected to the oxygen atom in **SugPOP-3**. Furthermore, the resonance peaks at 50–15 ppm are assigned to the methylene carbons connecting the phenyl rings and to the methyl groups present in the sugar backbone or to the incompletely reacted linker. The ^{13}C CP/MAS NMR spectra for **SugPOP-1** and **SugPOP-2** are shown in Figures S2 and S3 (Supporting Information File 1) and show similar resonance intensities to **SugPOP-3**. All of the polymer samples show some common properties of cross-linked polymers such as stability and insolubility in common solvents. The thermal stability of **SugPOP-1–3** was characterized by thermogravimetric analysis

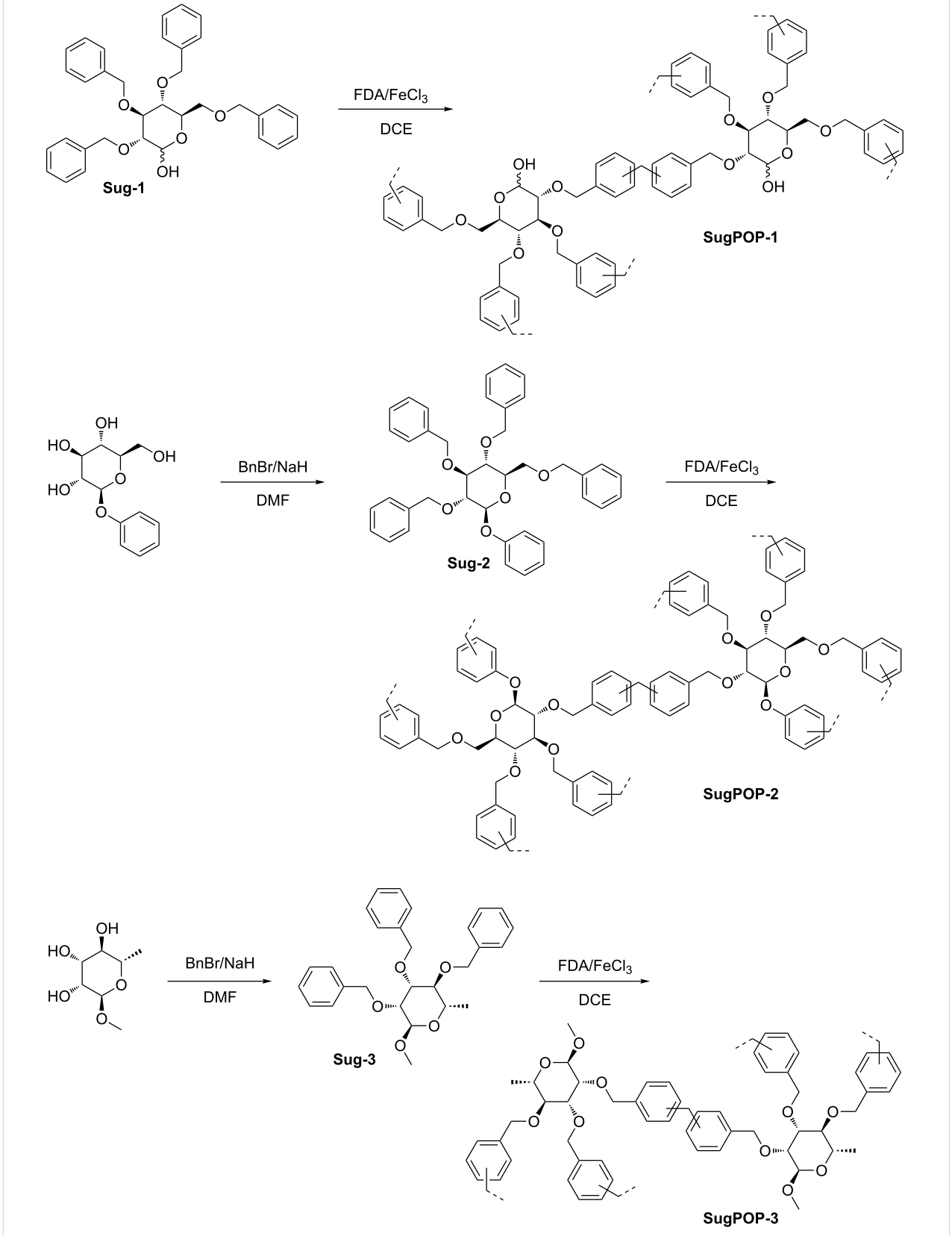

Scheme 1: Preparation of polymers **SugPOP-1–3** (FDA: formaldehyde dimethyl acetal).

(TGA) under nitrogen atmosphere (Figure S4, Supporting Information File 1). The TGA plots show that the decomposition temperature of the polymers is at about 300 °C and there is 35% mass loss when the temperature reaches 800 °C, indicating good thermal stability of the obtained polymers.

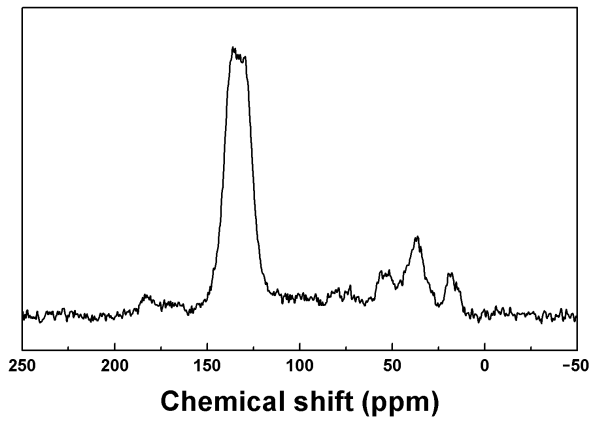

Figure 1: ^{13}C CP/MAS NMR spectrum of **SugPOP-3**.

The nitrogen adsorption–desorption isotherms (Figure 2a) of **SugPOP-1–3** were measured at 77 K to explore the porosity of the obtained polymers. Both **SugPOP-1** and **SugPOP-3** show the combination of type I and IV sorption isotherms according to the IUPAC classification, whereas **SugPOP-2** displays a type I sorption isotherm. A rapid uptake curve reflects the microporous monolayer adsorption tendency at low relative pressure ($p/p_0 < 0.10$). As for **SugPOP-1** and **SugPOP-3**, the significant hysteresis loops ($0.50 < p/p_0 < 1.00$) are consistent with the mesoporous structure. The SSA value (BET) of **SugPOP-1** was found to be as high as 1220 m^2 g^{-1} and about 1000 m^2 g^{-1} for **SugPOP-2** and **SugPOP-3**. The PSD profiles for all polymers (based on the nonlinear density functional theory (NLDFT) method) are shown in Figure 2b. The dominant PSD peaks for polymer **SugPOP-2** are located at around 0.53 and 1.35 nm. As for polymers **SugPOP-1** and **SugPOP-3**, their dominant pore size peaks are located around 0.53 and 1.30 nm, associated with mesoporous distribution between 2.2 and 7.0 nm, quantifying

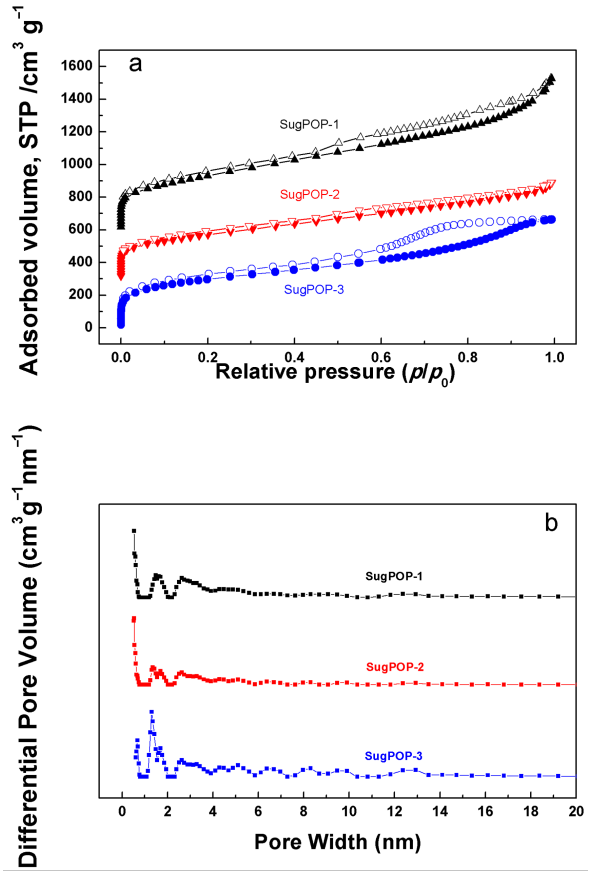

Figure 2: (a) Nitrogen adsorption–desorption isotherms of **SugPOP-1–3** measured at 77 K. For clarity, the isotherms of **SugPOP-1** and **SugPOP-2** were shifted vertically by 600 and 300 cm^3 g^{-1}, respectively. (b) PSD profiles of **SugPOP-1–3** calculated by NLDFT analysis at 77 K.

their micro/mesoporous features. The main porosity data of the obtained polymers, including SSA, pore volume, and pore size, are calculated based on the corresponding isotherms and listed in Table 1.

Such HCPs with a high SSA and micro/mesopore distribution inspired us to explore their gas uptake capacity. The CO_2 adsorption isotherms of the three polymers at 1.0 bar and 273 K

Table 1: Porosity data and gas sorption performance of **SugPOP-1–3**.

Polymers	S_{BET} (m^2 g^{-1})[a]	V_{Total} (cm^3 g^{-1})[b]	D_{pore} (nm)[c]	CO_2 uptake (wt %)[d]
SugPOP-1	1220	1.35	0.53, 1.48, 2.4–6.0	14.4
SugPOP-2	970	0.85	0.53, 1.35–2.63	12.8
SugPOP-3	1060	0.97	0.68, 1.30, 2.20–7.10	10.5

[a]SSA calculated from the nitrogen adsorption isotherm using the BET method in the relative pressure (p/p_0) range from 0.01 to 0.10. [b]Total pore volume at p/p_0 = 0.99. [c]Pore size calculated from the nitrogen adsorption isotherm using the NLDFT method. [d]Data were obtained at 1.0 bar and 273 K.

are shown in Figure S5 (Supporting Information File 1). The polymer **SugPOP-1** having a higher SSA and pore volume also exhibits a higher CO_2 adsorption capacity (14.4 wt %) than **SugPOP-2** (12.8 wt %) and **SugPOP-3** (10.5 wt %). Additionally, the hydroxy-group-bearing **SugPOP-1** can form hydrogen bonds with carbon dioxide, which may increase the affinity to carbon dioxide. Compared with the reported polymer Glc-3 [17] (prepared using the same monomer as for **SugPOP-1** and with a similar method), the polymer **SugPOP-1** also possesses a higher CO_2 adsorption capacity due to its higher porosity.

Compared with a class of microporous HCPs obtained by a similar method based on carbohydrates reported by Liu and Dai [17], our obtained porous polymers not only exhibit micro/mesoporous features, but can also be modified and functionalized for further applications. The porous organic polymer **SugPOP-1** containing an aldehyde functionality can be used as the supporting matrix to load AgNPs by treatment with Tollens' reagent through a redox reaction (Scheme 2) [40]. After **SugPOP-1** was stirred into the freshly prepared Tollens' reagent solution at 45 °C for 24 h in the dark, the obtained composite was washed with water to remove soluble impurities and dried, resulting in a dark brown solid. The formation process of a AgNPs/**SugPOP-1** composite together with the related morphology of the matrix and AgNPs were studied by TEM. As shown in Figure 3a–d, with increased reaction time, the AgNPs gradually grow and the particle size become apparently larger from 2–10 nm (8 h) to 5–20 nm (24 h). The SEM image of the AgNPs/**SugPOP-1** composite shows that many AgNPs are loaded onto the surface of the matrix (Figure 3e). The corresponding energy-dispersive X-ray spectroscopy (EDX) technique indicates that AgNPs are successfully loaded in **SugPOP-1** (Figure 3f). The weight percentage of carbon, oxygen, and silver is 85.33%, 7.21% and 7.46%, respectively. The atomic percentage of carbon, oxygen and silver is 93.18%, 5.91% and 0.91%, respectively.

The as-synthesized AgNPs/**SugPOP-1** composite was also characterized by X-ray diffraction (XRD) with the results given in Figure S6 (Supporting Information File 1). No crystal diffraction peaks were observed in the **SugPOP-1**, while the diffraction peaks for the AgNPs/**SugPOP-1** composite appeared at 2θ of 38.1°, 44.3°, 64.5°, and 77.4° corresponding to the characteristic peaks of silver [41]. These broad diffraction peaks suggest

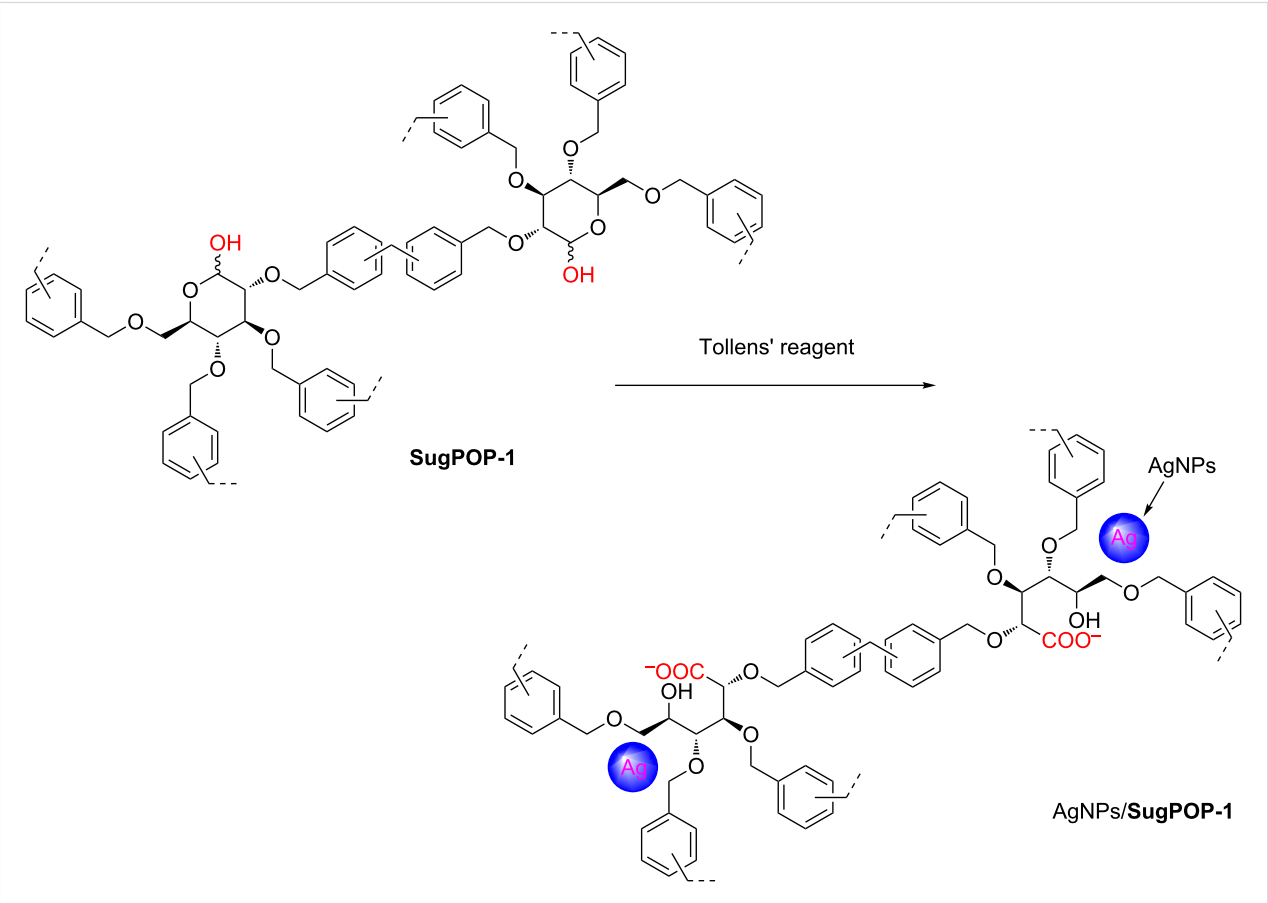

Scheme 2: The preparation of AgNPs/**SugPOP-1** composite by the in situ production of AgNPs.

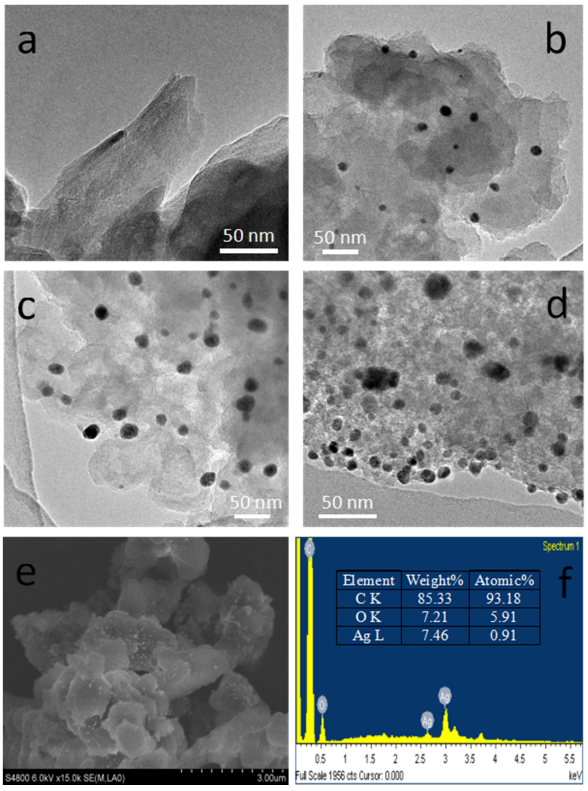

Figure 3: TEM images of the AgNPs/**SugPOP-1** composite taken at different reaction times: (a) 0 h, (b) 8 h; (c) 16 h; (d) 24 h. (e) SEM image and (f) the corresponding EDX data of the AgNPs/**SugPOP-1** composite obtained after reaction for 24 h.

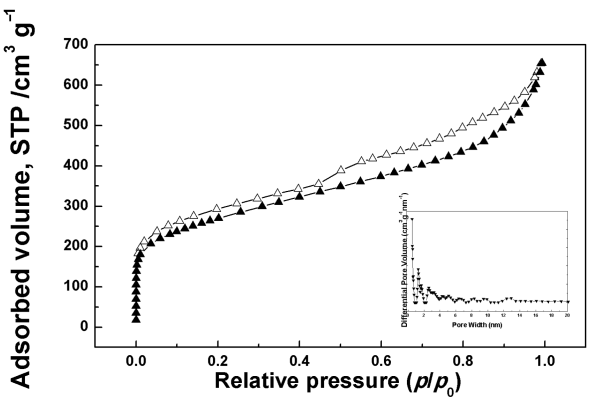

Figure 4: Nitrogen sorption isotherm at 77 K and the pore size distribution profile calculated by NLDFT analysis (inset) of the AgNPs/**SugPOP-1** composite.

the formation of small-sized AgNPs. The actual loading capacity of Ag is 5.4 wt % as discerned by TGA under air atmosphere. Meanwhile, the AgNPs/**SugPOP-1** composite exhibits about 2% mass loss at 310 °C and good thermal stability (Figure S7 in Supporting Information File 1).

The nitrogen adsorption–desorption isotherm of the AgNPs/**SugPOP-1** composite at 77 K and the corresponding PSD profile are shown in Figure 4. The SSA value (BET) of the AgNPs/**SugPOP-1** composite (960 m^2 g^{-1}) is obviously reduced (1220 m^2 g^{-1} before AgNP loading). However, its nitrogen adsorption–desorption isotherm and PSD are similar to **SugPOP-1**. The as-synthesized AgNPs/**SugPOP-1** composite also exhibits microporous and mesoporous features in which the micropore sizes are between 0.98–1.81 nm and mesopore sizes are in the range of 2–15 nm (based on NLDFT analysis).

The AgNPs loaded on the polymer demonstrate good catalytic activity, which takes on important implications for the conversion of nitro compound precursors or intermediates to the corresponding amino or amine compounds in the preparation of pharmaceuticals and agrochemicals [42,43]. 4-Nitrophenol (4-NP) can cause water pollution, which has aroused widespread concern, while its reduced product, 4-aminophenol (4-AP), is an industrial intermediate for uses such as anticorrosion lubricants and analgesic and antipyretic drugs [44]. The catalytic activity of the AgNPs/**SugPOP-1** composite was tested by the reduction of 4-NP at room temperature with an excess amount of $NaBH_4$ as the reducing reagent [45]. In our study, the process of the catalytic reaction was readily followed as the color of the solution turned from yellow to colorless. Both the reactants and products are easily monitored by UV–vis spectroscopy without any formation of appreciable byproduct.

Figure 5a shows the performance of the reduction of 4-NP in the presence of the AgNPs/**SugPOP-1** composite as catalyst at different times. As can been seen, the absorption peak at 400 nm gradually decreased, accompanied by emergence of a new peak at approximately 300 nm. Compared to the absorption peak at 317 nm of observed for the neutral 4-NP solution, the absorption at 400 nm is attributed to the 4-nitrophenolate ion. The latter is generated through deprotonation of 4-NP (pK_a = 7.15) upon the addition of $NaBH_4$ [41]. As can be seen from Figure 5a, the absorption peak of the substrate gradually decreased with reaction time due to its conversion. At the same time, the product formation of 4-AP is evident from the new UV–vis band at about 300 nm [46]. There is no byproduct formed during the reaction as the spectra for different reaction times intersect at 283 and 316 nm [47]. After 870 s, the absorption peak at 400 nm disappeared, implying full conversion of 4-NP to 4-AP.

The reaction kinetics of the reduction of 4-NP is considered to be pseudo-first order [48] and can be expressed by the following equation:

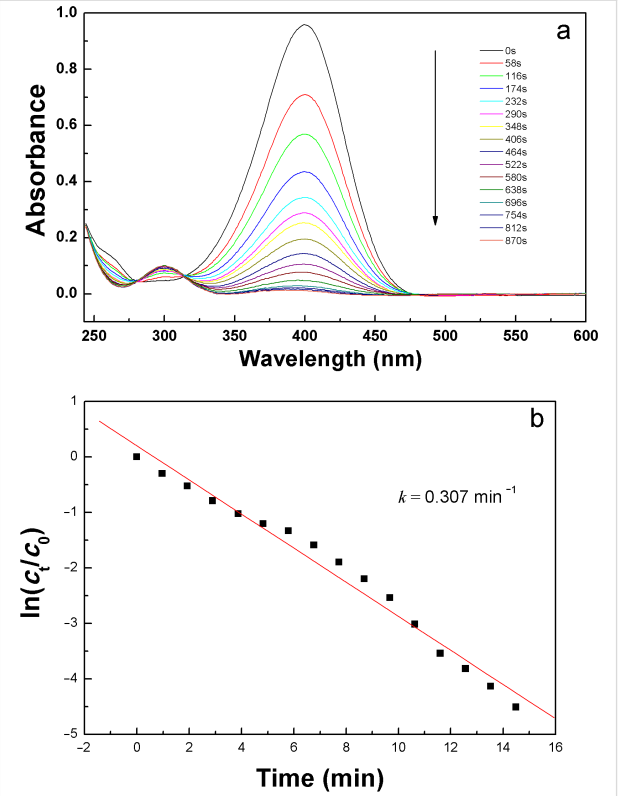

Figure 5: Catalytic performance of the AgNPs/**SugPOP-1** composite. Time-dependent UV–vis spectral changes (a) and the kinetic curve (b) for the catalytic reduction of 4-nitrophenol (4-NP) to 4-aminophenol (4-AP) at room temperature.

$$-r_t = \frac{-dc}{dt} = kt$$

where r_t is the consumption rate of 4-NP at time t, c_t is the concentration of 4-NP at time t, and k is the first-order rate constant.

Figure 5b shows the c_t/c_0 and $\ln(c_t/c_0)$ changes with time for the reduction of 4-NP in the presence of $NaBH_4$ with the AgNPs/**SugPOP-1** composite as catalyst. By the Beer–Lambert law we find that c_t/c_0 is proportional to A_t/A_0. A_t/A_0 was calculated via the corresponding absorbance ratio of the absorption at 400 nm. There is obviously a linear relationship consistent with the pseudo-first-order kinetics between $\ln(c_t/c_0)$ and reaction time (t). The rate constant k of the reaction in the presences of the AgNPs/**SugPOP-1** composite was 0.307 min^{-1} (5.14×10^{-3} s^{-1}) derived from the slope of the curve in Figure 5b. The active factor k_a ($k_a = k/m$, m is the total mass of catalyst) is considered as a suitable way to judge the activity of the catalyst [49]. As reported, the k_a of AgNPs/C composite is 1.69 s^{-1} g^{-1} [50], the Fe_3O_4@SiO_2–Ag nanocomposite is 7.76 s^{-1} g^{-1} [51], and the Ag/N–RGO is 7.4 s^{-1} g^{-1} [52]. These are all lower than the value of 51.4 s^{-1} g^{-1} found for the AgNPs/**SugPOP-1** composite prepared in this work. The high catalytic activity is due to the in situ synthesis of AgNPs well-dispersed in the porous polymer support with high SSA, producing more potential catalytic sites, which can promote the interaction between AgNPs and 4-NP to achieve a good catalytic effect.

The catalytic properties of composite materials are closely related to the content and particle size of the AgNPs. If the loading reaction time is short, the content of AgNPs incorporated into the porous polymer is too low and the AgNPs/**SugPOP-1** composite does not exhibit good catalytic activity. Composites with different metal particle sizes will exhibit different catalytic activity. Owing to the smaller particles, possessing more surface atoms available for catalysis, the related catalytic activity of the composite tends to decrease with the increase in the size of the AgNPs. Therefore, the reaction time should not be too long. We found that the optimized loading reaction time was about 24 h.

In the presence of excess BH_4^-, the catalytic reduction reaction mediated by the AgNPs/**SugPOP-1** composite could be assumed to follow the monomolecular mechanism [53]. During the reduction process, the interaction between 4-NP and catalytic sites of the AgNPs/**SugPOP-1** composite tend to form adsorbed species and the adsorption behavior to the formation of adsorbed species is described as the Langmuir–Freundlich isotherm [47]. The polymer matrix has higher adsorption capacity for 4-NP due to π–π stacking interactions, which can encourage 4-NP molecules to enter the polymer channel to form the adsorbed species [54]. At the same time, the hydrogen atom is introduced onto the surface of the AgNPs to form Ag–H via BH_4^- reacting with H_2O. Then, the adsorbed species containing 4-NP react with Ag–H to produce 4-AP [55]. The AgNPs play the role of electron-relaying matter to overcome the kinetic barrier in order to transfer electrons from BH_4^- to 4-NP [56]. In particular, the porous polymers encapsulating AgNPs is thought to accelerate the formation of Ag–H and its reaction with 4-NP. The pore structure of the polymer provides a favorable channel for the entry of 4-NP and the dissociation of 4-AP. The AgNPs embedded in the porous polymer remain active and the activity remains unaltered during the whole process [18].

Conclusion

The preparation of hypercross-linked polymers based on perbenzylated monosugars by Friedel–Crafts reaction using FDA as an external cross-linker is reported. Considering that the features of the polyhydroxylated structures derived from the monosaccharides have an effect on the SSA and PSD of the prepared porous polymers, porosity tuning could be achieved with three monomers with different molecular structures. The obtained

polymers exhibit mainly microporous and mesoporous features with an SSA (BET) of about 1000 $m^2 g^{-1}$. As for one of the obtained porous polymers containing a hemiacetal glucose motif (**SugPOP-1**), AgNPs were smoothly embedded into the material by chemical reduction of freshly prepared Tollens' reagent, allowing in situ formation of AgNPs in the polymer matrix. With a high porosity and micro-/mesoporous features, the AgNP-loaded polymer composite, AgNPs/**SugPOP-1**, exhibited good catalytic activity in the reduction of 4-NP at room temperature with a high activity factor (51.4 $s^{-1} g^{-1}$). This reflects the high catalytic activity of AgNPs/**SugPOP-1** with micro-/mesoporous features and implies important applications of nitro compound precursors for the preparation of pharmaceuticals and agrochemicals.

Experimental

Synthesis of perbenzyl phenyl β-D-glucopyranoside (**Sug-2**)

Sodium hydride (60%, 0.43 g, 10.85 mmol) was added portionwise to a solution of phenyl β-D-glucopyranoside (93 mg, 0.36 mmol) in DMF (5.0 mL) over 40 min under nitrogen atmosphere in an ice bath. After being stirred at room temperature, benzyl bromide (0.4 mL, 3.37 mmol) was added to the mixture. The resulting mixture was stirred for 4 h at room temperature and then ice water was added to quench the reaction. The suspension was extracted with ethyl acetate (2 × 50 mL). The combined organic layer was washed with water (3 × 50 mL) and dried with anhydrous sodium sulfate. After removing the solvent under reduced pressure, the residue was chromatographed on silica gel to give **Sug-2** as a white solid (149 mg, 67%). ^{1}H NMR (400 MHz, $CDCl_3$) δ (ppm) 7.31 (s, 20H), 7.20 (s, 2H), 7.13–6.97 (m, 3H), 5.12–4.90 (m, 3H), 4.84 (t, J = 11.1 Hz, 3H), 4.65–4.48 (m, 3H), 3.73 (m, 6H); ^{13}C NMR (100 MHz, $CDCl_3$) δ (ppm) 157.4, 138.6, 138.3, 138.2, 138.1, 129.6, 128.5, 128.4, 128.3, 128.0, 127.9, 127.8, 127.7, 127.6, 122.7, 116.9, 101.7, 84.7, 82.1, 77.8, 75.8, 75.2, 75.1, 73.5, 68.9; MS (MALDI–TOF) m/z: [M + Na] calcd for $C_{40}H_{40}O_6$, 639.3; found: 639.4.

Synthesis of perbenzyl methyl α-L-rhamnopyranoside (**Sug-3**)

Sodium hydride (160 mg, 60%, 6.72 mmol) was added to a solution of methyl α-L-rhamnopyranoside (200 mg, 1.12 mmol) in DMF (5.0 mL) in an ice bath over 40 min under a nitrogen atmosphere. Then benzyl bromide (470 μL, 3.93 mmol) was added and the reaction mixture was stirred at room temperature for 4 h. After completion (TLC and carbonation), the organic layer was extracted twice with ethyl acetate (50 mL). The combined organic layer was washed three times with water and dried with anhydrous sodium sulfate. The solvent was removed under reduced pressure and the residue was purified by silica gel column chromatography to give a colorless solid foam (286 mg, 57%). ^{1}H NMR (400 MHz, $CDCl_3$) δ (ppm) 7.38–7.19 (m, 15H), 4.92 (d, J = 10.9 Hz, 1H), 4.71 (q, J = 12.7 Hz, 2H), 4.66–4.52 (m, 4H), 3.87–3.70 (m, 2H), 3.61 (dd, J = 18.9, 9.9 Hz, 2H), 3.26 (s, 3H), 1.38–1.26 (m, 3H); ^{13}C NMR (100 MHz, $CDCl_3$) δ (ppm) 138.8, 138.7, 138.5, 128.5, 128.1, 128.0, 127.8, 127.7, 127.6, 99.2, 80.6, 80.3, 75.5, 74.9, 72.9, 72.2, 68.0, 54.7, 18.1; MS (MALDI–TOF) m/z: [M + Na] calcd for $C_{28}H_{32}O_5$, 471.2; found: 471.2.

Synthesis of polymers **SugPOP-1–3**

The representative synthesis procedure was as follows (**SugPOP-1**). Anhydrous $FeCl_3$ (180 mg, 1.11 mmol) was added to a stirred solution of **Sug-1** (100 mg, 0.18 mmol) and FDA (99 μL, 1.11 mmol) in 10 mL dry DCE under a nitrogen atmosphere. After the solution was well mixed, the resulting mixture was heated to 45 °C for 5 h and 85 °C for 19 h. The obtained precipitate was washed three times with methanol and THF, respectively. The residue was further purified by Soxhlet extraction with methanol and THF for 24 h each, then dried under reduced pressure at 50 °C for 24 h to give **Sug-1** as a brown powder (96 mg, 89%).

Following the same procedure as described for **SugPOP-1**, **SugPOP-2**, and **SugPOP-3** were prepared from **Sug-2** and **Sug-3**, respectively, with yields of about 90%.

Preparation of AgNPs/**SugPOP-1** composite

SugPOP-1 (101 mg) was added to a freshly prepared Tollens' reagent solution (15 mL). The reaction mixture was stirred at 45 °C in the dark for 24 h. The obtained product was filtered and washed with water and ethanol and then dried under reduced pressure at 45 °C for 24 h to give AgNPs/**SugPOP-1** composite as a brown solid (100 mg).

Catalytic reduction of 4-nitrophenol (4-NP) by AgNPs/**SugPOP-1** composite

To investigate the catalytic performance of the AgNPs/**SugPOP-1** composite, the reduction of 4-NP was performed in a quartz cuvette (1 cm optical path, 4 mL volume) in the presence of sodium borohydride ($NaBH_4$). 4-NP (1.44 mM, 0.10 mL) and a freshly prepared aqueous $NaBH_4$ solution (6.87 mM, 2.80 mL) were added in the quartz cuvette. Then, the AgNPs/**SugPOP-1** composite (1.0 mg/mL, 0.10 mL) suspended in deionized water was subsequently added to the above solution and the reaction progress monitored by UV–vis spectroscopy. The absorption spectra were measured at room temperature by recording absorbance from 244–600 nm within defined time intervals. The reduction reaction was conducted within minutes after the solution was prepared to minimize decomposition of $NaBH_4$.

Supporting Information

Supporting Information File 1

Additional spectra.
IR spectra of the **SugPOP-1–3**; ^{13}C CP/MAS NMR spectra of **SugPOP-1** and **SugPOP-2**; TGA curves of polymers **SugPOP-1–3** under nitrogen atmosphere; CO_2 adsorption isotherms of **SugPOP-1–3** with pressure up to 1.13 bar; X-ray diffraction patterns of **SugPOP-1** and AgNPs/**SugPOP-1** composite; TGA plot of the AgNPs/**SugPOP-1** composite under air atmosphere; ^1H NMR, ^{13}C NMR, and MS spectra of new monomers are provided.
[http://www.beilstein-journals.org/bjoc/content/supplementary/1860-5397-13-120-S1.pdf]

Acknowledgements

The financial support of the National Natural Science Foundation of China (Grants 21574031, 21374024, and 21574032), the Ministry of Science and Technology of China (Grant No. 2014CB932200), and CAS Youth Innovation Promotion Association is acknowledged.

References

1. Sidorov, S. N.; Bronstein, L. M.; Davankov, V. A.; Tsyurupa, M. P.; Solodovnikov, S. P.; Valetsky, P. M.; Wilder, E. A.; Spontak, R. J. *Chem. Mater.* **1999,** *11,* 3210–3215. doi:10.1021/cm990274p
2. Pan, L.; Chen, Q.; Zhu, J.-H.; Yu, J.-G.; He, Y.-J.; Han, B.-H. *Polym. Chem.* **2015,** *6,* 2478–2487. doi:10.1039/c4py01797h
3. Seo, M.; Kim, S.; Oh, J.; Kim, S.-J.; Hillmyer, M. A. *J. Am. Chem. Soc.* **2015,** *137,* 600–603. doi:10.1021/ja511581w
4. Luo, Y.; Li, B.; Wang, W.; Wu, K.; Tan, B. *Adv. Mater.* **2012,** *24,* 5703–5707. doi:10.1002/adma.201202447
5. Wood, C. D.; Tan, B.; Trewin, A.; Niu, H.; Bradshaw, D.; Rosseinsky, M. J.; Khimyak, Y. Z.; Campbell, N. L.; Kirk, R.; Stöckel, E.; Cooper, A. I. *Chem. Mater.* **2007,** *19,* 2034–2048. doi:10.1021/cm070356a
6. Li, B.; Gong, R.; Wang, W.; Huang, X.; Zhang, W.; Li, H.; Hu, C.; Tan, B. *Macromolecules* **2011,** *44,* 2410–2414. doi:10.1021/ma200630s
7. Yang, Y.; Zhang, Q.; Zhang, S.; Li, S. *Polymer* **2013,** *54,* 5698–5702. doi:10.1016/j.polymer.2013.08.039
8. Li, Z.; Wu, D.; Liang, Y.; Fu, R.; Matyjaszewski, K. *J. Am. Chem. Soc.* **2014,** *136,* 4805–4808. doi:10.1021/ja412192v
9. Grzybowski, M.; Skonieczny, K.; Butenschön, H.; Gryko, D. T. *Angew. Chem., Int. Ed.* **2013,** *52,* 9900–9930. doi:10.1002/anie.201210238
10. Li, B.; Guan, Z.; Yang, X.; Wang, W. D.; Wang, W.; Hussain, I.; Song, K.; Tan, B.; Li, T. *J. Mater. Chem. A* **2014,** *2,* 11930–11939. doi:10.1039/c4ta01081g
11. Zhu, J.-H.; Chen, Q.; Sui, Z.-Y.; Pan, L.; Yu, J.; Han, B.-H. *J. Mater. Chem. A* **2014,** *2,* 16181–16189. doi:10.1039/c4ta01537a
12. Woodward, R. T.; Stevens, L. A.; Dawson, R.; Vijayaraghavan, M.; Hasell, T.; Silverwood, I. P.; Ewing, A. V.; Ratvijitvech, T.; Exley, J. D.; Chong, S. Y.; Blanc, F.; Adams, D. J.; Kazarian, S. G.; Snape, C. E.; Drage, T. C.; Cooper, A. I. *J. Am. Chem. Soc.* **2014,** *136,* 9028–9035. doi:10.1021/ja5031968
13. Saleh, M.; Lee, H. M.; Kemp, K. C.; Kim, K. S. *ACS Appl. Mater. Interfaces* **2014,** *6,* 7325–7333. doi:10.1021/am500728q
14. Wang, S.; Tan, L.; Zhang, C.; Hussain, I.; Tan, B. *J. Mater. Chem. A* **2015,** *3,* 6542–6548. doi:10.1039/c4ta06963c
15. Sulman, E.; Doluda, V.; Dzwigaj, S.; Marceau, E.; Kustov, L.; Tkachenko, O.; Bykov, A.; Matveeva, V.; Sulman, M.; Lakina, N. *J. Mol. Catal. A: Chem.* **2007,** *278,* 112–119. doi:10.1016/j.molcata.2007.08.029
16. Ruan, Y.-L.; Jin, Y.; Yang, Y.-J.; Li, G.-J.; Boyer, J. S. *Mol. Plant* **2010,** *3,* 942–955. doi:10.1093/mp/ssq044
17. Li, H.; Meng, B.; Mahurin, S. M.; Chai, S.-H.; Nelson, K. M.; Baker, D. C.; Liu, H.; Dai, S. *J. Mater. Chem. A* **2015,** *3,* 20913–20918. doi:10.1039/c5ta03213j
18. Pradhan, N.; Pal, A.; Pal, T. *Colloids Surf., A* **2002,** *196,* 247–257. doi:10.1016/s0927-7757(01)01040-8
19. Chen, X.; Schluesener, H. J. *Toxicol. Lett.* **2008,** *176,* 1–12. doi:10.1016/j.toxlet.2007.10.004
20. Zhu, Y.; Morisato, K.; Li, W.; Kanamori, K.; Nakanishi, K. *ACS Appl. Mater. Interfaces* **2013,** *5,* 2118–2125. doi:10.1021/am303163s
21. Nie, S.; Emory, S. R. *Science* **1997,** *275,* 1102–1106. doi:10.1126/science.275.5303.1102
22. Ji, T.; Chen, L.; Mu, L.; Yuan, R.; Wang, H.; Knoblauch, M.; Bao, F. S.; Zhu, J. *Catal. Commun.* **2016,** *77,* 65–69. doi:10.1016/j.catcom.2016.01.025
23. Sárkány, A.; Sajó, I.; Hargittai, P.; Papp, Z.; Tombácz, E. *Appl. Catal., A* **2005,** *293,* 41–48. doi:10.1016/j.apcata.2005.06.030
24. Bois, L.; Chassagneux, F.; Battie, Y.; Bessueille, F.; Mollet, L.; Parola, S.; Destouches, N.; Toulhoat, N.; Moncoffre, N. *Langmuir* **2010,** *26,* 1199–1206. doi:10.1021/la902339j
25. Esteban-Cubillo, A.; Díaz, C.; Fernández, A.; Díaz, L. A.; Pecharromán, C.; Torrecillas, R.; Moya, J. S. *J. Eur. Ceram. Soc.* **2006,** *26,* 1–7. doi:10.1016/j.jeurceramsoc.2004.10.029
26. Katiyar, S.; Mondal, K.; Sharma, A. *RSC Adv.* **2016,** *6,* 12298–12310. doi:10.1039/c5ra26503g
27. Vijayakumar, P. S.; Prasad, B. L. V. *Langmuir* **2009,** *25,* 11741–11747. doi:10.1021/la901024p
28. Laudenslager, M. J.; Schiffman, J. D.; Schauer, C. L. *Biomacromolecules* **2008,** *9,* 2682–2685. doi:10.1021/bm800835e
29. Nagy, A.; Harrison, A.; Sabbani, S.; Munson, R. S., Jr.; Dutta, P. K.; Waldman, W. J. *Int. J. Nanomed.* **2011,** *6,* 1833–1852. doi:10.2147/ijn.s24019
30. Wu, J.; Zhao, N.; Zhang, X.; Xu, J. *Cellulose* **2012,** *19,* 1239–1249. doi:10.1007/s10570-012-9731-3
31. Koga, H.; Kitaoka, T.; Wariishi, H. *J. Mater. Chem.* **2009,** *19,* 2135–2140. doi:10.1039/b820310e
32. Vora, K.; Kang, S. Y.; Shukla, S.; Mazur, E. *Appl. Phys. Lett.* **2012,** *100,* 063120. doi:10.1063/1.3684277
33. Pore, S.; Venkatram, N.; Rao, D. N.; Radhakrishnan, T. P. *J. Appl. Phys.* **2007,** *102,* 033107. doi:10.1063/1.2764239
34. Thanjam, I. S.; Philips, M. F.; Lee, K.-P.; Gopalan, A. *J. Mater. Sci.: Mater. Electron.* **2012,** *23,* 807–810. doi:10.1007/s10854-011-0496-5

35. Cao, Q.; Chen, Q.; Han, B. *Acta Chim. Sin.* **2015,** *73,* 541–556. doi:10.6023/a15020126
36. Taskin, O. S.; Dadashi-Silab, S.; Kiskan, B.; Weber, J.; Yagci, Y. *Macromol. Chem. Phys.* **2015,** *216,* 1746–1753. doi:10.1002/macp.201500141
37. Liu, J.; Chen, Q.; Sun, Y.-N.; Xu, M.-Y.; Liu, W.; Han, B.-H. *RSC Adv.* **2016,** *6,* 48543–48549. doi:10.1039/c6ra04515d
38. Zhong, H.; Liu, C.; Wang, Y.; Wang, R.; Hong, M. *Chem. Sci.* **2016,** *7,* 2188–2194. doi:10.1039/c5sc04351d
39. Ishida, T.; Onuma, Y.; Kinjo, K.; Hamasaki, A.; Ohashi, H.; Honma, T.; Akita, T.; Yokoyama, T.; Tokunaga, M.; Haruta, M. *Tetrahedron* **2014,** *70,* 6150–6155. doi:10.1016/j.tet.2014.04.049
40. Liu, J.; Cui, J.; Vilela, F.; He, J.; Zeller, M.; Hunter, A. D.; Xu, Z. *Chem. Commun.* **2015,** *51,* 12197–12200. doi:10.1039/c5cc04476f
41. Saha, S.; Pal, A.; Kundu, S.; Basu, S.; Pal, T. *Langmuir* **2010,** *26,* 2885–2893. doi:10.1021/la902950x
42. Zhang, Z.; Shao, C.; Zou, P.; Zhang, P.; Zhang, M.; Mu, J.; Guo, Z.; Li, X.; Wang, C.; Liu, Y. *Chem. Commun.* **2011,** *47,* 3906–3908. doi:10.1039/c0cc05693f
43. Liang, M.; Su, R.; Huang, R.; Qi, W.; Yu, Y.; Wang, L.; He, Z. *ACS Appl. Mater. Interfaces* **2014,** *6,* 4638–4649. doi:10.1021/am500665p
44. Liang, M.; Wang, L.; Liu, X.; Qi, W.; Su, R.; Huang, R.; Yu, Y.; He, Z. *Nanotechnology* **2013,** *24,* 245601. doi:10.1088/0957-4484/24/24/245601
45. Zhang, P.; Shao, C.; Zhang, Z.; Zhang, M.; Mu, J.; Guo, Z.; Liu, Y. *Nanoscale* **2011,** *3,* 3357–3363. doi:10.1039/c1nr10405e
46. Dauthal, P.; Mukhopadhyay, M. *Ind. Eng. Chem. Res.* **2012,** *51,* 13014–13020. doi:10.1021/ie300369g
47. Wunder, S.; Polzer, F.; Lu, Y.; Mei, Y.; Ballauff, M. *J. Phys. Chem. C* **2010,** *114,* 8814–8820. doi:10.1021/jp101125j
48. Schrinner, M.; Ballauff, M.; Talmon, Y.; Kauffmann, Y.; Thun, J.; Möller, M.; Breu, J. *Science* **2009,** *323,* 617–620. doi:10.1126/science.1166703
49. Baruah, B.; Gabriel, G. J.; Akbashev, M. J.; Booher, M. E. *Langmuir* **2013,** *29,* 4225–4234. doi:10.1021/la305068p
50. Tang, S.; Vongehr, S.; Meng, X. *J. Phys. Chem. C* **2010,** *114,* 977–982. doi:10.1021/jp9102492
51. Chi, Y.; Yuan, Q.; Li, Y.; Tu, J.; Zhao, L.; Li, N.; Li, X. *J. Colloid Interface Sci.* **2012,** *383,* 96–102. doi:10.1016/j.jcis.2012.06.027
52. Tian, Y.; Cao, Y.-y.; Pang, F.; Chen, G.-q.; Zhang, X. *RSC Adv.* **2014,** *4,* 43204–43211. doi:10.1039/c4ra06089j
53. Li, M.; Chen, G. *Nanoscale* **2013,** *5,* 11919–11927. doi:10.1039/c3nr03521b
54. Daniel, M.-C.; Astruc, D. *Chem. Rev.* **2004,** *104,* 293–346. doi:10.1021/cr030698+
55. Holbrook, K. A.; Twist, P. J. *J. Chem. Soc. A* **1971,** 890–894. doi:10.1039/j19710000890
56. Chen, H. M.; Chen, C. K.; Chen, C.-J.; Cheng, L.-C.; Wu, P. C.; Cheng, B. H.; Ho, Y. Z.; Tseng, M. L.; Hsu, Y.-Y.; Chan, T.-S.; Lee, J.-F.; Liu, R.-S.; Tsai, D. P. *ACS Nano* **2012,** *6,* 7362–7372. doi:10.1021/nn3024877

License and Terms

BEILSTEIN JOURNAL OF ORGANIC CHEMISTRY

Novel approach to hydroxy-group-containing porous organic polymers from bisphenol A

Tao Wang[1,2], Yan-Chao Zhao[1], Li-Min Zhang[1], Yi Cui[1], Chang-Shan Zhang[2] and Bao-Hang Han[*1]

Full Research Paper

Open Access

Address:
[1]CAS Key Laboratory of Nanosystem and Hierarchical Fabrication, CAS Center for Excellence in Nanoscience, National Center for Nanoscience and Technology, Beijing 100190, China and [2]School of Chemical Engineering, Nanjing University of Science and Technology, Nanjing 210094, China

Email:
Bao-Hang Han[*] - hanbh@nanoctr.cn

* Corresponding author

Keywords:
bisphenol A; carbon dioxide uptake; hydrogen storage; OH-containing; porous organic polymers

Beilstein J. Org. Chem. **2017,** *13,* 2131–2137.
doi:10.3762/bjoc.13.211

Received: 25 January 2017
Accepted: 20 September 2017
Published: 12 October 2017

This article is part of the Thematic Series "Organic porous materials".

Guest Editor: S. Bräse

Abstract

We successfully employed bisphenol A and several different formyl-containing monomers as useful building blocks to construct a series of hydroxy-group-containing porous organic polymers in a sealed tube at high temperature. Fourier transform infrared and solid-state ^{13}C CP/MAS NMR spectroscopy are utilized to characterize the possible structure of the obtained polymers. The highest Brunauer–Emmet–Teller specific surface area of the phenolic-resin porous organic polymers (PPOPs) is estimated to be 920 m^2 g^{-1}. The PPOPs exhibit a highest carbon dioxide uptake (up to 15.0 wt % (273 K) and 8.8 wt % (298 K) at 1.0 bar), and possess moderate hydrogen storage capacities ranging from 1.28 to 1.04 wt % (77 K) at 1.0 bar. Moreover, the highest uptake of methane for the PPOPs is measured as 4.3 wt % (273 K) at 1.0 bar.

Introduction

Porous organic polymers standing out from kinds of porous materials such as zeolite, activated carbon, metal-organic frameworks [1,2], and covalent organic frameworks [3,4], with their prominent potential as heterogeneous catalysts [5-7], supports for catalysts [8,9], gas permeable membranes [10,11], and gas storage materials [12-14] have attracted much attentions from researchers all over the world as reviewed by Matyjaszewski [15]. During the past years, a large amount of porous organic polymers (POPs) have been reported via Sonogashira–Hagihara coupling reaction [16], Suzuki–Miyaura chemistry [17], Yamato reaction [18], and self condensation of aromatic nitriles[19]. Although these methods can be used to construct POPs with high specific surface area values, these reactions are usually catalyzed by heavy and/or transition-metal catalysts,

which are usually expensive and environmentally harmful. Furthermore, the majority of reagents used for the preparation of the aforementioned POPs are synthesized through multiple steps at high cost. New reactions using inexpensive and convenient raw materials with non-metallic catalysts, even no catalysts might show great advantages for construction of porous organic polymers. Our group has made much contribution to the exploitation of such reaction methodologies without any metallic catalysts [20-22].

We found that Bakelite-type chemistry is a reaction that can be catalyzed without any metal-containing catalysts and it is selected as an appropriate approach, spontaneously. Phenolic resins can be produced commercially using bases (ammonia and sodium hydroxide) or acids (hydrochloric acid and sulfuric acid) as catalysts via connecting phenolic molecules with formaldehyde or other aromatic aldehydes to form cross-linking structures through the simple Bakelite-type chemistry to obtain great number of polymers with different functionalities. Phloroglucinol has been utilized as a monomer by Kanatzidis and Katsoulidis [23,24] to produce a series of porous polymers. In this contribution, bisphenol A (BPA) was employed as a novel polyphenol monomer instead of phloroglucinol. BPA is a commercially available industrial raw material, which is much cheaper than phloroglucinol. In addition, BPA might be stored more easily, compared with phloroglucinol that has a relatively high reactivity and can be oxidized in an ambient environment. Based on the aforementioned, BPA, to the best of our knowledge, may be a suitable candidate prior to other phenolic compounds such as phloroglucinol [23] and 1,5-dihydroxynaphthalene [24], which have been used for the preparation of porous materials.

Recently, Kanatzidis and Katsoulidis have reported a series of Bakelite-type porous organic polymers prepared in two steps. The mixture of reagents and solvent was pretreated at 70 °C and kept for 1 h, followed by a high temperature treatment at 220 °C for 96 h [25]. This approach is involved with a longer reaction time and a higher reaction temperature, which might cause a tremendous energy waste. Herein we provide an effective one-step approach to construct phenolic-resin porous organic polymers (PPOPs) from the reactions between BPA and different aldehydes using *p*-toluenesulfonic acid (TSA) as catalyst that has been proved to be a non-metallic acidic catalyst with high efficiency [26,27]. The materials exhibit Brunauer–Emmet–Teller (BET) specific surface area values ranging from 720 to 920 m^2 g^{-1}, and the highest carbon dioxide uptake is up to 15.0 wt % at 273 K and 1.0 bar. Meanwhile, the hydrogen and methane capacities are also investigated. Considering the gas adsorption properties, PPOPs may be a promising candidate for gas storage and separation materials.

Results and Discussion

Three multi-formyl compounds, i.e., two dialdehydes **M1** and **M2** [22] and one trialdehyde **M3** [22] were employed to react with bisphenol A to produce phenolic-resin porous polymers **PPOP-1**–**PPOP-3** (Scheme 1). It is well-known that the *ortho*- and *para*-position of phenol are activated with negative charge

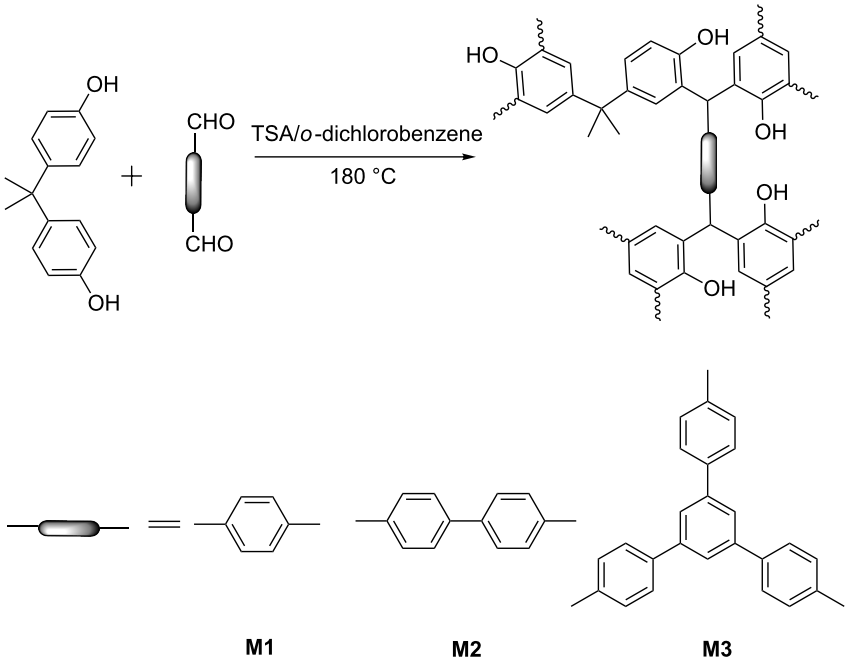

Scheme 1: Schematic representation of the possible structures of bisphenol-A-based porous organic polymers.

for the electrophilic aromatic substitution in consequence of the electron-donating effect of the hydroxy group. The positively charged carbonyl group of the aldehyde could be attacked by the electron-rich phenyl ring, thus a carbonyl group can connect two phenol molecules by elimination of a water molecule. As a result, a cross-linked hydroxy-group-containing polymer is constructed ultimately. BPA and multi-formyl-containing compounds are suspended in *o*-dichlorobenzene, and TSA, as a catalyst, was then added into reaction system. After the reaction in a sealed tube at 180 °C for 72 h, three polymers **PPOP-1**–**PPOP-3** were obtained. The possible chemical structures of the obtained PPOPs are shown in the Scheme 1. All of the polymers are stable and insoluble in common organic solvents such as dichloromethane, ethanol, and acetone. Furthermore, the as-prepared materials exhibit a high thermal stability according to the results of TGA (Supporting Information File 1, Figure S1). There is a weight loss of about 5% up to 150 °C, which is attributed to the evaporation of trapped solvent, carbon dioxide, or adsorbed water that could not be easily removed from the microporous structure of the polymers during the after-synthesis treatment and drying process. There is not any obvious thermal degradation for PPOPs until when heated up to 300 °C.

According to the TGA result of BPA (Supporting Information File 1, Figure S2), the thermal degradation of BPA begins around 180 °C and the evolved products are mainly phenol with one or two benzene rings from investigations of thermal degradation of bisphenol A polycarbonate [28]. Investigation of the changes from methyl groups and aldehyde groups between monomers and polymers is carried out by means of FTIR spectroscopy. The FTIR spectra displayed (Figure 1 and Supporting Information File 1, Figure S3) that signal at 2970 cm^{-1} arised from the stretching vibration of methyl groups shows quantitative changes between BPA and PPOPs, suggesting the degradation of BPA in *o*-dichlorobenzene and it is reported that the cleavage of methylene can be catalyzed under acidic or basic conditions [29,30]. *p*-Toluenesulfonic acid acted as an acid catalyst in this contribution and will promote the cleavage of BPA at high temperature. The broad absorption bands located at ca. 3500 cm^{-1} is attributed to the characteristic stretching vibration of hydroxy groups, which is consistent with the literature data [25]. The absorption peak at 1705 cm^{-1} assigned to the stretching vibration of carbonyl groups is significantly reduced in PPOPs, indicating that most of the aldehyde compounds are consumed.

Solid-state ^{13}C CP/MAS NMR spectroscopy was employed to characterize the structure of the polymers PPOPs. As shown in Figure 2 and Figure S4 (Supporting Information File 1), it can be found that the ^{13}C chemical shifts of these polymers are similar. It is reasonable considering the structural features of these polymers. Typically, taking the spectrum of **PPOP-1** for example, two major resonances at 127 and 140 ppm are assigned to the unsubstituted phenyl carbon atoms and the substituted aromatic carbon atoms, respectively. The resonance at 46 ppm can be ascribed to the tertiary carbon atoms that act as the linkage of two different benzene rings originated from the BPA and aldehyde monomers, respectively. The shoulder peak at 116 ppm is related to the reacted *ortho* carbons of the hydroxy groups. The signal at 153 ppm comes from the phenoxy carbons [25]. Unexpectedly, no obvious peak at 20 ppm ascribed to the carbons of methyl groups from BPA molecules can be found in the spectrum of **PPOP-1**, which is in consistence with the results of FT-IR spectra, indicating the degradation of BPA catalyzed by TSA at high temperature [29,30].

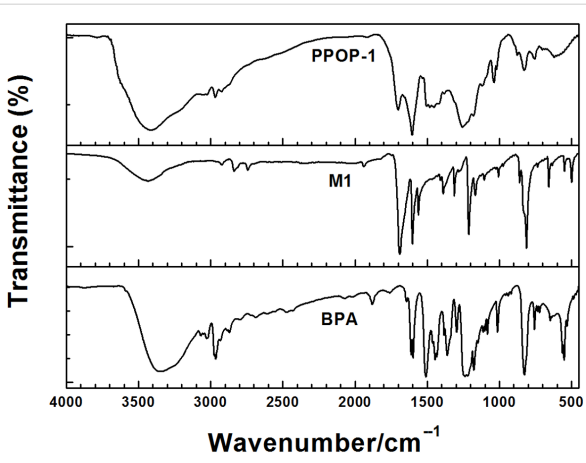

Figure 1: FTIR spectra of terephthalic aldehyde (**M1**), BPA, and **PPOP-1**.

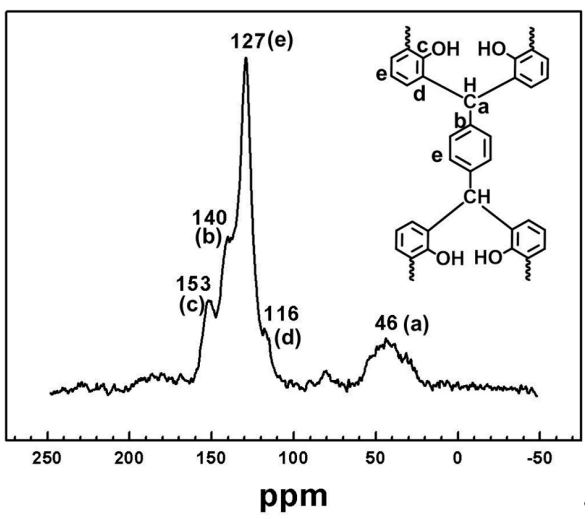

Figure 2: Solid-state ^{13}C CP/MAS NMR spectrum of **PPOP-1** recorded at the MAS rate of 5 kHz.

Nitrogen sorption measurements were employed to evaluate the porosity of the obtained polymers. The nitrogen adsorption–desorption isotherms of **PPOP-1**–**PPOP-3** are similar to each other (Figure 3a). All of the isotherms show a high gas uptake at relative pressure (P/P_0) less than 0.02, indicating that the materials are microporous. Meanwhile, a nitrogen condensation step could be found for all the polymers at P/P_0 above 0.90, which is an indication of characteristic macroporosity that might correspond to interparticular voids associated with the pack of small particles of about 4 μm adhered to the external surface of spherical particles (Supporting Information File 1, Figure S5). The BET specific surface area values are calculated in the relative pressure range P/P_0 = 0.01–0.10 for the microporous materials [31] for PPOPs (Supporting Information File 1, Figure S6). **PPOP-2** possesses the highest BET surface area value calculated as 920 m^2 g^{-1}. According to the obtained values summarized in Table 1, both total pore volume (0.36 cm^3 g^{-1}) determined at P/P_0 = 0.95 and micropore volume (0.18 cm^3 g^{-1}) calculated using the *t*-plot method of **PPOP-1** are smaller than those of **PPOP-2** and **PPOP-3**. The difference between the pore volumes and BET specific surface area results of PPOPs may be related to the monomer strut length. With the shortest linker of **M1**, **PPOP-1** possesses the lowest pore volume and BET specific surface area. As for **PPOP-3**, using **M3** as a monomer may induce a depression of polymerization degree owing to its stereo-hindrance effect, which might be responsible for its lower BET surface area value (880 m^2 g^{-1}) and micropore volume (0.20 cm^3 g^{-1}) than that of **PPOP-2** using **M2** as the monomer. However, it is noteworthy that when the reaction is conducted between **M1** and phenol selected as the substitution of BPA, a new material is obtained with a BET surface area value calculated as 470 m^2 g^{-1} (Supporting Information File 1, Figure S7), which is a indication of the fact that pyrolysis of BPA might result in some new porous structure in situ, leading to an increase in BET surface area value. The PSD profiles calculated using original DFT are shown in Figure 3b. All of the materials exhibit a similar PSD profile with a maximum peak at 0.59 nm and several smaller peaks between 0.6 and 2.0 nm, indicating that PPOPs are microporous. The pore size for PPOPs and the total pore volume for **PPOP-2** and **PPOP-3** do not show any obvious difference with increasing monomer strut length, which may be attributed to the random penetration and space-filling within the fragments of the extended repeating units [16].

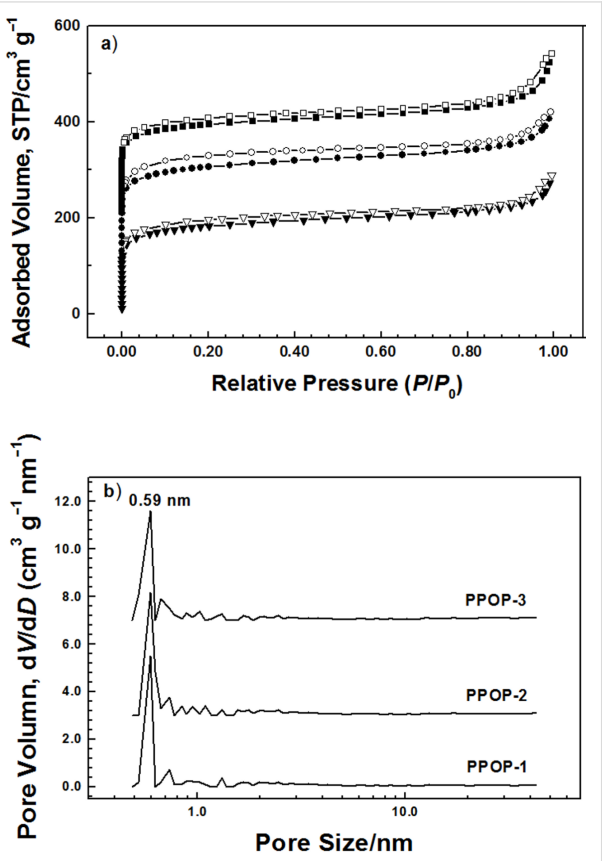

Figure 3: (a) Nitrogen adsorption–desorption isotherms of **PPOP-1** (downtriangle), **PPOP-2** (circle), and **PPOP-3** (square) at 77 K. The isotherms have been offset by 100 cm^3 g^{-1} for **PPOP-2** and 200 cm^3 g^{-1} for **PPOP-3** for the purpose of clarity, respectively. (b) PSD profiles calculated by the original DFT method. The PSD profiles of **PPOP-2** and **PPOP-3** have been offset by 3 and 6 units for the purpose of clarity, respectively.

The gas uptake capacities for carbon dioxide, hydrogen, and methane of the polymers are investigated by gravimetric methods and listed in Table 2. The hydrogen storage capacities for PPOPs vary between 1.08 and 1.28 wt % at 77 K and 1.0 bar (Figure 4a) and **PPOP-3** possesses the highest hydrogen uptake,

Table 1: Porosity properties of **PPOP-1**–**PPOP-3**.

polymer	S_{BET} (m^2 g^{-1})[a]	V_{total} (cm^3 g^{-1})[b]	V_{micro} (cm^3 g^{-1})[c]
PPOP-1	720	0.36	0.18
PPOP-2	920	0.41	0.21
PPOP-3	880	0.41	0.20

[a]Surface area calculated from the nitrogen adsorption isotherm using the BET method in the relative pressure (P/P_0) range from 0.01 to 0.10. [b]Total pore volume at P/P_0 = 0.95. [c]Micropore volume calculated from nitrogen adsorption isotherm using the *t*-plot method.

Table 2: Gas adsorption uptake of **PPOP-1**–**PPOP-3**.

polymer	H_2 uptake (wt %)[a]	CH_4 uptake (wt %)[b]	CO_2 uptake (wt %)[c]	
			273 K	298 K
PPOP-1	1.14	4.01	13.2	9.1
PPOP-2	1.08	4.29	14.6	8.2
PPOP-3	1.28	3.24	15.0	8.8

[a]Hydrogen gravimetric uptake capacities at 77 K measured at hydrogen equilibrium pressure of 1.0 bar. [b]Methane gravimetric uptake capacities at 273 K measured at a pressure at 1.0 bar. [c]Carbon dioxide gravimetric uptake capacities at 1.0 bar measured at 273 and 298 K, respectively.

which may be on account of the fact that there is much more ultramicropores in **PPOP-3** that are appropriate for hydrogen rather than nitrogen [32]. The methane gravimetric uptake for the materials was measured at 273 K and 1.0 bar. PPOPs exhibit a methane storage capacity varying between 4.29 and 3.24 wt % (Figure 4d), which is higher than that of the reported mesoporous polymeric organic frameworks (mesoPOF)s [23]. **PPOP-2** with the largest BET surface area and micropore volume shows the highest methane uptake. However, **PPOP-3** possesses a smaller methane storage capacity than **PPOP-1** that is known for its lowest BET surface area and total pore volume and micropore volume, which may arise from the fact that interactions between the accessible surface area, micropore volume, and pore topology contribute predominantly to methane storage capacity in porous material [33,34]. The carbon dioxide adsorption isotherms for PPOPs are collected at 273 and 298 K, respectively (Figure 4b,c). **PPOP-3** possesses a largest carbon dioxide adsorption capacity up to 15.0 wt % (273 K) and 8.8 wt % (298 K) at 1.0 bar, which is larger than that of the reported work [35]. As reported that apparent surface area is not the only crucial factor that influences the amount of adsorbed CO_2, whereas the uptake capacity is more depended on porosity characteristic such as pore size in the networks [36,37]. Specially, the smallest pores contribute most to the CO_2 uptake

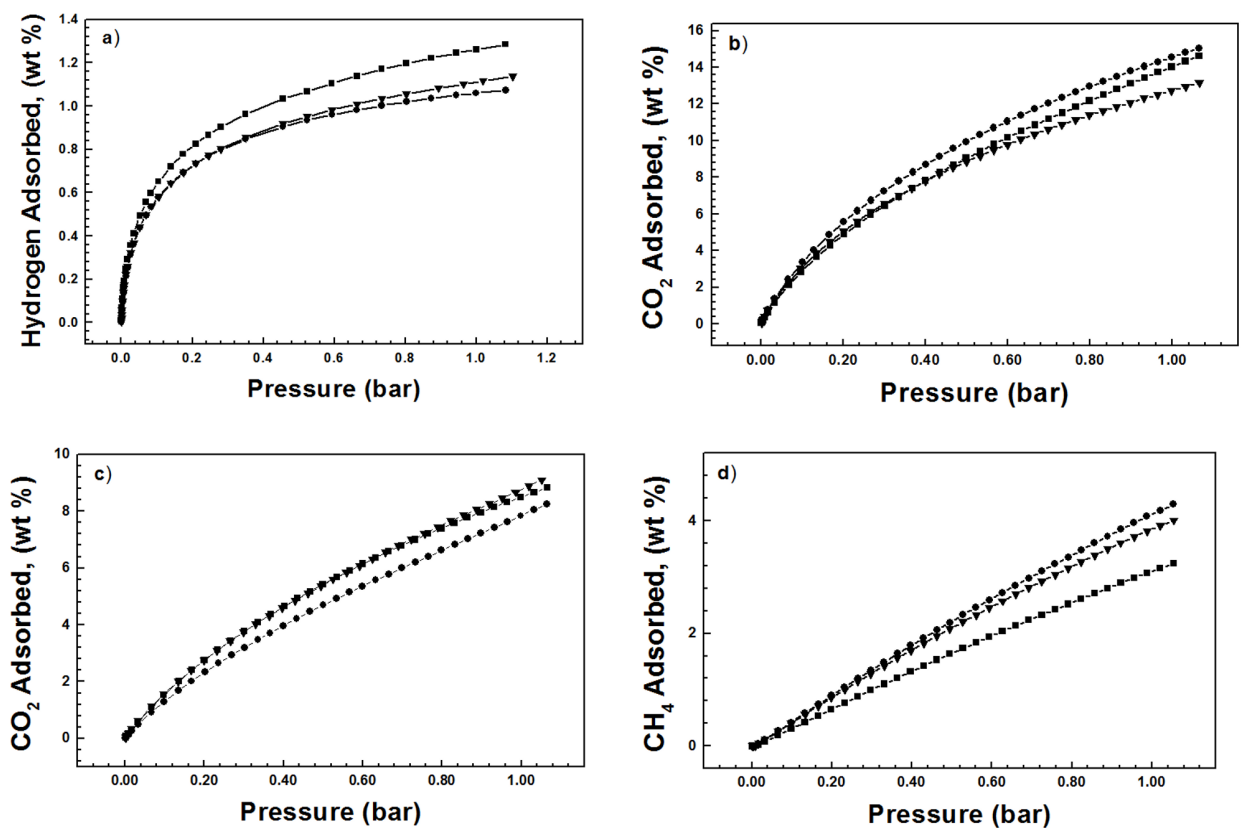

Figure 4: Gravimetric gas adsorption isotherms for **PPOP-1** (downtriangle), **PPOP-2** (circle), and **PPOP-3** (square) (a) hydrogen at 77 K, (b) carbon dioxide at 273 K, (c) carbon dioxide at 298 K, and (d) methane at 273 K.

at low pressure [36]. Hence, **PPOP-3** with a smaller pore size located at 0.68 nm that is different from the other two polymers in Figure 3b is probably the best candidate for CO_2 capture. The high carbon dioxide uptake capacity for PPOPs may correspond to the large amount of the hydroxy groups in the PPOPs through the formation of O=C=O(δ^-)…H(δ^+)–O hydrogen bonds that are enhanced by weak supramolecular interactions with C–H atoms on the aromatic rings of the polymers [38]. The isosteric heat of adsorption for carbon dioxide is calculated from adsorption data collected at 273 and 298 K using a virial method and the Clausius–Clapeyron equation [39] (Supporting Information File 1, Figure S8). The typical heats of absorption Q_{st} for the PPOPs are measured in the range of about 21.6–24.3 kJ mol^{-1} (Figure 5), which are in accordance with the report data [40], indicating that the adsorption of CO_2 is mainly physical adsorption. Unusually, **PPOP-2** and **PPOP-3** show an increase in the Q_{st} value with increased CO_2 loading, which is likely induced by synergic interactions between carbon dioxide molecules [41,42].

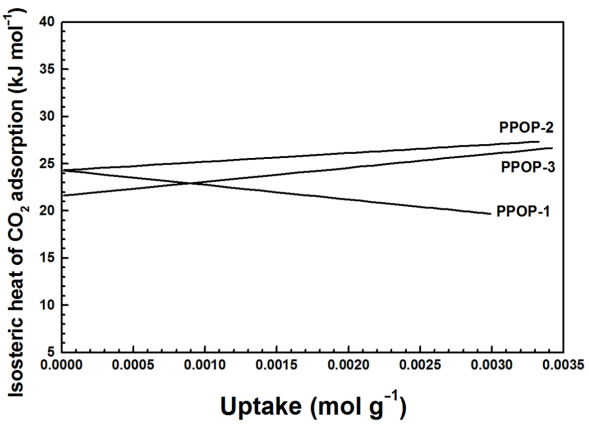

Figure 5: Variation of isosteric heat of adsorption with amount of adsorbed CO_2 in **PPOP-1**, **PPOP-2**, and **PPOP-3**.

Conclusion

In conclusion, we have developed a novel approach to porous organic polymers from BPA using the traditional Bakelite-type chemistry. The prepared polymers possess high specific surface area values up to 920 m^2 g^{-1}, with a high carbon dioxide uptake of up to 15.0 wt % at 273 K and 1.0 bar. The materials also exhibit hydrogen uptake properties measured as 1.28 wt % (77 K) at 1.0 bar while the highest methane storage capacity is 4.29 wt % (273 K) at 1.0 bar. These gas adsorption properties and high BET specific surface area may make the PPOPs appropriate candidates for materials for gas adsorption and storage.

Experimental

Preparation of PPOPs

A mixture of BPA (50.0 mg, 0.22 mmol), terephthalaldehyde (59.0 mg, 0.44 mmol), and *p*-toluenesulfonic acid (0.5 g) was suspended in *o*-dichlorobenzene (8.0 mL) in a glass tube. After ultrasonication for 0.5 h, the mixture was degassed by at least three freeze–pump–thaw cycles. The tube was frozen at 77 K (liquid nitrogen bath) and evacuated to high vacuum and flame-sealed. After 180 °C for 72 h, the reaction mixture gave a solid product (denoted as **PPOP-1**). After cooled to room temperature, the solid was filtrated and washed with acetone, dichloromethane, and ethanol, subsequently. Further purification of the polymer was carried out by Soxhlet extraction with water, ethanol, and dichloromethane for 24 h to give the final product with a yield of 87.5%, which was dried in vacuo at 120 °C for more than 12 h.

Similar to the preparation of **PPOP-1**, 4,4'-biphenyldicarboxaldehyde (**M2**) and 1,3,5-tri(4-formylphenyl)benzene (**M3**) were used to afford **PPOP-2** and **PPOP-3**, with yield of 85% and 80%, respectively.

Supporting Information

Supporting Information File 1

Experimental, instruments section, SEM images, data of TGA, FTIR and BET surface area, virial analysis of the adsorption data for CO_2 and NMR spectra.
[http://www.beilstein-journals.org/bjoc/content/supplementary/1860-5397-13-211-S1.pdf]

Acknowledgements

The financial support of the National Natural Science Foundation of China (Grant no. 21574032) and the Ministry of Science and Technology of China (Grant no. 2014CB932200) is acknowledged.

References

1. Yaghi, O. M.; Li, G.; Li, H. *Nature* **1995,** *378,* 703–706. doi:10.1038/378703a0
2. Yaghi, O. M.; Li, H. *J. Am. Chem. Soc.* **1995,** *117,* 10401–10402. doi:10.1021/ja00146a033
3. Côté, A. P.; Benin, A. I.; Ockwig, N. W.; O'Keeffe, M.; Matzger, A. J.; Yaghi, O. M. *Science* **2005,** *310,* 1166–1170. doi:10.1126/science.112041
4. Wan, S.; Guo, J.; Kim, J.; Ihee, H.; Jiang, D. *Angew. Chem., Int. Ed.* **2008,** *47,* 8826–8830. doi:10.1002/anie.200803826
5. Palkovits, R.; Antonietti, M.; Kuhn, P.; Thomas, A.; Schüth, F. *Angew. Chem., Int. Ed.* **2009,** *48,* 6909–6912. doi:10.1002/anie.200902009
6. Liu, J.; Chen, Q.; Sun, Y.-N.; Xu, M.-Y.; Liu, W.; Han, B.-H. *RSC Adv.* **2016,** *6,* 48543–48549. doi:10.1039/c6ra04515d

7. Du, X.; Sun, Y.; Tan, B.; Teng, Q.; Yao, X.; Su, C.; Wang, W. *Chem. Commun.* **2010,** *46,* 970–972. doi:10.1039/B920113K
8. Chan-Thaw, C. E.; Villa, A.; Katekomol, P.; Su, D.; Thomas, A.; Prati, L. *Nano Lett.* **2010,** *10,* 537–541. doi:10.1021/nl904082k
9. Kaur, P.; Hupp, J. T.; Nguyen, S. T. *ACS Catal.* **2011,** *1,* 819–835. doi:10.1021/cs200131g
10. Ghanem, B. S.; McKeown, N. B.; Budd, P. M.; Selbie, J. D.; Fritsch, D. *Adv. Mater.* **2008,** *20,* 2766–2771. doi:10.1002/adma.200702400
11. Du, N.; Park, H. B.; Robertson, G. P.; Dal-Cin, M. M.; Visser, T.; Scoles, L.; Guiver, M. D. *Nat. Mater.* **2011,** *10,* 372–375. doi:10.1038/nmat2989
12. Wood, C. D.; Tan, B.; Trewin, A.; Niu, H.; Bradshaw, D.; Rosseinsky, M. J.; Khimyak, Y. Z.; Campbell, N. L.; Kirk, R.; Stöckel, E.; Cooper, A. I. *Chem. Mater.* **2007,** *19,* 2034–2048. doi:10.1021/cm070356a
13. Hu, X.-M.; Chen, Q.; Zhao, Y.-C.; Laursen, B. W.; Han, B.-H. *Microporous Mesoporous Mater.* **2016,** *224,* 129–134. doi:10.1016/j.micromeso.2015.11.046
14. McKeown, N. B.; Gahnem, B.; Msayib, K. J.; Budd, P. M.; Tattershall, C. E.; Mahmood, K.; Tan, S.; Book, D.; Langmi, H. W.; Walton, A. *Angew. Chem., Int. Ed.* **2006,** *45,* 1804–1807. doi:10.1002/anie.200504241
15. Wu, D.; Xu, F.; Sun, B.; Fu, R.; He, H.; Matyjaszewski, K. *Chem. Rev.* **2012,** *112,* 3959–4015. doi:10.1021/cr200440z
16. Jiang, J.-X.; Su, F.; Trewin, A.; Wood, C. D.; Niu, H.; Jones, J. T. A.; Khimyak, Y. Z.; Cooper, A. I. *J. Am. Chem. Soc.* **2008,** *130,* 7710–7720. doi:10.1021/ja8010176
17. Weber, J.; Thomas, A. *J. Am. Chem. Soc.* **2008,** *130,* 6334–6335. doi:10.1021/ja801691x
18. Liu, X.; Xu, Y.; Jiang, D. *J. Am. Chem. Soc.* **2012,** *134,* 8738–8741. doi:10.1021/ja303448r
19. Kuhn, P.; Antonietti, M.; Thomas, A. *Angew. Chem., Int. Ed.* **2008,** *47,* 3450–3453. doi:10.1002/anie.200705710
20. Zhao, Y.-C.; Cheng, Q.-Y.; Zhou, D.; Wang, T.; Han, B.-H. *J. Mater. Chem.* **2012,** *22,* 11509–11514. doi:10.1039/C2JM31187A
21. Zhao, Y.-C.; Wang, T.; Zhang, L.-M.; Cui, Y.; Han, B.-H. *ACS Appl. Mater. Interfaces* **2012,** *4,* 6975–6981. doi:10.1021/am302163p
22. Wang, T.; Zhao, Y.-C.; Luo, M.; Zhang, L.-M.; Cui, Y.; Zhang, C.-S.; Han, B.-H. *Polymer* **2015,** *60,* 26–31. doi:10.1016/j.polymer.2014.12.072
23. Katsoulidis, A. P.; Kanatzidis, M. G. *Chem. Mater.* **2012,** *24,* 471–479. doi:10.1021/cm202578k
24. Katsoulidis, A. P.; He, J.; Kanatzidis, M. G. *Chem. Mater.* **2012,** *24,* 1937–1943. doi:10.1021/cm300696g
25. Katsoulidis, A. P.; Kanatzidis, M. G. *Chem. Mater.* **2011,** *23,* 1818–1824. doi:10.1021/cm103206x
26. Wisser, F. M.; Eckhardt, K.; Wisser, D.; Böhlmann, W.; Grothe, J.; Brunner, E.; Kaskel, S. *Macromolecules* **2014,** *47,* 4210–4216. doi:10.1021/ma500512j
27. Rose, M.; Klein, N.; Senkovska, I.; Schrage, C.; Wollmann, P.; Böhlmann, W.; Böhringer, B.; Fichtner, S.; Kaskel, S. *J. Mater. Chem.* **2011,** *21,* 711–716. doi:10.1039/C0JM02998J
28. Jang, B. N.; Wilkie, C. A. *Polym. Degrad. Stab.* **2004,** *86,* 419–430. doi:10.1016/j.polymdegradstab.2004.05.009
29. Hunter, S. E.; Felczak, C. A.; Savage, P. E. *Green Chem.* **2004,** *6,* 222–226. doi:10.1039/B313509H
30. Hunter, S. E.; Savage, P. E. *J. Org. Chem.* **2004,** *69,* 4724–4731. doi:10.1021/jo0356964
31. Dawson, R.; Laybourn, A.; Clowes, R.; Khimyak, Y. Z.; Adams, D. J.; Cooper, A. I. *Macromolecules* **2009,** *42,* 8809–8816. doi:10.1021/ma901801s
32. Zhang, B.; Wang, Z. *Chem. Commun.* **2009,** 5027–5029. doi:10.1039/B909424E
33. Makal, T. A.; Li, J.-R.; Lu, W.; Zhou, H.-C. *Chem. Soc. Rev.* **2012,** *41,* 7761–7779. doi:10.1039/C2CS35251F
34. Düren, T.; Sarkisov, L.; Yaghi, O. M.; Snurr, R. Q. *Langmuir* **2004,** *20,* 2683–2689. doi:10.1021/la0355500
35. Dawson, R.; Stevens, L. A.; Drage, T. C.; Snape, C. E.; Smith, M. W.; Adams, D. J.; Cooper, A. I. *J. Am. Chem. Soc.* **2012,** *134,* 10741–10744. doi:10.1021/ja301926h
36. Dawson, R.; Stöckel, E.; Holst, J. R.; Adams, D. J.; Cooper, A. I. *Energy Environ. Sci.* **2011,** *4,* 4239–4245. doi:10.1039/C1EE01971F
37. Wahby, A.; Ramos-Fernández, J. M.; Martínez-Escandell, M.; Sepúlveda-Escribano, A.; Silvestre-Albero, J.; Rodríguez-Reinoso, F. *ChemSusChem* **2010,** *3,* 974–981. doi:10.1002/cssc.201000083
38. Yang, S.; Sun, J.; Ramirez-Cuesta, A. J.; Callear, S. K.; David, W. I. F.; Anderson, D. P.; Newby, R.; Blake, A. J.; Parker, J. E.; Tang, C. C.; Schröder, M. *Nat. Chem.* **2012,** *4,* 887–894. doi:10.1038/nchem.1457
39. Sumida, K.; Rogow, D. L.; Mason, J. A.; McDonald, T. M.; Bloch, E. D.; Herm, Z. R.; Bae, T.-H.; Long, J. R. *Chem. Rev.* **2012,** *112,* 724–781. doi:10.1021/cr2003272
40. Dunne, J. A.; Mariwala, R.; Rao, M.; Sircar, S.; Gorte, R. J.; Myers, A. L. *Langmuir* **1996,** *12,* 5888–5895. doi:10.1021/la960495z
41. Furukawa, H.; Yaghi, O. M. *J. Am. Chem. Soc.* **2009,** *131,* 8875–8883. doi:10.1021/ja9015765
42. Llewellyn, P. L.; Maurin, G. *C. R. Chim.* **2005,** *8,* 283–302. doi:10.1016/j.crci.2004.11.004

License and Terms